RADC-TR-77-200
Final Technical Report
June 1977

COUPLING OF SINGLE-MODE OPTICAL FIBERS TO GaAs WAVEGUIDE

Laboratory for Applied Electronic Sciences

Approved for public release; distribution unlimited.

Sponsored by:

Defense Advanced Research Projects Agency
ARPA Order No. 3020

ROME AIR DEVELOPMENT CENTER
AIR FORCE SYSTEMS COMMAND
GRIFFISS AIR FORCE BASE, NEW YORK 13441

This report has been reviewed by the RADC Information Office (OI) and is releasable to the National Technical Information Service (NTIS). At NTIS it will be releasable to the General public, including foreign nations.

This technical report has been reviewed and is approved.

Andrew C. Yang

ANDREW C. YANG
Contract Monitor

Unclassified

SECURITY CLASSIFICATION OF THIS PAGE (When Data Entered)

(19) REPORT DOCUMENTATION PAGE	READ INSTRUCTIONS BEFORE COMPLETING FORM
(18) 1. REPORT NUMBER: RADC-TR-77-200	2. GOVT ACCESSION NO. / 3. RECIPIENT'S CATALOG NUMBER
(6) 4. TITLE (and Subtitle): COUPLING OF SINGLE-MODE OPTICAL FIBERS TO GaAs WAVEGUIDES	(9) 5. TYPE OF REPORT & PERIOD COVERED: Final repr. 1 Feb 76—31 Dec 77 / 6. PERFORMING ORG. REPORT NUMBER
(10) 7. AUTHOR(s): William S. C. Chang, Bhushan L. Sopori, Thomas L. Monsees	(15) 8. CONTRACT OR GRANT NUMBER(s): F19628-76-C-0032,
9. PERFORMING ORGANIZATION NAME AND ADDRESS: Washington University, Saint Louis, Missouri 63130	10. PROGRAM ELEMENT, PROJECT, TASK AREA & WORK UNIT NUMBERS: ARPA Order [redacted]-3020, 61101E
11. CONTROLLING OFFICE NAME AND ADDRESS: Deputy for Electronic Technology(RADC), Hanscom AFB, Massachusetts 01731, Monitor/Andrew Yang/ETSD	(11) 12. REPORT DATE: June 1977 / 13. NUMBER OF PAGES: (12) 171 p.
14. MONITORING AGENCY NAME & ADDRESS (if different from Controlling Office)	15. SECURITY CLASS. (of this report): Unclassified / 15a. DECLASSIFICATION/DOWNGRADING SCHEDULE

16. DISTRIBUTION STATEMENT (of this Report)

Approved for public release; distribution unlimited

DDC RECEIVED NOV 7 1977

17. DISTRIBUTION STATEMENT (of the abstract entered in Block 20, if different from Report)

18. SUPPLEMENTARY NOTES

Sponsored By: Defense Advanced Research Projects Agency (DoD) ARPA Order No. 3020

19. KEY WORDS (Continue on reverse side if necessary and identify by block number)

waveguide concepts, coupling concepts, single-mode fibers

20. ABSTRACT (Continue on reverse side if necessary and identify by block number)

The object of this research contract is to find an efficient method to couple a single-mode optical fiber to a GaAs waveguide at near infrared wavelengths. The general approach chosen is to first fabricate a transitional waveguide. The fiber and the transitional waveguide are then coupled together by the tapered velocity coupling method.

Technologies were developed and excellent results have been →

DD FORM 1 JAN 73 1473 EDITION OF 1 NOV 65 IS OBSOLETE

UNCLASSIFIED

SECURITY CLASSIFICATION OF THIS PAGE (When Data Entered)

408607

obtained in using the r.f. sputtering process with a cleaved GaAs mask to step-etch the GaAsP waveguides. This process followed by the r.f. deposition of SiO_2 buffer layer and by deposition of either BaO_2 glass or AZ1350 waveguiding layer on top of the SiO_2 layer has led to very high coupling efficiency (80%) between the primary waveguide and the transition waveguide. Research on the deposition of sodium glass was undertaken to obtain the transition from uniform planar waveguide to channel waveguide. These results demonstrated that highly efficient fiber to thin film waveguide coupling can probably be realized by this method. Additional research is needed in order to demonstrate a complete coupling system.

TABLE OF CONTENTS

TABLE OF CONTENTS (Continued)

1. INTRODUCTION

The potential of combining signal processing capabilities of integrated optics with the large information transmission capacity of a single mode optical fiber (SMOF) is well documented (1,2). Since the advent of integrated optics, about a decade ago, many components for optical communication have been developed. These include modulators and switches of GHz band width, directional couplers, filters, thin film lasers, etc.(3-6). Simultaneously, many important advances have been made in optical fiber technology. Single mode fibers with losses as low as 2dB/km have been fabricated (7,8). Fiber splicing and joining techniques which allow more than 95% transmission have been developed (9, 10). However, efficient fiber-to-thin film waveguide coupling still remains a major obstacle in realizing high data rate single mode fiber optical communication systems.

Low efficiencies achieved to date in coupling a SMOF to a thin film waveguide (TFWG) results from the fact that conventional high efficiency coupling techniques via phase matching and mode matching are difficult to apply. Difficulties arise due to two factors. Firstly, there is incompatibility in materials: the most important integrated optical component systems (from the consideration of modulation and switching and/or capability of monolithic integration of many devices and components) are high refrac-

tive index materials viz $LiNbO_3$ ($n \simeq 2.2$) and GaAs ($n = 3.47$). On the other hand lowest loss fibers have low index ($n \simeq 1.46$) and are made of silica (Bell fiber: Silica/Borosilicate; Corning Fiber: all silica). Hence conventional high efficiency phase matching cannot be realized. Secondly, there are geometric incompatibility between the rectangular TFWG and the circular fibers, as well as the stringent alignment required for mode matching. In addition, there is the need to prepare the ends of both the fiber and the waveguide to optical flatness and normal to their axes.

In this report we shall present first a discussion of different types of the SMOF-TWFG coupling, their advantages and disadvantages and, in particular, the tolerance considerations of the fabrication processes for these coupling methods. Following these considerations, we shall discuss the design calculation, the fabrication, and the evaluation of the new method of coupling a high index TFWG to a SMOF, utilizing a low index transitional waveguide (TWG). In this new method the TWG is formed on the same substrate as the primary high index waveguide. The tight tolerances for mode matching at the primary and the transitional waveguide junction are met by sputter etching and thin film deposition techniques. The TWG is also designed to allow the interconnection of the TWG and the SMOF utilizing tapered velocity coupling method which is known to be highly efficient with low tolerance requirements.

In the process to fabricate and to evaluate this coupler a number of techniques such as sputter deposition and etching, fabrication of low-loss sodium glass waveguide, the use of hollow dielectric waveguide mode, and evaluation of the step etch by radiation pattern were developed. These techniques are discussed separately in Section 5, 6 and 7.

2. BASIC COUPLING METHODS AND THE PROPOSED COUPLING SCHEME

2.1 Coupling Methods

Coupling between a TFWG and a SMOF is in principle similar to the coupling of microwave components. There are basically two methods by which energy can be efficiently transferred from one waveguide to the other. These are: (i) mode matching and (ii) phase matching. In this section we will describe each of these methods in detail as applied to TFWG-SMOF coupling and bring out the requirements of high efficiency in terms of tolerance demands in fabrication.

2.1.1 Mode Matching

This method of coupling involves bringing the two components end to end in such a way as to maximize the overlap between the field due to the waveguide in the boundary adjoining the fiber end and the desired mode of the fiber (for this reason mode matching is also called direct or end excitation). Due to the circular symmetry of the fiber, an optimum coupling can take place only if the incident field due to the waveguide at the boundary is also circularly symmetric. In addition, it is necessary to have the beam size of the

waveguide field to be about the same as the beam size in the fiber. This can be achieved in two ways. One way is to use a channel waveguide of square cross section whose dimensions are nearly the same as the core diameter of the fiber. The other way is to use a focussing element like a lens or a mode transformer like a horn, either on the waveguide or at the fiber end.

Theoretically the mode matching can yield very high efficiencies, limited only by the reflection at the junction. However, in practice the requirements of alignment between the waveguide and the fiber, and the quality of the end surfaces needed to obtain high efficiency are difficult to meet with. These requirements are:

1. The axes of the waveguide and the fiber should be colinear.
2. The ends of the waveguide and the fiber should be normal to their respective axes.
3. The separation between the ends of the fiber and the waveguide should be as small as possible.
4. The end surfaces of the waveguide and the fiber should be of high optical quality to avoid scattering losses.

The requirements 1 and 2 are due to the fact that the wavefronts of the modal fields in the waveguide and the fiber are plane and normal to the direction of propagation. Thus, a tilt in the ends or the axes will result in coupling loss due to the mode conversion.

An axial (transverse) offset will result in the coupling loss due to the amplitude mismatch between the incident field and the fiber mode. The separation between the ends reduces the coupling efficiency due to the divergence of the field emanating from the waveguide end.

Additional power losses due to the random scattering can take place if the ends of the fiber and the waveguide exhibit surface roughness. A method of breaking a fiber to produce flat and perpendicular end faces has recently been developed by Gloge et al. (9). The end of the waveguide may be prepared in several ways depending on the coupling scheme to be used (the practical schemes of coupling by direct excitation are described later in this section). For certain crystalline waveguides like GaAs waveguides which exhibit good cleavage, high quality end faces can be produced by cleavage. In such cases, however, the waveguide must be oriented such that the cleavage plane is normal to the direction of propagation of the guided wave. Polycrystalline and amorphous waveguides would require painstaking task of polishing, in particular in maintaining the end normal to the axis. Another technique of end preparation is etching either chemically or by sputtering.

To estimate the magnitude of the coupling loss due to the misalignments, let us consider a thin film waveguide and an optical fiber brought end to end with a separation z as shown in Figure 2.1a. The field in the aperture next to the end of the fiber can be determined by first evaluating the field in the waveguide aperture and then taking into account

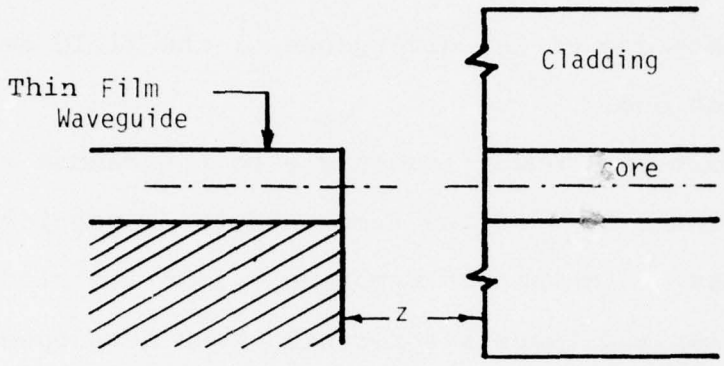

Figure 2.1a Coupling of a TFWG and a Fiber by Mode Matching

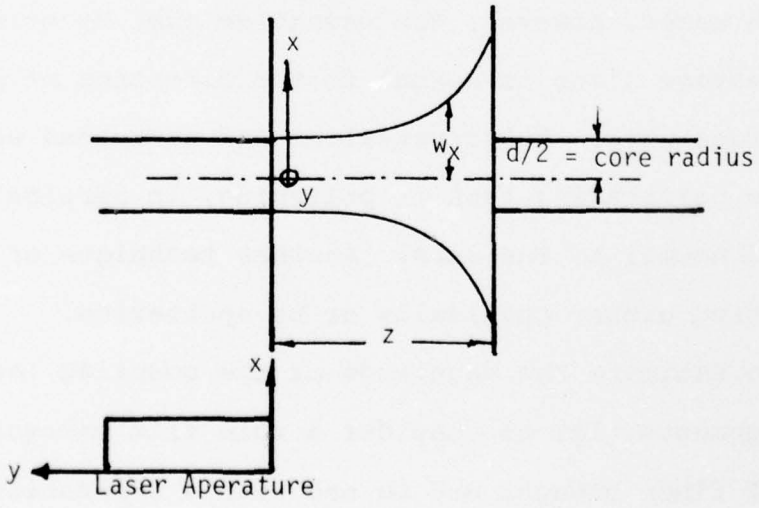

Figure 2.1b Gaussian Beam Emanating from Laser Aperture

the effects of propagation in a distance z. The excitation efficiency of the fiber mode due to the aperture field can then easily be evaluated by means of the overlap integral. However, in order to get a physical insight it is instructive to evaluate the coupling efficiency where the field emanating from the waveguide is assumed to have a convenient analytical form. Similar assessments were made for the coupling of the injection laser radiation into fibers. In the following paragraphs we will discuss the results already obtained for injection lasers as an example of fiber to waveguide coupling.

A useful analytical distribution of the field from a waveguide or a laser is a Gaussian field. Such a field has been experimentally observed to be emanating from the end of a stripe geometry semiconductor laser (11). The propagation of such a field along z direction can be described as(see Fig. 2.1b):

$$E = E(z)\exp\left\{-\left[\left(\frac{x}{w_x}\right)^2 + \left(\frac{y}{w_y}\right)^2 + j\frac{k}{2\pi}\left(x^2/R_x + y^2/R_y\right)\right]\right\} \qquad [2.1]$$

Where w_x and w_y are the beam radii along x and y at a distance z from the laser surface, R and R_y are the wave-front radii of curvature, and $k = 2\pi/\lambda$. Further, assuming

a Gaussian approximation of the mode of the fiber, the coupling coefficient between the laser field and the fiber can be calculated to be (11),

$$c = \frac{2/\left(\frac{w_{ox}}{a} + \frac{a}{w_{ox}}\right)}{\sqrt{1 + \frac{2z}{k(w_{ox}^2 + a^2)}}} \cdot \frac{2/\left(\frac{w_{oy}}{a} + \frac{a}{w_{oy}}\right)}{\sqrt{1 + \frac{2z}{k(w_{oy}^2 + a^2)}}} \qquad [2.2]$$

with the mode radius $a \overset{\Delta}{=} \frac{2\sqrt{2}\,\pi r}{\lambda}(\bar{n}\Delta n)^{1/2}$ where r is the core radius, λ is the free space wavelength, $\bar{n}$ is the average refractive index of the core and the cladding, and Δn is the difference between the refractive indices of the core and the cladding. Figure 2.2 shows the plots of the coupling coefficient c versus axial separation z for two experimental fibers whose mode radii are 2.6 μm and 4.6 μm. The parameter w_o is the half width of the laser beam waist. From this plot we can draw three conclusions:

1. The efficiency depends critically on the half width of the beam waist w_o. The beam waist must match the fiber core diameter in order to get high coupling efficiency.

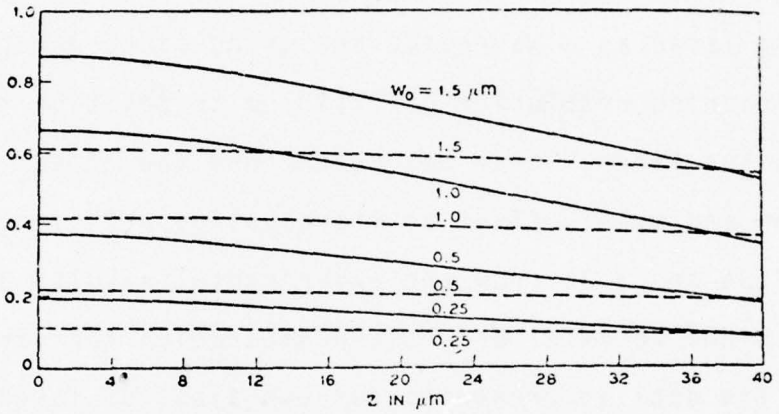

Figure 2.2 Power Coupling Coefficient **c** Versus Axial Separation **z** between a laser and a Single-Mode fiber (λ = 9000 A°)

——— 3.2μm fiber (mode radius 2.6 m)

----- 3.7μm fiber (mode radius = 4.6μm)

[after (11)]

2. The separation distance z must be less than 20 μm to maintain high efficiency.
3. As the mode radius of the fiber increases the effect of separation in reducing the efficiency becomes less.

Using laser as a waveguide and using micro-manipulators with positioning resolution of 0.125 μm to position the laser and the fiber, Cohen has determined the effect of separation and axial offset on the coupling efficiency. Figures 2.3a and 2.3b show the experimental results of power loss due to axial offset and separation for various fibers. The data is presented for two types of lasers; the diffused junction (DJ) and the double heterostructure (DH) with beam dimensions 3 x 6 μm and 1 x 3 μm respectively. From Figure 2.3a we see that coupling to a 3.2 μm fiber is more sensitive to axial offset for DH than for DJ. This is expected in view of the larger beam dimensions of the DJ laser. About 40% loss in power takes place with an axial offset equal to radius of the single mode fiber. Figure 2.3b shows axial separation is less critical than axial offset. Here the sensitivity to axial separation increases with reduction in core size of the fiber.

Similar results were theoretically obtained by Marcuse (12) in calculating the effects of axial misalignment for the coupling between a Gaussian beam and a fiber (dielectric

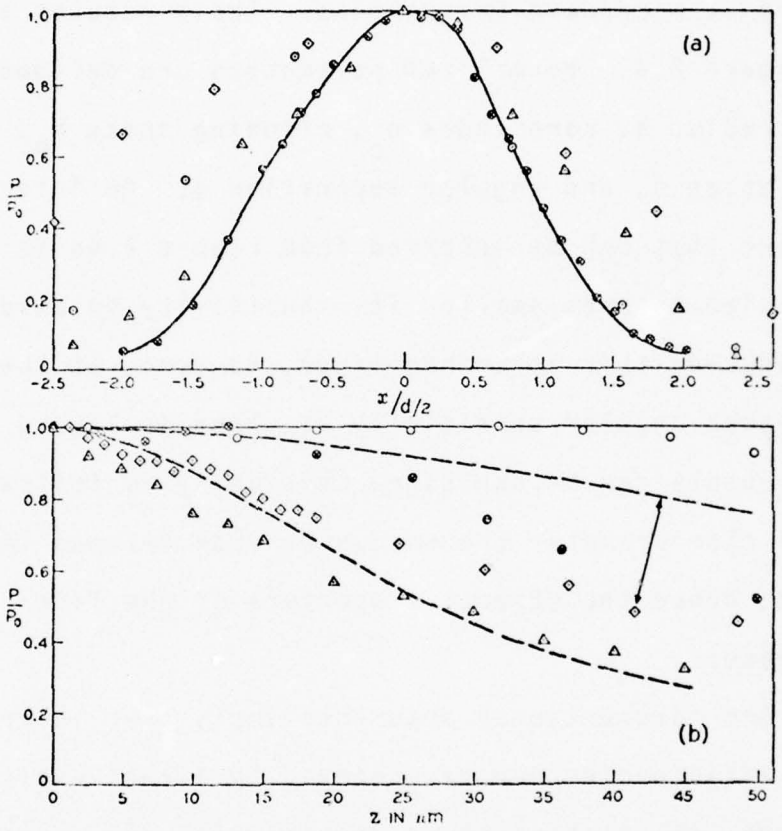

Figure 2.3 Profiles of the normalized power emitted from the end of a fiber which was displaced from its optimal position relative to the laser stripe.

Legend: ○ 3.2-μm fiber
· 10-μm fiber , L-229 #1 DJ laser
○ 19-μm fiber
◇ 3.7-μm fiber, L-229 #2 DJ laser
△ 3.2-μm fiber, L-363 #1 DH laser.

(a) The fiber core was offset in the plane of the junction. (b) The fiber core was axially separated from the laser surface. The dashed curves were based on Equation 2.2 with λ=9000 Å. (w_{0_z}=2.7μm, w_{0_y}=1.3μm, a=4.6μm for ◇ data; w_{0_x}=1.5μm, w_{0_y}=0.36μm, a=2.6 for △ data.)

[after (11)]

rod of refractive index 1.1 surrounded by air). Cook et al (13) have studied misalignment effects in coupling of two fibers at microwave frequencies. Their results are shown in Figure 2.4. Normalized parameters are defined in terms of core radius a, core index n_c, cladding index n_o, axial separation s, and angular separation ϕ. An interesting feature that can be inferred from Figure 2.4a is that as core size becomes smaller its sensitivity to axial offset is reduced; this is accomplished, however, at the cost of increased angular sensitivity as shown in Figure 2.4b. This result can be explained physically as follows: for small core diameter the waveguide mode becomes loosely bound, hence the effective aperture of the fiber is increased.

The forementioned arguments imply that in principle high efficiencies can be achieved by direct excitation. However, in practice there requirements are extremely difficult to meet with. These requirements for high efficiency demand the following alignment tolerances:

1. axial offset less than 1μm
2. angular alignment less than 2°
3. axial separation 10-15μm is acceptable

Any practical schemes of film-fiber coupling must incorporate means of such critical alignments and methods of end preparation, and in addition, be insensitive to vibrations.

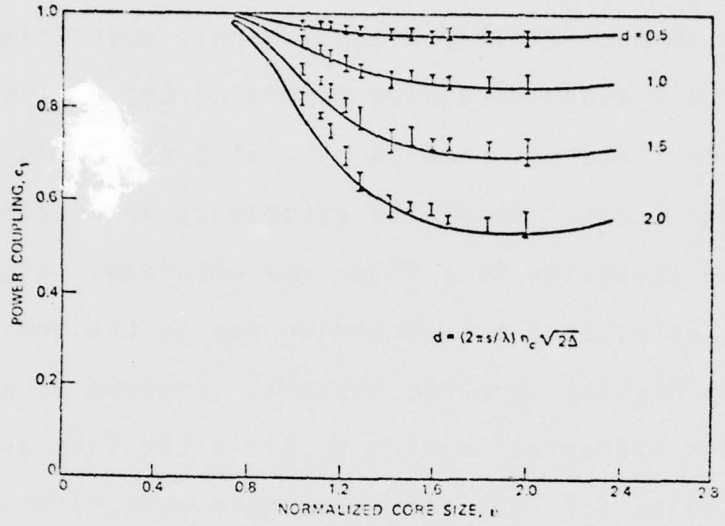

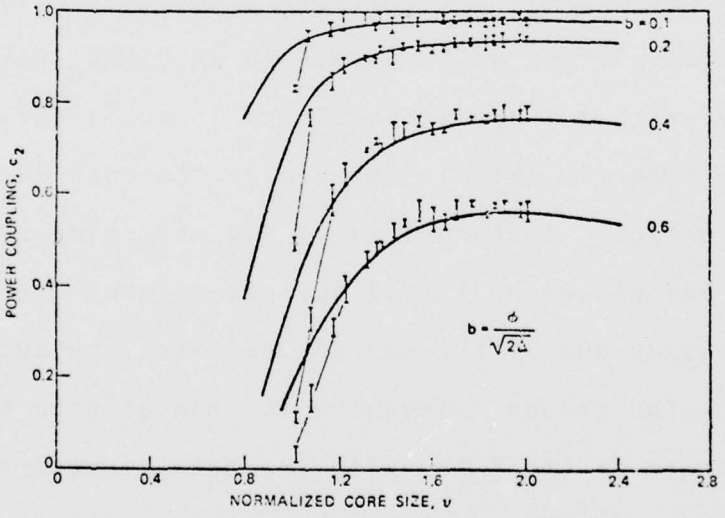

Figure 2.4 (a) Power coupling through translationally displaced joint as a function of normalized core size and axial translation, d.

(b) Power coupling through angularly misaligned joint as a function of normalized core size and misalignment, b.

[after (13)]

Normalized core size υ is related to the actual core radius a by

$$\upsilon = \frac{2\pi a}{\lambda} (n_c^2 - n_o^2)^{\frac{1}{2}}$$

Biovin used a preferentially etched V-groove in an Si wafer to mechanically align a single mode film with respect to a glass waveguide formed on the Si wafer (14). The guided field was focused by a thin film lens on the end of the fiber. About 20% efficiency in coupling from a thin film waveguide to a fiber was obtained. High coupling loss was attributed to scattering due to the end facets formed by crystallographic etchant. Guttman et al. (15) proposed a mechanical device to align the film and fiber ends; results for coupling two single mode fibers showed high efficiencies ~ 85% could be achieved by this method. Recently Hsu and Milton (16) have extended Biovin's approach to position a fiber with respect to an $LiNbO_3$ waveguide. A channel with a V-groove is etched in an Si wafer such that when the fiber is laid in the groove the core is just above the Si surface. A channel waveguide with cleaved ends is flipped and placed on the Si surface so that the heights of the waveguide and of the end of the fiber are automatically aligned. The channel waveguide is then aligned horizontally with respect to the fiber with the help of registration marks along the sides of tne channel waveguide. The highest efficiency obtained by this method was only about 27%.

Techniques of improving the direct excitation efficiency by formation of a microlens has been investigated by many workers. Fabrication of a photoresist lens at the end of

an optical fiber was reported by Cohen and Scheider (17) and by Auracher (18). Kato (19) formed similar lenses by thermally melting the end of the fiber (multimode). Significant improvements in coupling have been obtained by this technique.

With the present techniques of direct excitation the efficiency of coupling from a waveguide to a single mode fiber still remains less than 30%.

2.1.2 Phase Matching

It is well known that efficient power transfer can take place between two waveguides whose phase velocities are equal, provided that the waveguides are coupled together (20). For dielectric waveguides the necessary coupling may be provided by the evanescent field overlap when the waveguides are brought into close proximity. Such a system can easily be analyzed using the coupled mode theory (21). Two important results of such an analysis are:

1. 100% power transfer can be obtained only if the difference in the phase velocities, $\Delta\beta$, is zero and the coupling coefficient is constant over the coupling length.
2. The coupling length for maximum power transfer is critical.

Phase matched coupling has been used for making directional couplers, switches, etc., where the coupling length and the uniformity of the coupling coefficient can be controlled (22,23).

Use of a periodic structure to phase match two waveguides of different phase velocities has been studied for planar waveguides (24) and for film fiber coupling (25,26). In general, this method generates unwanted grating orders which reduce the coupling efficiency. Experimentally, coupling efficiencies of 27% for uniform planar waveguides and 8% for TFWG fiber have been obtained. Use of blazed gratings to suppress the unwanted diffracted order are expected to improve the efficiency.

To improve tolerances in coupling length, use has been made of tapered velocity coupling (TVC). In this method phase matching of the two components takes place only at one point in the coupling region. However, the wave number β_1 and β_2 of the two separate waveguides vary continuously as a function of distance such that $\Delta\beta = (\beta_1 - \beta_2)$ changes sign from one side of the coupling region to the other. Figure 2.5a shows such a scheme. The wave number β_1 of the isolated waveguide WGI is reduced gradually by tapering its film thickness whereas β_2 is constant. Wilson and Teh have analyzed the power transfer between the waveguides of such a system by numerically solving a set of coupled mode equations (27). Figure 2.5b shows schematically typical plots of the powers p_1 and p_2 contained in the waveguides WGI and WG2 respectively, as a function of coupling length.

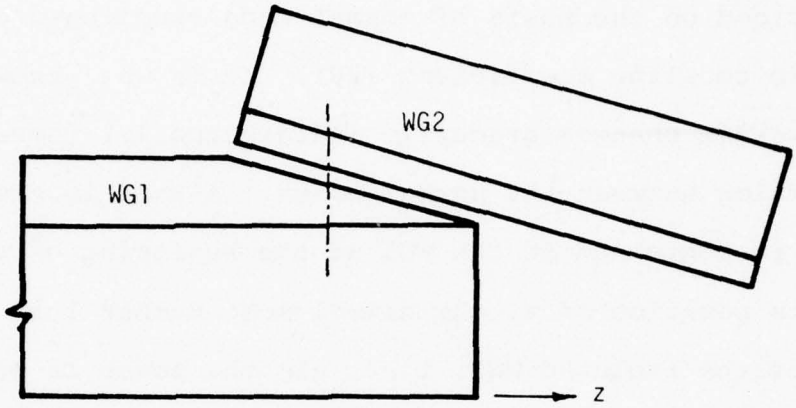

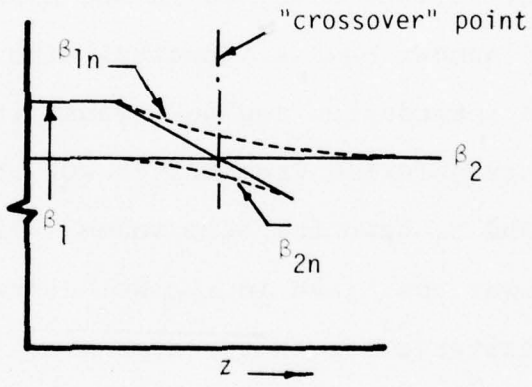

(a)

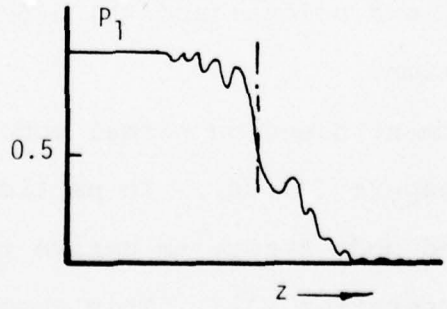

(b)

Figure 2.5 Principle of operation of a tapered velocity coupler. Variation of (a) β/k and (b) power in WG1 and WG2 along the coupling length.

The operation of a tapered velocity coupler can be easily understood on the basis of normal mode coupling due to a non-uniform coupling coefficient (28).* It is well known that if β of a system changes gradually (adiabatically) there is no power conversion between the normal modes. Assume in Figure 2.5 that power is contained in the WG1 at the beginning of the interaction. At this position of z, the normal mode number 1 is the same as the mode of the isolated WG1, i.e., all the power is contained in the normal mode number 1. As the mode propagates toward larger values of z, this power will be retained in the normal mode of the system. But normal mode number one is identical with the mode of WG2 at the exit end of the interaction region. Thus, it would appear that the total power is transferred from WG1 to WG2 at the "crossover" region where β_1 and β_2 have the same value. Figure 2.5b illustrates the apparent power contained in the WG1 at various positions of z. Two important criteria for this scheme are: (a) $\Delta\beta$ at the end of the interaction region should be large; this ensures single normal mode excitation at the end points; and (b) $d\Delta\beta/dz$ should be small to allow adiabatic operation.

Theoretical treatment based on normal mode analysis is given in several excellent papers (29,30). In particular, Milton and Burns have used coupled mode theory to derive the approximate condition for adiabatic operation (31). This condition demands

*The normal modes are the local modes of the total 5 layer structure at a given position in z. The β's of the normal modes are designated as β_{in} (i=1,2,3,4....), while the β's of the isolated WG1 and WG2 are designated as β_1 and β_2.

$$d(\Delta\beta)/dz \leq 5.9\ kk^* \tag{2.3}$$

where k is the coefficient of coupling. Moreover, for a uniform coupling gap between two waveguides the required coupling length (for 95% power transfer) is given by

$$\Delta z_T \leq 53/\Delta\beta_T \tag{2.4}$$

where Δz_T is the coupling length and $\Delta\beta_T$ = 1/2 of the total change in β. It should be emphasized that TVC can result in nearly 100% coupling efficiency; however, this needs a long coupling length and negligible scattering loss in the coupling region. In a practical coupler, due to inherent propagation loss, small coupling lengths are desired.

TVC coupling of uniform planar waveguides has been well established (32-34). Efficiencies exceeding 85% have been experimentally demonstrated (33). Dalgouette et al., have used TVC for coupling "externally mounted fibers" with over 70% efficiency in 2 mm length (35). High efficiency power transfer (>95%) between two single mode fibers has been demonstrated by Yamamoto et al. (36). The fibers were chemically etched to form long gradual tapers (1/1250, 1/2500) and held together due to surface tension of the matching oil effective coupling length was about 1 cm for 95% power transfer.

It is, thus clear that TVC can yield high efficiencies if $d(\Delta\beta)/dz$ is small. There are problems when $\Delta\beta_T$ is either too small

or when refractive indices are such that very small film thickness is required for phase match. In the former case single normal mode operation is difficult whereas in the latter cases excessive scattering losses occur at very small film thickness.

Use of tapered velocity coupling for interconnecting high index waveguides to low index waveguides was proposed by Dalgoutte et al., (34) and Hsu et al. (16). Their scheme is shown in Figure 2.6. It consists of a branching transitional waveguide so that the power from a desired mode in the primary WG is channelled into the transitional WG. The TWG can then be connected to the fiber by tapered velocity coupling. For adiabatic mode liftoff of TE_o mode to take place (Region I) the requirements of the TWG are (16):

1. The refractive index of the guiding region of the TWG, n_4 should be greater than n_2, the refractive index of the primary guiding film.
2. The thickness t_4 of the TWG films should vary from zero to t_{4max} such that $t_{4max} > t_{cut\ off}$, the cut off thickness t_4 required to form a waveguide with a substrate refractive index n_2.
3. The coupling length L for a linear taper for adiabatic operation must satisfy

$$(1/L) < 0.4(\Delta\beta_n)^2_{min} / \left[\left| (\Delta\beta_n)_{\text{at point 1}} \right| + \left| (\Delta\beta_n)_{\text{at point 3}} \right| \right] \tag{2.5}$$

where $\Delta\beta_n$ is the difference in β of the two normal modes involved.

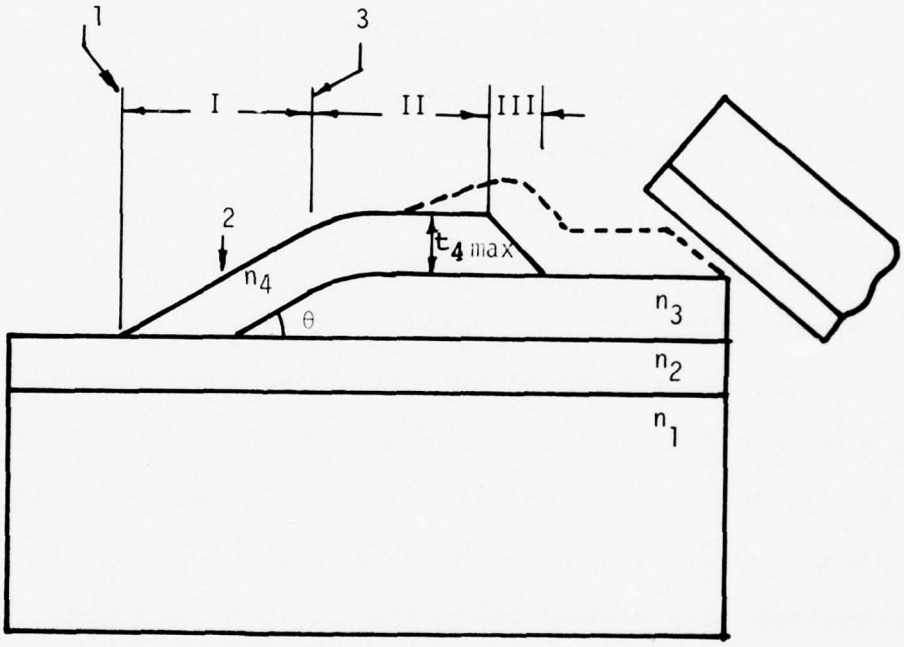

$\beta_i (i=0,1)$ = Propagation wave numbers of normal mode, i

$(\Delta\beta_{01})$ = Minimum difference in normal modes i and j in the region I, of the composite structure.

[after (16)]

Figure 2.6 Schematic Diagram of Mode Lift-Off

4. The inclincation of mode liftoff wedge should satisfy

$$\theta < 0.5\ \Delta\beta_n' \Big/ \sqrt{\beta^2 - k^2 n_3^2} \qquad (2.6)$$

where $(\Delta\beta_n')_{min}$ is the minimum $\Delta\beta_n$ in region II.

5. The thickness of the film t_3 away from the liftoff region, i.e., Region II in Figure 2.6, should be such that the power in the normal mode is confined to the TWG.

Hsu et al., (16) have calculated the values of L_{min} and θ to be 223 μm and 0.4 m rad respectively for a transition from $LiNbO_3$ primary waveguide to a Nb_2O_5/SiO_2 TWG.

It should be pointed out, however, that the mode liftoff method has a severe drawback due to the fact that the effective index, β/k of the guided mode in the liftoff region (Region I in Figure 2.6) is close to n_2. From the point of view of geometrical optics representation of a guided mode, the angle of the modal ray made with respect to the normal of the air film interface in the liftoff region will be close to the total internal reflection angle. In such a case excessive scattering losses will be incurred even by very small surface roughness. The propagation loss due to surface scattering, α_s, was given by Tien (37) as:

$$\alpha_s = 4.343\ \sigma^2 \sin^2 \phi_1/2 \cos \phi_1 \cdot t_{eff} \qquad (2.7)$$

where

$$\phi_1 = \beta/n_f \cdot k, \quad \sigma^2 = \left[4\pi\ n_f/\lambda_o\right]^2 \cdot \left[\sigma_u^2 + \sigma_b^2\right] \qquad (2.8)$$

t_{eff} is the effective thickness of the waveguide; σ_u^2 and σ_b^2 are the rms roughness at the top and bottom surfaces of the waveguide. Based on the above equation Hsu et al., have calculated the loss for t_4 = 0.6 μm (for the waveguide shown in Figure 2.6) to be 30 dB/cm when σ^2_{rms} = 150Å. Losses for smaller value of t_4 are in excess of 100 dB/cm. The measured total losses for this structure are shown in Table 2.1.

Higher scattering losses may also occur in the TVC region where the phase matching point has β/k close to 1.45. Use of several transition regions with progressive reduction in β/k has been proposed to bring down the losses. This, however, would increase the overall length of the coupler. As a result, the total through-put efficiency will be reduced significantly. The fabrication of such a structure is also very complex.

Based on these results it can be concluded that mode liftoff using a TWG and subsequent coupling to a SMOF using TVC is very inefficient. Insertion losses greater than 20 dB in coupling from $LiNbO_3$ to a silica fiber can be expected. Moreover, such a scheme cannot be used for GaAs devices due to the fact that no transparent material with refractive index larger than that of GaAs is available.

2.2 The New Method

From the previous discussion we have seen that stringent requirements in alignment for direct excitation and inability to

Table 2.1

Mode Liftoff Efficiencies for Ti Indiffused Waveguides with SiO_2 Buffer Layers and Nb_2O5 Top Layers.

(After reference 16)

t_4	Taper Slope θ (Radians)	Total Loss Point 1 to 3	Branching Loss Across Point 2	Top Layer Propagation Loss
0.42	$3.0\ 10^{-4}$	14.0 dB(3mm)	No Liftoff	
0.86	$3.5\ 10^{-4}$	11.8 dB(7mm)	2%	19.6 dB/mm
1.2	$3.9\ 10^{-4}$	5.4 dB(6mm)	6%	20.6 dB/mm
1.35	$2.5\ 10^{-4}$	7.2 dB(6mm)	26%	12.2 dB/mm

fabricate an efficient low index TWG for TVC applications have limited the performance of TFWG-SMOF coupling. In this section we describe a new low index intermediary waveguide, i.e., a transitional waveguide (TWG) that will couple efficiently to the high index primary waveguide (PWG). Figure 2.7 illustrates the operation of this method. The TWG is fabricated on the same substrate as the PWG by sputter etching and thin film deposition techniques, thus permitting a high degree of alignment both in vertical positioning of the TWG with respect to the PWG and their axial parallelism. The thickness of the guiding layer of the TWG is tapered for evanescent coupling to the SMOF whose cladding over the coupling length is stripped.

Fabrication of the TWG involves first making a uniform planar TWG. This is shown schematically in Figure 2.8. Ideally it consists of step etching the primary waveguide, shown in Figure 2.8a, followed by deposition of a low index buffer layer. The buffer layer provides isolation of the waveguide mode from "mode sinking" due to the high index substrate. Finally, the low index waveguiding layer is deposited, Figure 2.8c. The location and the thickness of this layer are determined from the considerations of optimum mode matching between uniform planar primary waveguide and uniform TWG. For tapered velocity coupling the guiding layer thickness of the TWG will be tapered such that propagation wave number β in this region will decrease from a value slightly above β_f, the wave number

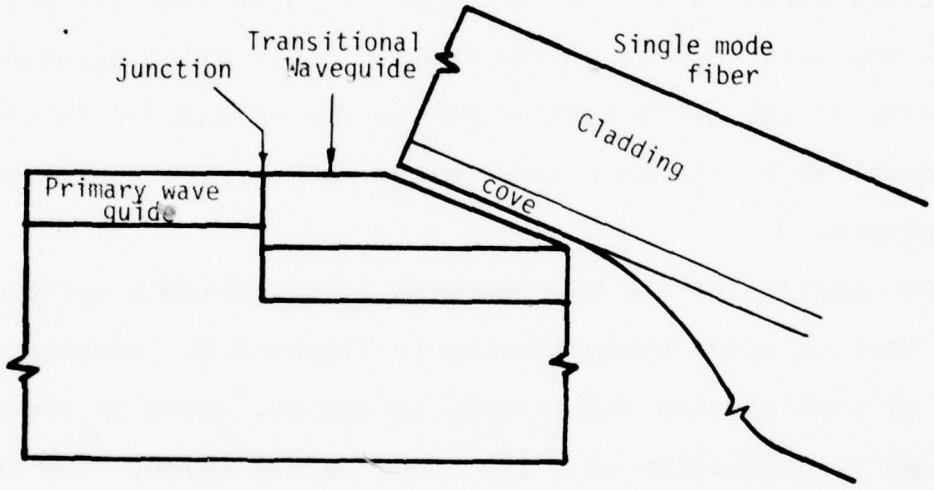

Figure 2.7 Principle of the Proposed Method

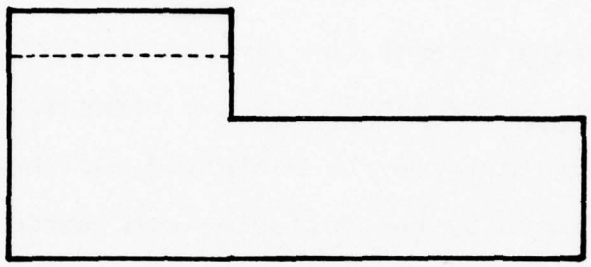

a. A vertical step etched in the primary wave guide

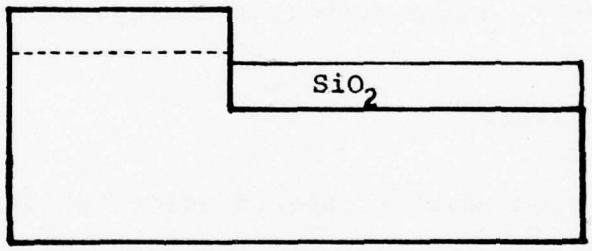

b. Deposition of low index isolation layer.

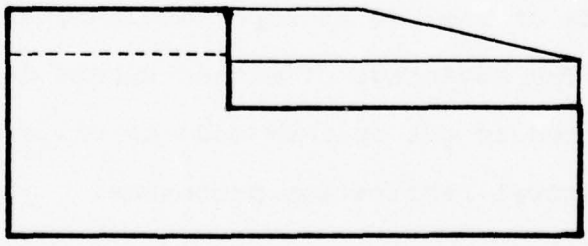

c. Deposition of low index guiding films with tapered thickness.

Figure 2.8 Steps involved in the fabrication of a transitional waveguide

of the fiber, at the beginning of the coupling region to a value lower than β_f at the end of the taper.

The refractive indices of the buffer and the guiding film n_b^{TWG} and n_f^{TWG} are determined from the requirements of the tapered velocity coupling between the TWG and the SMOF, i.e., $n_b^{TWG} < n_{core}$ and $n_f^{TWG} > n_{core}$ where n_{core} is the refractive index of the fiber core. These criteria may be satisfied for the two lowest loss single mode fibers by the following combinations of the film and the buffer materials.

(A)	Bell Lab fiber (core: silica, cladding, Borosilicate)	TWG* SiO_2/MgF_2
(B)	Corning fiber (core: doped silica, cladding: silica)	TWG Sputtered SiO_2 (in Ar)/ SiO_2 (in O_2)
(C)	Any fiber	Hollow Dielectric Modes of TWG

Two proposed ways of tapered velocity coupling between the TWG and a fiber are shown in Figure 2.9. In Figure 2.9a the TWG has a tapered film thickness such that its β/k at the beginning of the taper is greater than that of the fiber. In Figure 2.9b the film thickness of the TWG is kept constant; instead the fiber core is tapered. The advantage of either scheme depends on the thickness of SiO_2 required to get optimum mode matching with the PWG and the ease of the actual fabrication processes.

---

*It would seem reasonable to make buffer and guiding layers of the TWG of the same material as the cladding and the core of the fiber. However, there are two difficulties in doing so. Thin films of silica deposited by sputtering are oxygen deficient. The refractive index of these non-stochiometric SiO_2 films > 1.45. A small difference of refractive indices between the buffer and the guiding films would require a guiding film thickness of about 5 μm to form a waveguide. This would yield low efficiencies of the input junction of the TWG because most of the primary waveguides have thickness in the 1-2 μm range.

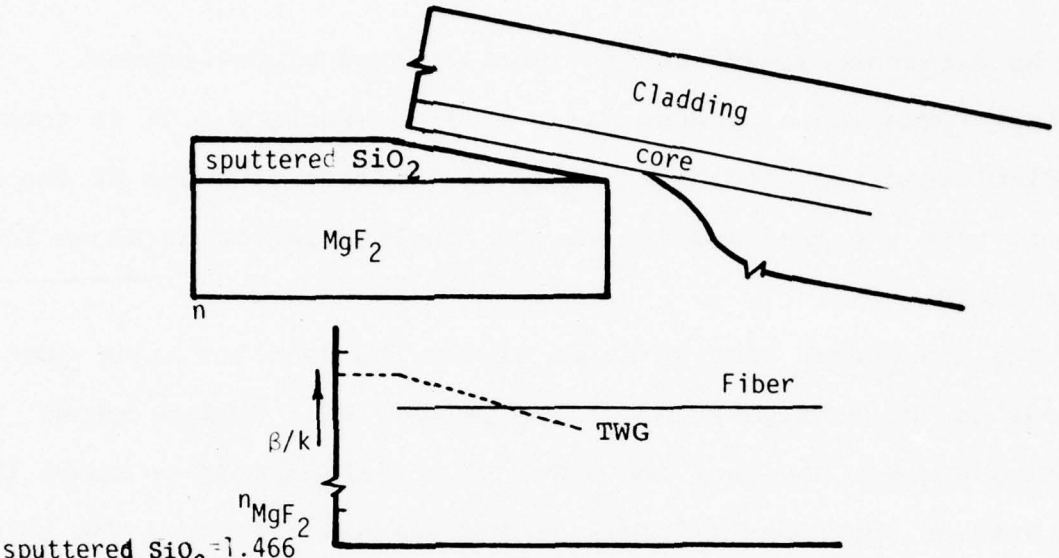

sputtered SiO_2 =1.466
MgF_2=1.38
n_{silica} =1.458

Figure 2.9a Coupling scheme when $\beta/k \Big|_{TWG} > n_F$

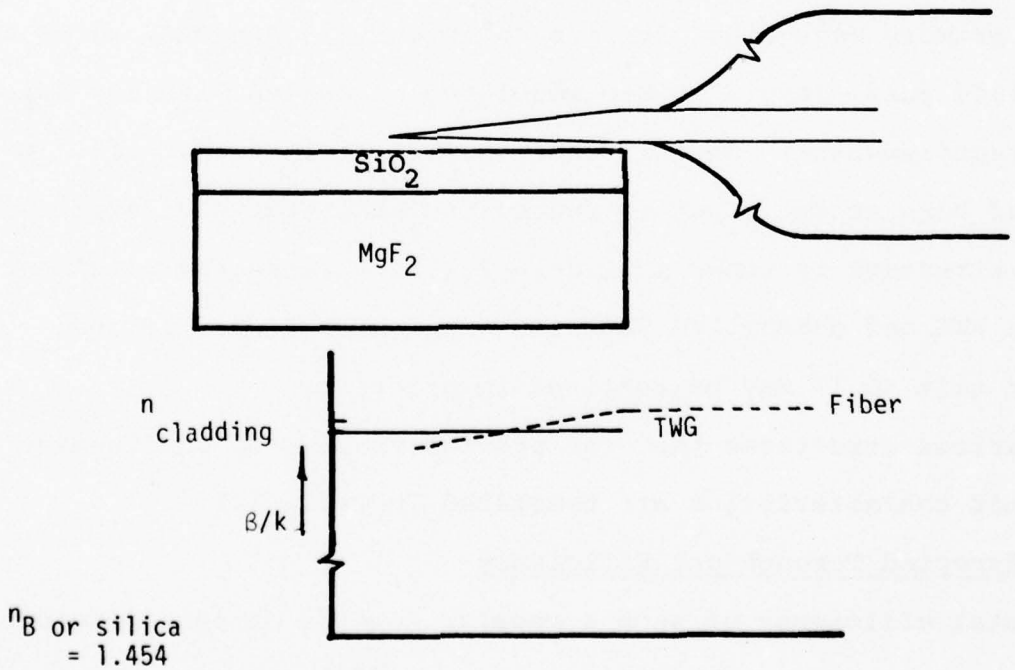

n_B or silica
= 1.454

Figure 2.9b Coupling scheme if $\beta/k \Big|_{TWG} < n_{cladding}$

An alternate scheme in its initial stage of development involves formation of sodium glass on SiO_2 (Section 5.3) to form a sodium·glass/SiO_2 TWG, and modify the refractive index of the fiber core to have a graded profile in the coupling region as shown in Figure 2.10.

The transverse configuration of the TWG near the input junction depends on the configuration of the primary WG. In the output coupling region, however, the width of the TWG should be about the core size of the fiber (~5 μm). For a uniform (or wide) PWG this necessitates the use of a transverse horn structure as a mode transformer, as shown in Figure 2.11a. Alternatively, one may consider the fabrication of a waveguide horn (35) for the transition. However a primary waveguide, for most purposes, is expected to be a channelled guide (e.g., an E-O modulator or switch with low drive power requirements). In this case the TWG will be channelled with a flared horn at the input to reduce the sensitivity to axial offset. Such a structure is shown in Figure 2.11b. Transverse alignment between PWG and channelled TWG with axial offset ~0.5 μm and angular tilt $<0.1^{\circ}$ may be realized in practice.

Various structures that can provide transverse confinement and their characteristics are described in Table 2.2.

2.3 Expected Through-put Efficiency

Total efficiency of such a coupler depends on three factors:

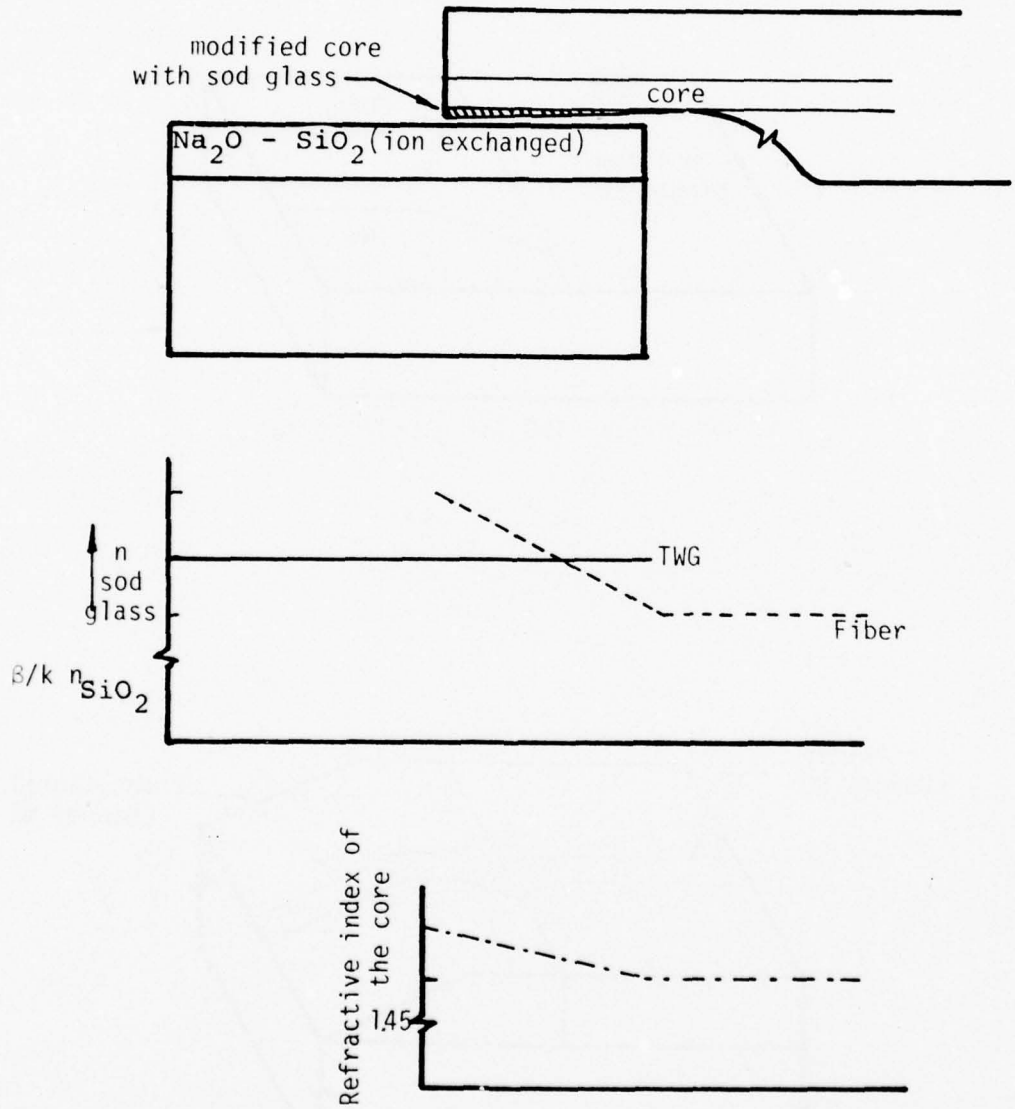

Figure 2.10 Method of modifying fiber core index for TVC

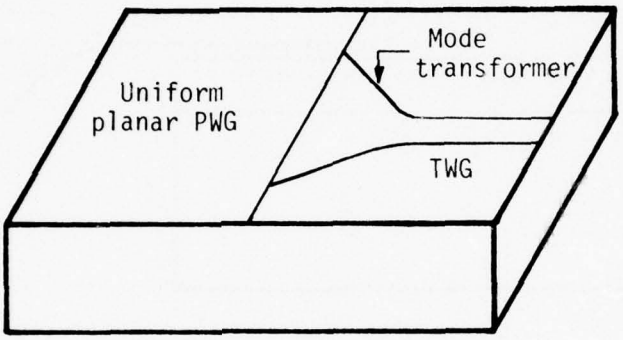

Figure 2.11a TWG for a Uniform PWG

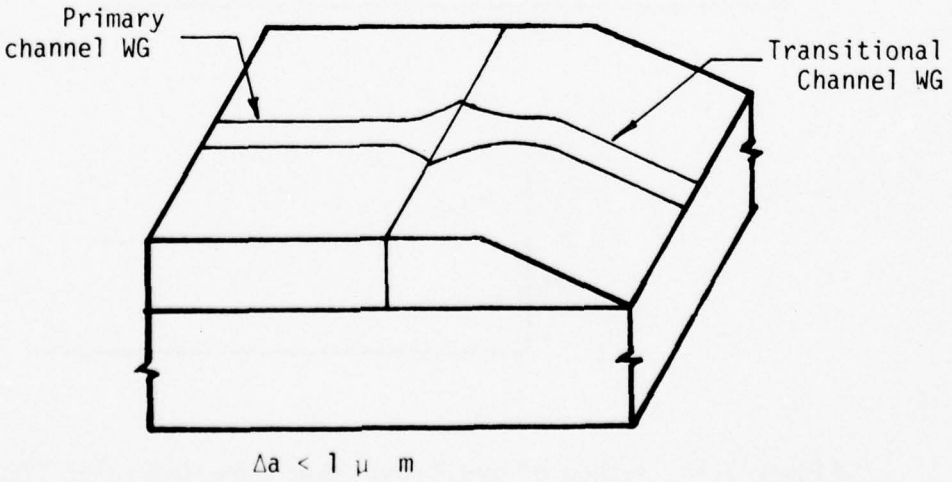

Figure 2.11b TWG for a Primary Channel Waveguide

Table 2.2 Channel TWG Structures

waveguide	structure	comments
ridge type	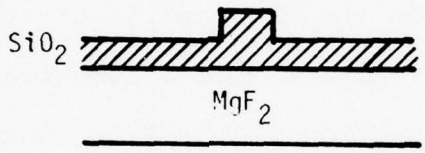	low loss; difficult to fabricate
metal confinement	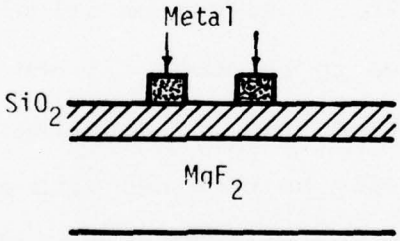	high loss due to metal absorption. Fiber alignment easy
Ion-exchanged sod. glass	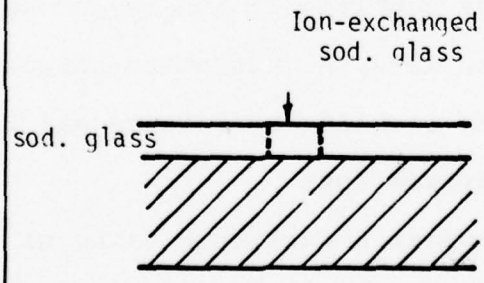	low loss. Fiber refractive index to be modified.

1. The insertion loss at the input junction of the TWG.
2. The propagation loss in the length of the TWG.
3. The insertion loss at the TWG-fiber juntion.

An estimate of the through-put efficiency can be made based on the present state of the art.

Work done to date on the fabrication of the uniform TWG has shown that efficiencies close to the theoretical values can be obtained at the input junction of the TWG. Loss at this junction is mainly the reflection loss (which will be incurred for all direct film-fiber couplers). This loss can be calculated for GaAs and $LiNbO_3$ primary waveguides to be about 17% and 5% respectively. From the results on tapered velocity coupling (36) efficiencies greater than 85% can easily be obtained with a coupling length of about 5 mm. Higher coupling efficiencies need longer coupling lengths. Since a longer coupling length is accompanied by a higher total propagation loss, a compromise between the total propagation loss and the coupling efficiency has to be reached in order to minimize the system loss.

For a practical coupler a realistic value of the propagation loss in the channel TWG is about 2 dB/cm. Assuming a coupling length of 5 mm to achieve an 85% coupling efficiency between TWG and the fiber, the total coupling efficiency between a GaAs wave-

guide and a SMOF can be 56%. Similarly, the total coupling efficiency between a $LiNbO_3$ waveguide and a SMOF can be calculated to be 64%. Higher efficiencies can be achieved if the propagation loss of the TWG is reduced.

3. DESIGN CALCULATIONS OF A UNIFORM PLANAR TWG

In this section we will analyze how to design the parameters of the TWG and how to assess the effects of the tolerances in the fabrication processes. These design parameters are the film thickness and the thickness of the buffer layer. To determine the required film thickness, we will calculate the coupling efficiency between the PWG and the TWG and the insertion loss, as a function of the film thickness of the TWG. The desired film thickness is the one which yields the highest efficiency. To evaluate the effects of the fabricational tolerance, we will calculate the coupling efficiency as a function of the tilt angle of the step-etch wall, as well as the gap separation between the PWG and the TWG.

3.1 Coupling Efficiency Between the PWG and the TWG

Consider the two thin film waveguides, WG1 and WG2, joined end-to-end as shown in Figure 3.1. We will first consider a case in which there is no separation between the guides and that the junction (xy) plane is perpendicular to the axes of the waveguides. The parameters t_i, n_{fi} and n_{si}

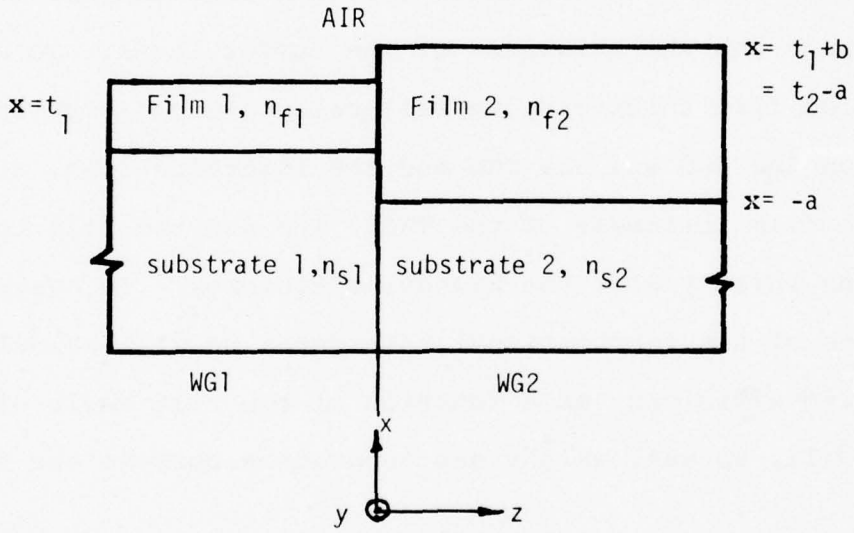

Figure 3.1 Two Waveguides Joined End-to-End

refer to the film thickness, the refractive indices of the film, and the substrate respectively, for the waveguide i (i=1,2). a and b are the offsets between the substrate-film and film-air interfaces of the two waveguides. Let a TE_m guided mode be excited on the WGI to the left of z=0 and propagate towards the junction. This mode has the electric field E in y direction, i.e., $E = E_{ym}$. At the junction, due to the discontinuity, there will be some reflection of the energy back to the WGI some transmission of the energy as the guided modes of the WG2 and radiation. Without any loss of generality, we will assume that a single mode is excited on the WGI and that the reflected radiation will be predominately in the same guided mode (this is based on our assumption of the vertical junction plane). We can apply the boundary conditions in the z=0 plane for the transverse field components. This yields

$$E_{ym}^{(1)} + a_r E_{ym}^{(1)} + \int_0^{\infty} q_r(\rho) E_y^{(1)}(\rho) d\rho$$

$$= \sum_n c_{tmn} E_{yn}^{(2)} + \int_0^{\infty} q_t(\rho) E_y^{(2)}(\rho) d\rho \qquad (3.1)$$

$$H_{xm}^{(1)} + a_r H_{xm}^{(1)} + \int_0^{\infty} q_r(\rho) H_x^{(1)}(\rho) d\rho =$$

$$\sum_n c_{tmn} H_{xn}^{(2)} + \int_0^{\infty} q_t(\rho) H_x^{(2)}(\rho) d\rho \qquad (3.2)$$

The fields are assumed implicitly to be of the form $e^{j(\omega t-\beta z)}$. The subscripts r and t indicate reflected and transmitted fields. m and n refer to the order of guided modes. The field components with explicit ρ dependence are the radiation modes. c_{tmn} is the coupling coefficient between mode m of the incident wave guide 1 and the mode n of the WG2, a_r is the reflection coefficient. Equations 3.1 and 3.2 can be solved approximately utilizing the orthogonality relations of the waveguide modes (38). The solutions are:

$$c_{tmn} = \frac{\beta_{2n}(1+a_r)}{2\omega\mu} \int_{-\infty}^{\infty} E_{ym}^{(1)} E_{yn}^{(2)*} dx$$

$$+ \frac{\beta_{mn}}{2\omega\mu} \int_{-\infty}^{\infty} \int_{0}^{\infty} q_r(\rho) E_y^{(2)}(\rho) E_y^{(2)*} d\rho dx \qquad (3.3)$$

From the scattering theory we know that the scattering is predominately in the forward direction for large abrupt discontinuity; hence, for thick waveguides $q_r(\rho)$ is small in our case and can be neglected. Equation 3.3 therefore reduces to

$$c_{tmn} = \frac{\beta_{2n}(1+a_r)}{2\omega\mu} \int_{-\infty}^{\infty} E_{ym}^{(1)} E_{yn}^{(2)*} dx \qquad (3.4)$$

Similarly, from Equation 3.2 we get

$$c_{tmn} = \frac{\beta_{1m}(1-a_r)}{2\omega\mu} \int_{-\infty}^{\infty} E_{ym}^{(1)} E_{yn}^{(2)*} dx \qquad (3.5)$$

Equations 3.4 and 3.5 can be combined to yield the expressions for the coupling coefficient and the reflection coefficient as:

$$c_{tmn} = \frac{2\beta_{1m}}{(\beta_{1m} + \beta_{2n})} \cdot \frac{\beta_{2n}}{2\omega\mu} \cdot \int_{-\infty}^{\infty} E_{ym}^{(1)} E_{yn}^{(2)*} dx \qquad (3.6)$$

and

$$a_r = \frac{\beta_{1m} - \beta_{2n}}{\beta_{1m} + \beta_{2n}} \qquad (3.7)$$

Numerical answers c_t and a_r are obtained by substituting the expressions of the normalized guided wave modes directly into equations (3.6) and (3.7).

In Figures 3.2 to 3.4, $|c_t|^2$ is plotted as a function of t_2 for several typical waveguide combinations. Here we have assumed b=o, so that the air-film interfaces of both waveguides can be co-planar to facilitate further microfabrication processing steps. Figure 3.2 shows a variation of the coupling efficiency (λ = 1.06 μm) between the TE_0 modes of a $GaAs_{0.77}P_{0.23}/GaAs_{0.64}P_{0.34}$PWG and an $AZ1350/SiO_2$ TWG. Similar plots for the coupling efficiency (λ=1.06 μm) of the same PWG to two different TWG's, $Glass/SiO_2$ and $AZ1350/SiO_2$ are compared in Figure 3.3. Coupling efficiency of a $LiNbO_3$ PWG and an SiO_2/MgF_2 TWG as a function of t_2 is shown in Figure 3.4. From these figures several observations can be noted: 1. The maximum efficiency for coupling TE_0 to TE_0 also corresponds to the minimum coupling for TE_0 to TE_1 (and higher order modes). 2. The

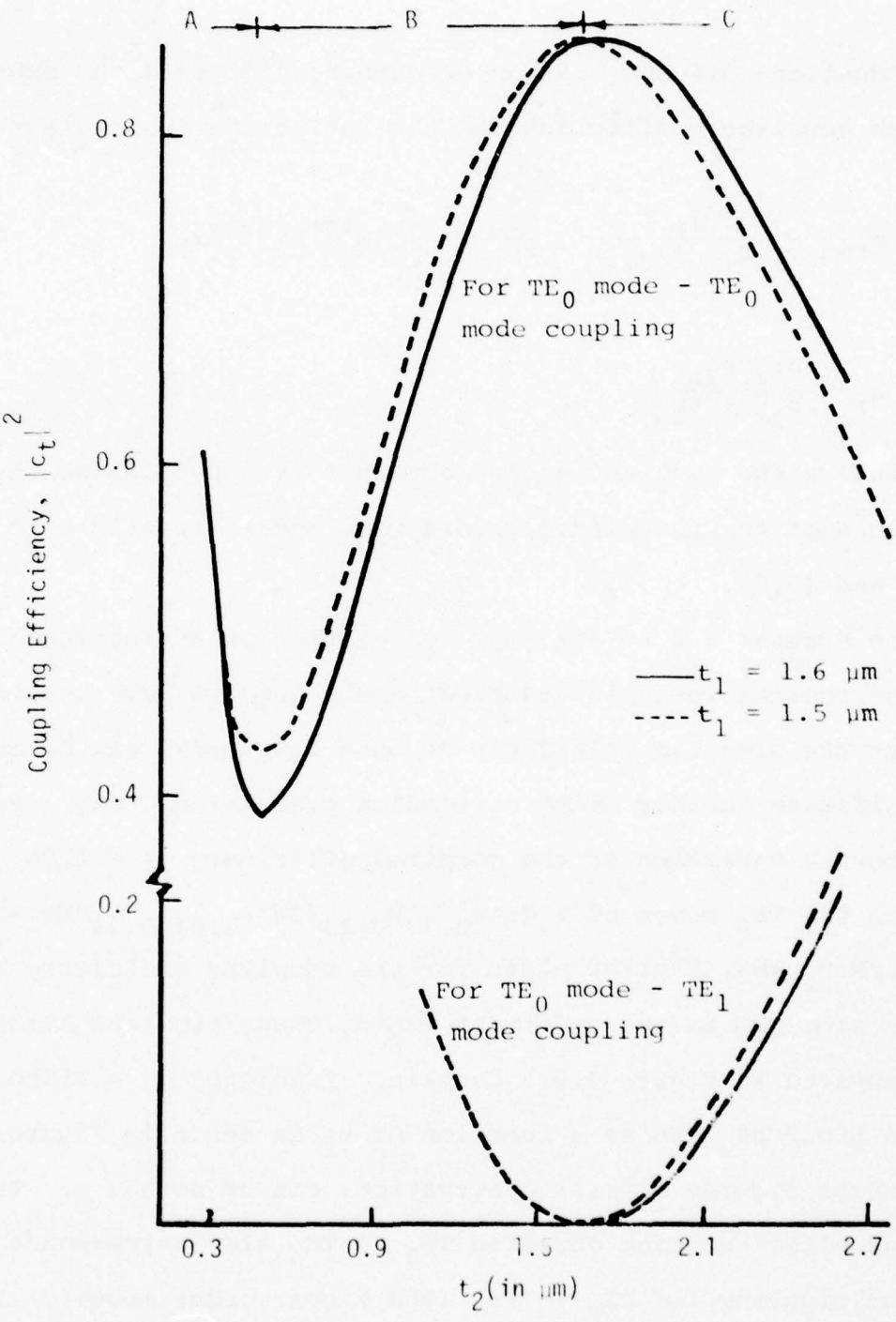

Figure 3.2 Coupling Efficiency Versus t_2
PWG: GaAs P
$0.77\ 0.23$/GaAs P
$0.62\ 0.38$
TWG: AZ1350/SiO_2
λ = 1.06μm

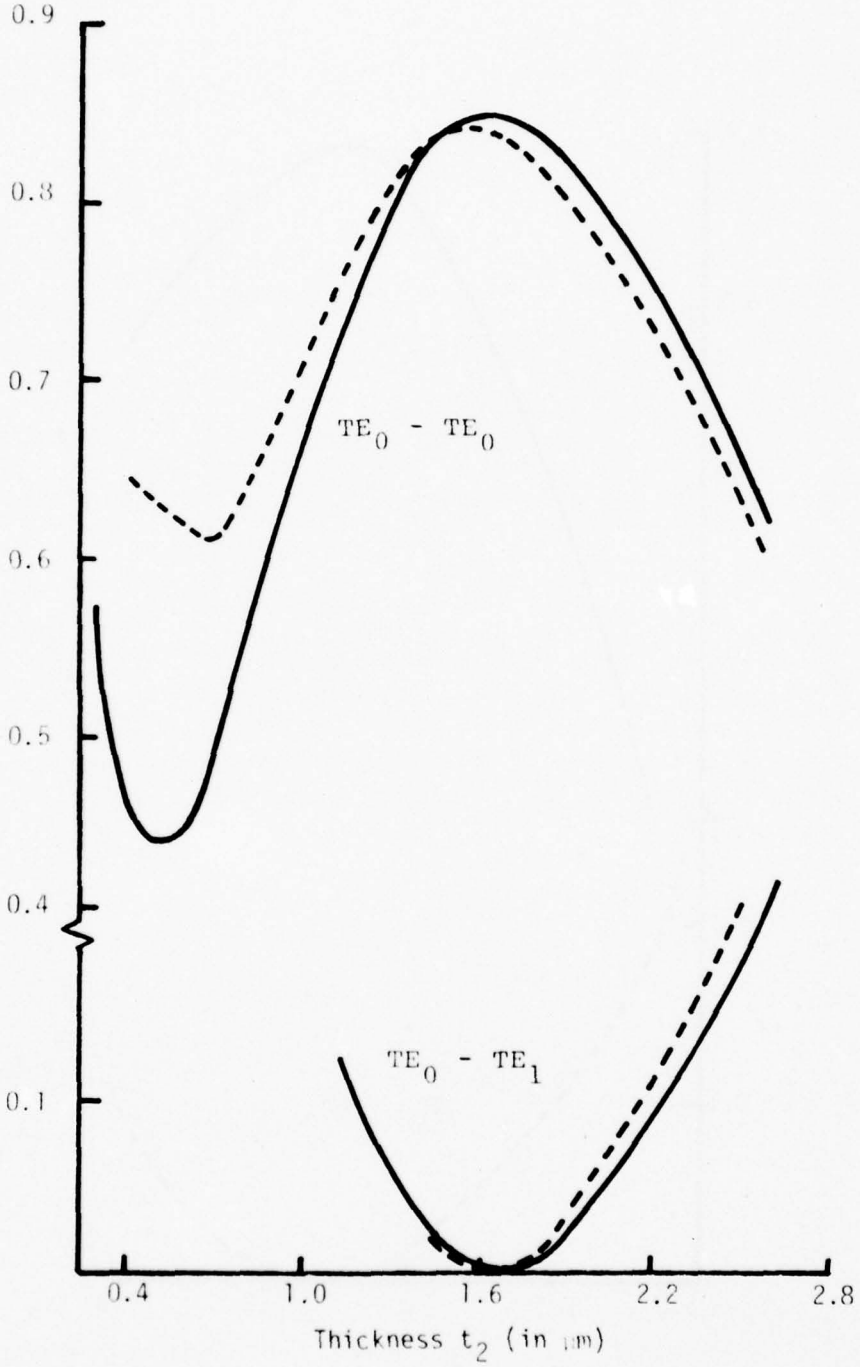

Figure 3.3 Coupling efficiency versus t_2
PWG: $GaAs_{0.77}P_{0.23}/GaAs_{0.62}P_{0.38}$
TWG: —— AZ1350/SiO_2, --- Glass/SiO_2
t_1 = 1.5μm, λ = 1.06μm

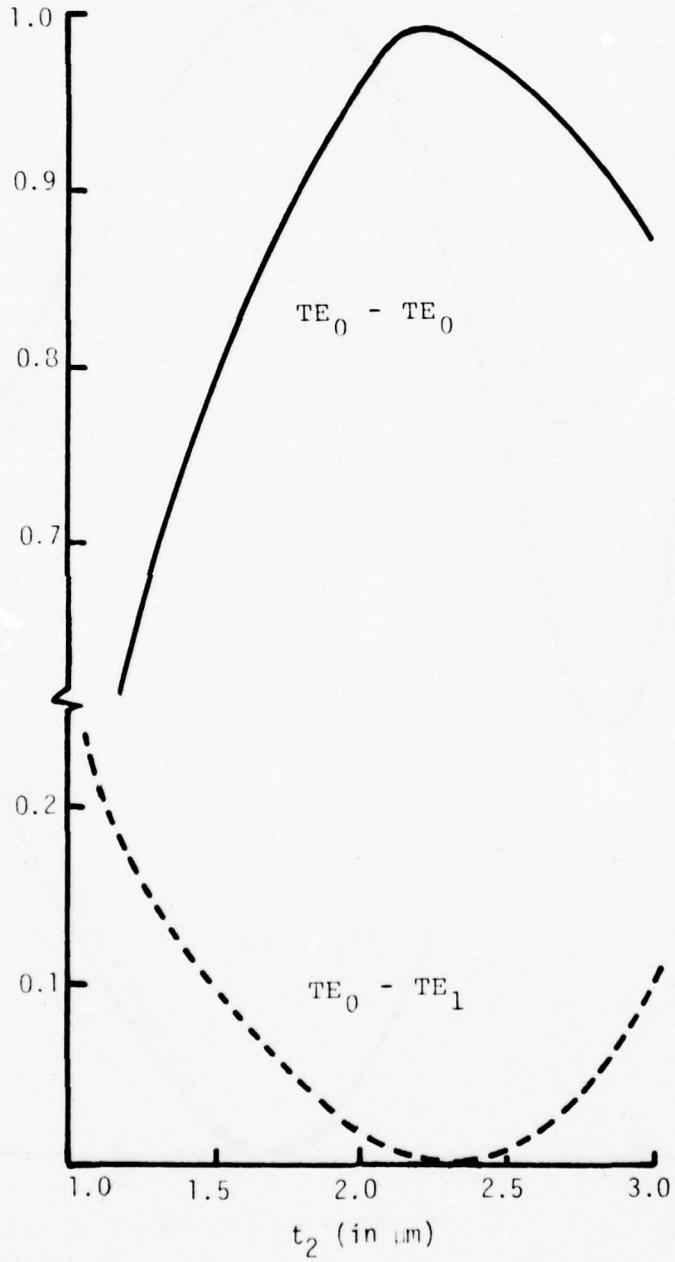

Figure 3.4 Coupling efficiency versus t_2
PWG: $LiNbO_3$
TWG: SiO_2/MgF_2
t_1 = 2μm, λ = 0.6328μm

peak efficiency is not very sensitive to t_2; change in t_2, Δt_2, of ±0.1 μm does not change the efficiency significantly. 3. Coupling efficiency versus t_2 shows three distinct regions, denoted as A, B and C in Figure 3.2. In Region A, $t_2<0.7$ μm, $|c_t|^2$ reduces as t_2 is increased; in Region B, $|c_t|^2$ increases with t_2, and then reduces again in the Region C. This variation is a consequence of the variation of the overlap between TE_0 modes of the primary and transitional waveguides and is not due to a breakdown of the approximation we have made. Such a variation in the overlap of the fields is clearly indicated in Figure 3.5 which shows the field distributions in the PWG and TWG referred to in Figure 3.2 for three values of t_2.

In a practical situation a waveguide is often well above cutoff and the guided mode of interest (due to its lowest propagation loss) is TE_0. In this case one can use the thick waveguide approximation, i.e., $\beta_1 \simeq n_{f1}k$ and $\beta_2 \simeq n_{f2}k$, to obtain a simple expression,

$$|c_{tom}|^2 = \frac{64}{\pi^2} \frac{n_{f1}n_{f2}}{(n_{f1}+n_{f2})^2} \frac{t_1}{t_2} \frac{}{\{1-\left[(m+1)\frac{t_1}{t_2}\right]^2\}^2}$$

$$\cos^2\left[\frac{(m+1)\pi t_1}{t_2}\right] \sin^2\left[\frac{(m+1)\pi}{2}\right] \qquad (3.8)$$

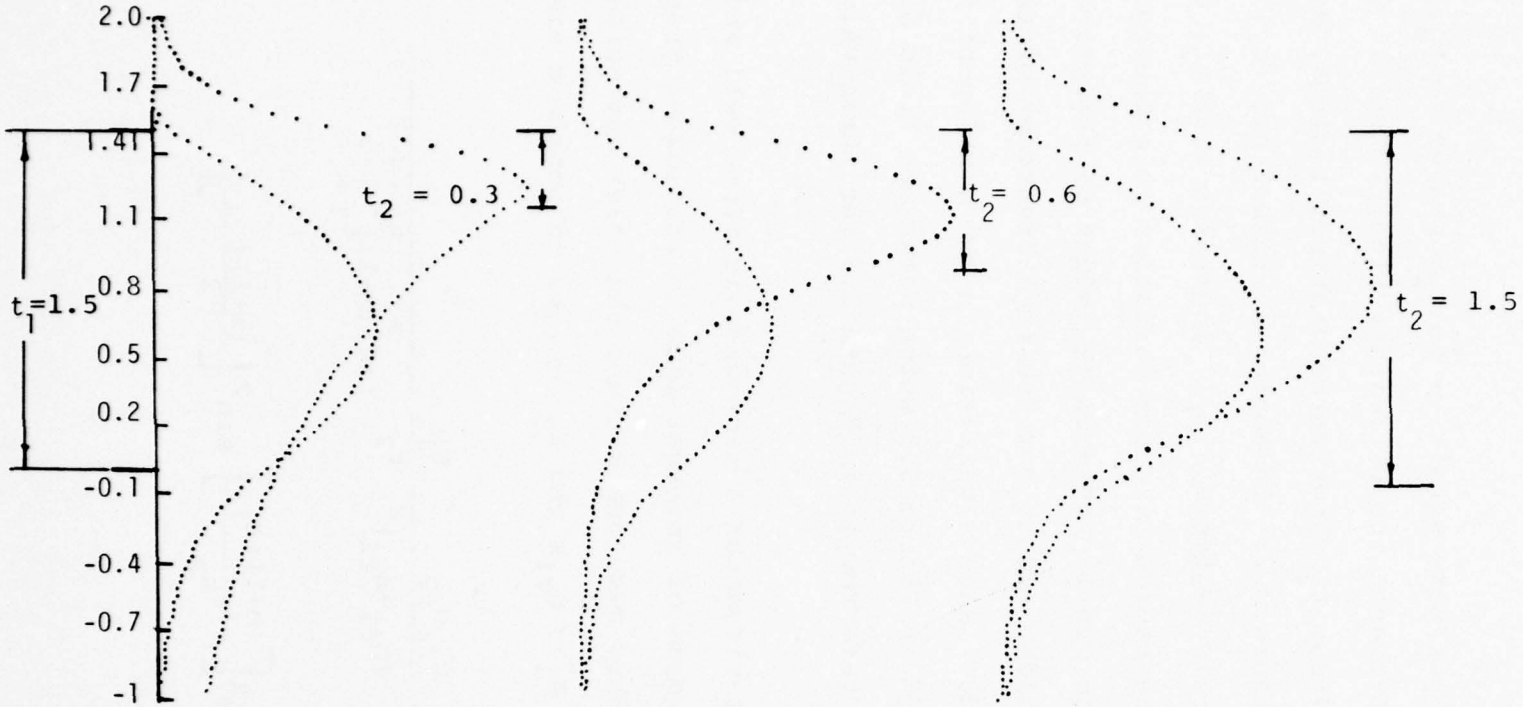

Figure 3.5 TE_0 field configurations for the PWG and the TWG (of Figure 3.2) for different values of t_2, showing variation in the overlap.

From Equation 3.8 we can easily see that for thick waveguides there is no coupling from TE_0 to odd modes of WG2. Figure 3.6 shows c_{tom}^2 as a function of $\frac{t_2}{t_1}$ for a $GaAs_{0.77}P_{0.34}$ waveguide to AZ1350/SiO_2 waveguide.

We see from these figures that coupling efficiencies as high as 84% between GaAs and glass waveguides and as high as 96% between $LiNbO_3$ and glass waveguides are possible. Coupling efficiencies for a practical PWG and TWG interconnection will, however, be less than these values due to the fabrication errors. These effects are considered in the next section.

3.1.1 Effect of Fabrication Errors on the Coupling Efficiency

We have calculated the coupling efficiency for an idealized junction between a PWG and a TWG. Although close to ideal junctions can be fabricated by the techniques described in Section 4, it is instructive to review the tolerance requirements in fabrication errors, in order to estimate the coupling losses. The sources of coupling loss are: 1. Tilt in the waveguide axes. 2. Tilt in the junction plane with respect to the waveguide axes. 3. Separation between the PWG and the TWG. From the section describing the fabrication of the planar TWG we shall see that sputter etching and thin film deposition can result in perfect parallelism of the PWG and the TWG. However, there is always a small tilt in the wall of the etched step (reasons and the means to minimize this

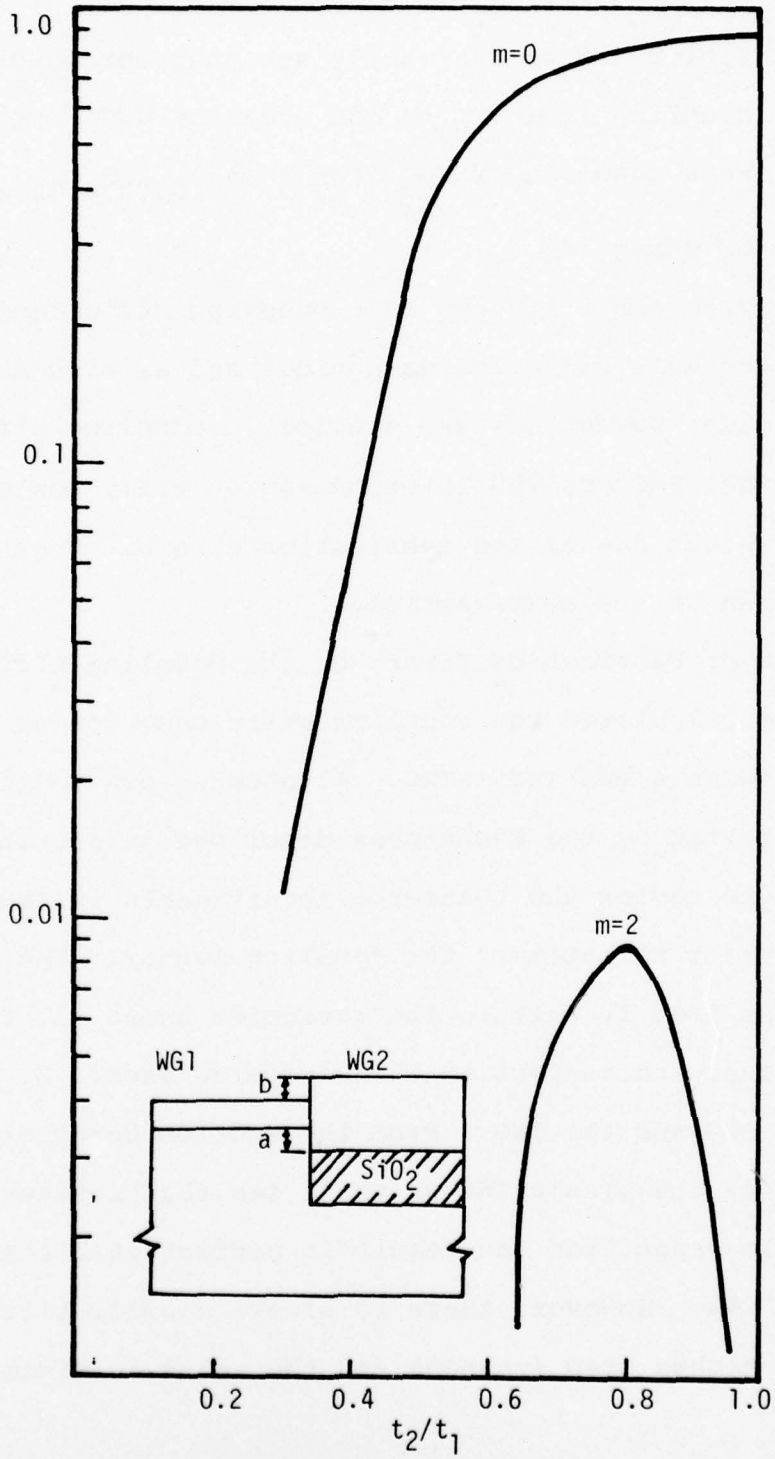

Figure 3.6 Calculated Coupling Coefficients Between the GaAs and the Transitional Waveguide

are described in Section 7). Furthermore, during the deposition of the buffer layer some of the material is deposited on the vertical wall of the step, resulting in a small separation (~2 μm) gap.

From the discussion in Section 2 we see that a small separation gap (<10 μm) should not result in any significant change in the coupling efficiency. Since the separation gap between the PWG and the TWG due to deposition of the buffer layer is only a few μm, no significant reduction in coupling efficiency is expected. Significant reduction in the coupling efficiency can, however, occur due to small angles of tilt in the step wall. We will, therefore, consider only the tolerance of a small angular deviation of the step wall from the vertical.

3.1.2 Effect of Tilt in the Stepwall

Let the orientation of a step etched wall in the PWG be such that it makes a small angle Φ with the vertical direction. A TWG fabricated on such an inclined step-etched PWG is illustrated in Figure 3.7a. From the geometric optical point of view one can see from Figure 3.7b that the wave front of the guided wave in the PWG will now be incident on the step wall at an angle $(\pi/2-\theta_g-\Phi)$ where θ_g is the angle which the modal ray in the film makes with the normal. This will result in a change in both the phase and the amplitude of the transmitted beam in the junction plane from the case of the vertical wall.

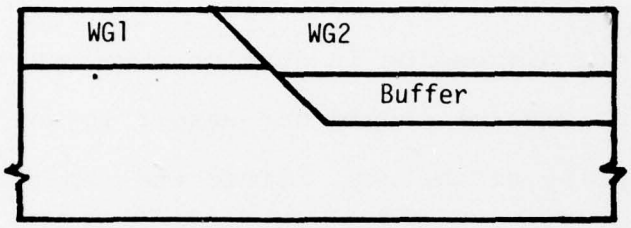

Figure 3.7a Schematic Diagram of Inclined PWG-TWG Junction

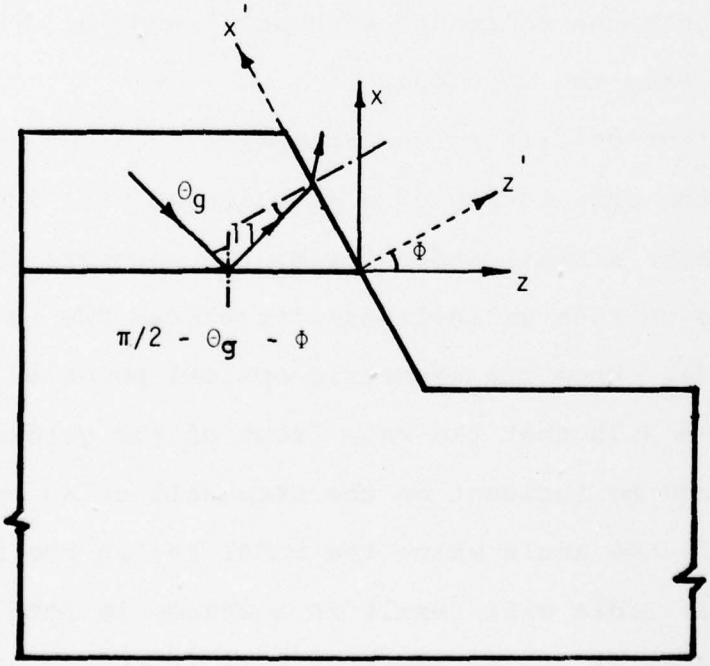

Figure 3.7b Transmission of Modal Ray at the Inclined Step-Wall.

An exact analysis of the coupling coefficient of a tilted junction plane is very complicated because waveguide fields are not orthogonal in this plane. However, for small tilt we can use a similar approach as developed in Section 3.2 by means of an appropriate correction to the phase and the amplitude of the guided wave fields of the PWG and the TWG.

Utilizing a coordinate transformation (see Figure 3.7b) (40)

$$x = x' \cos \Phi - z \sin \Phi$$

and

$$z = -x' \sin \Phi + z' \cos \Phi$$

We can rewrite Equation 3.6, for $z' = 0$ as

$$c_t = \frac{2\beta_1}{(\beta_1 + \beta_2)} \frac{\beta_2}{2\omega\mu} \int_{-\infty}^{\infty} E_y^{(1)} E_y^{(2)*} \cos \Phi \cos \Phi \, e^{-j(\beta_1 - \beta_2)\Phi x} dx \qquad (3.9)$$

The cosine and the exponential terms in the integral arise due to the amplitude and the phase corrections (40). Equation 3.9 can be numerically integrated to compute the coupling efficiency as a function of Φ. However, simplification in evaluating the integral analytically can result if we convine our interest to small values of tilt where the significant contribution to the integral comes from the terms due to phase distortion. In this case

$$c_t = \frac{\beta_1 \beta_2}{\omega\mu(\beta_1 + \beta_2)} \int_{-\infty}^{\infty} E_y^{(1)} E_y^{(2)*} e^{-j(\beta_1 - \beta_2)\Phi x} dx \qquad (3.10)$$

We have implicitly assumed ϕ to be small. An estimate of upper limit can be set by demanding the maximum phase deviation to be less than 20% of the phase constant ($\tilde{n}_f k_o$). For a GaAsP waveguide with film thickness 1.5 μm operating at 1.06 μm, this condition implies $\phi \leq 2.3^o$.

The variation of coupling efficiency between TE_0 modes of a $GaAs_{0.77}P_{0.23}/GaAs_{0.66}P_{0.34}$ feeding an $AZ1350/SiO_2$ TWG, as a function of tilt Φ, is shown in Figure 3.8. The plots are for $t_1=t_2=1.5$ μm and 2 μm. From this figure we see that for $t_1=t_2=$ 1.5 μm, a tilt of 2^ocauses only about 2% reduction in efficiency. Furthermore, the thicker waveguiding films exhibit higher sensitivity wrt tilt.

3.2 Effect of Separation on Coupling Efficiency

A separation, s, between the primary and the transitional waveguides causes the PWG field to diffract before it is incident on the aperture of the TWG. The effect of the diffraction due to a small separation (in Fresnel field) is merely to introduce a phase factor $e^{-j\beta_1 s}$ at the aperture of the TWG. This does not result in any change in coupling. However, for large separations, about 10 μm for GaAsP waveguides (λ = 1.06 μm) and about 15 μm for $LiNbO_3$ waveguides ($\lambda=6328a^o$), significant reduction in coupling can take place. For the proposed TWG, the separation is less than 2 μm; hence no significant loss in coupling efficiency is expected.

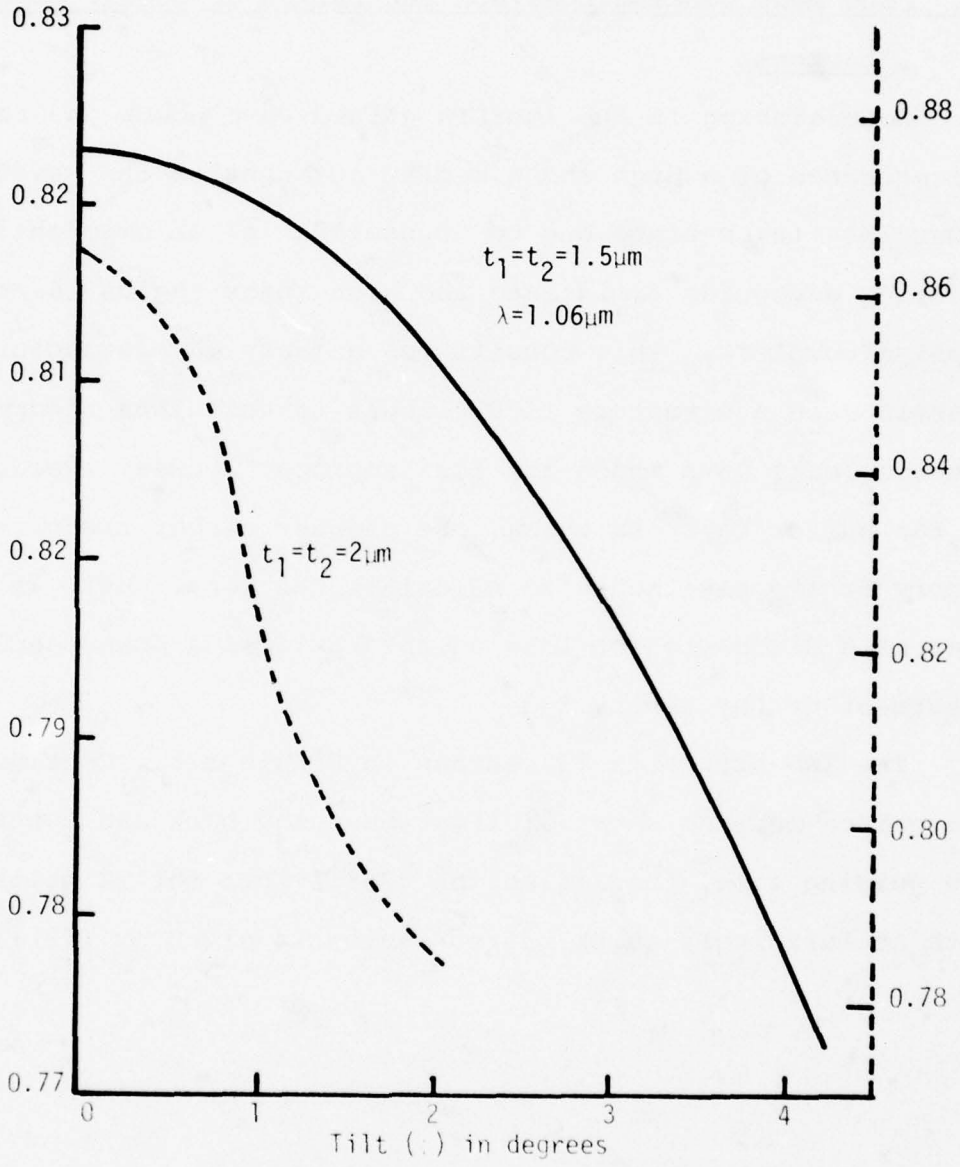

Figure 3.8 Coupling Efficiency as a Function of Tilt
PWG: $GaAs_{0.77}P_{0.23}/GaAs_{0.62}P_{0.38}$
TWG: AZ1350/SiO_2

3.3 The Mode Sinking Loss and the Design of Buffer Layer Thickness

Mode sinking is the loss in guided wave power due to the presence of a high index medium adjacent to the waveguide. Power loss takes place due to "tunneling" of an exponentially decaying waveguide field into the high index region (as in a prism coupler). This constitutes a leaky wave structure. Loss in such a structure is difficult to calculate rigorously because leaky wave modes are the "improper" modes. However, if the buffer layer is thick, one can use either the perturbation theory or the ray theory to calculate the loss. Here we will present a discussion of loss on the basis of a phenomenological treatment of Ray theory.*

The TWG structure is redrawn in Figure 3.9. Considering the guided mode as a ray of light bouncing back and forth in the guiding film, the reflection coefficient for TE polarization with an infinitely thick buffer region is given by (42):

---

*Ray theory gives the same results as the perturbation theory formulated by W.S.C. Chang (41).

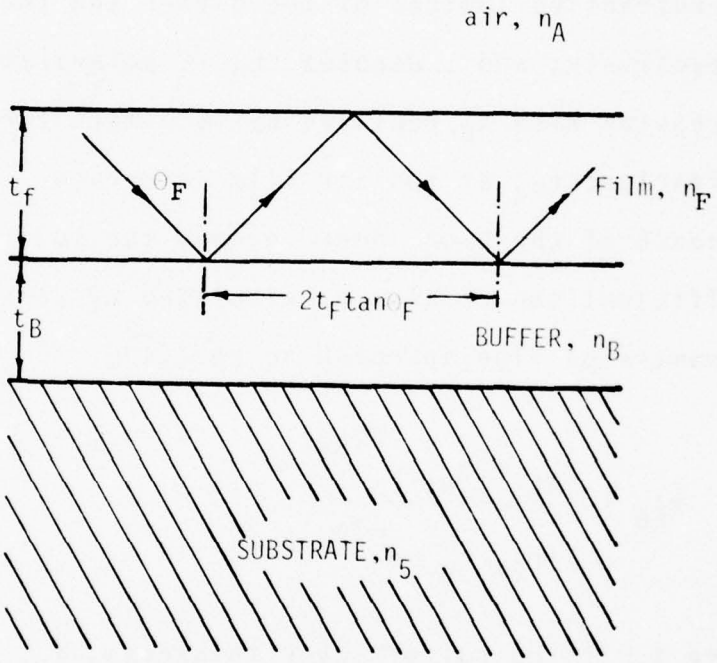

Figure 3.9 Propagation an Optic Ray in a TWG

$$r_{FB\perp} = \frac{\cos\Theta_F - 1^{\circ}\sqrt{\sin^2\Theta_F - (n_B/n_F)^2}}{\cos\Theta_F + 1^{\circ}\sqrt{\sin^2\Theta_F - (n_B/n_F)^2}} \tag{3.11}$$

where $\Theta_F = \sin^{-1}(B/n_F k)$ is the angle that the modal ray makes with the normal to the waveguide interfaces; n_B and n_F are the refractive indices of the buffer and the film regions respectively; and $\perp$ denotes the TE polarization. A similar expression with n_B replaced by 1, exists for the reflection coefficient r_{Fa} at the air-film interface. With the presence of the high index region, the modified reflection coefficient can easily be calculated by an x-direction transmission line approach to be. [43]

$$r'_{FB} = \frac{r_{fB} + r_{Bs}\, e^{-2q_B t_B}}{1 + r_{FB}\, r_{Bs}\, e^{-2q_B t_B}} \tag{3.12}$$

where t_B is the buffer layer thickness, r_{Bs} is the reflection coefficient at buffer-substrate interface given by

$$r_{Bs} = \frac{1^{\circ}\sqrt{n_F^2 \sin^2\Theta_F - n_B^2} - \sqrt{n_s^2 - n_F^2 \sin^2\Theta_F}}{1^{\circ}\sqrt{n_F^2 \sin^2\Theta_F - n_B^2} + \sqrt{n_s^2 - n_F^2 \sin^2\Theta_F}} \tag{3.13}$$

$$q_B = k_0 \sqrt{n_F^2 \sin^2\Theta_F - n_B^2} \tag{3.14}$$

and n_s is the refractive index of the substrate region. The power lost at each reflection is given by

$$P = 1 - r_{Fa}^2 \cdot r_{FB}^2 \tag{3.15}$$

where r_{Fa} is the reflection coefficient at the film-air interface. The distance between two reflections is $2t_F \tan\theta_F$. Hence, the attenuation per unit length is given by

$$\alpha = \frac{1-r_{Fa}^2 \cdot r_{FB}'^2}{2t_F \tan\theta_F} \tag{3.16}$$

Since $r_{Fa}^2 = 1$ (for total internal reflection), α can be written as

$$\alpha = \frac{1-r_{FB}'^2}{2t_F \tan\theta_F} \tag{3.17}$$

It should be noted that r_{FB} will vary from a value $r_{Fs} = (n_F \cos\theta_F - n_s \cos\theta_s)/n_F\cos\theta_F - n_s\cos\theta_s$ for $t_B=0$ to r_{FB} when $t_B \to \infty$. The variation of $|r_{FB}'|^2$ with t_B for the TE_0 mode of AZ1350/SiO_2/GaAs at 1.06μm wavelength is shown in Figure 3.10. It is seen that the reflection coefficient becomes unity at a buffer layer thickness of about 1μm.

Attenuation loss given by Equation 3.17 for a Glass/SiO_2/GaAs TWG structure is plotted as a function of t_B in Figure 3.11. From this data we see that an SiO_2 thickness of about 2μm offers adequate isolation. For TWG's where the difference $(n_F - n_B)$ is smaller, a larger buffer layer thickness is required in order to offer complete isolation from mode sinking.

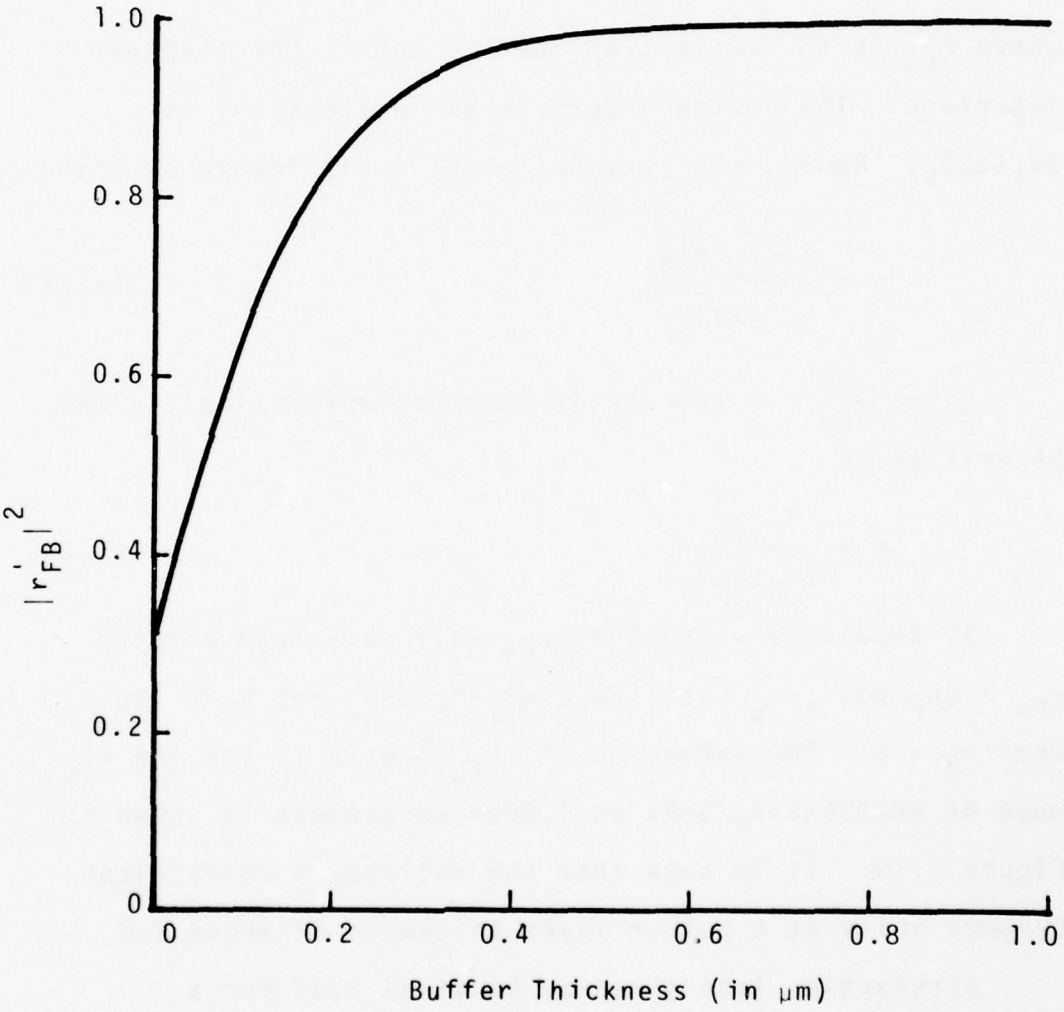

Figure 3.10 Variation of Power reflection Coefficient, $|r'_{FB}|^2$, at the film-buffer interface as a function of buffer thickness (TWG: AZ1350/SiO_2/GaAs, λ=1.06μm)

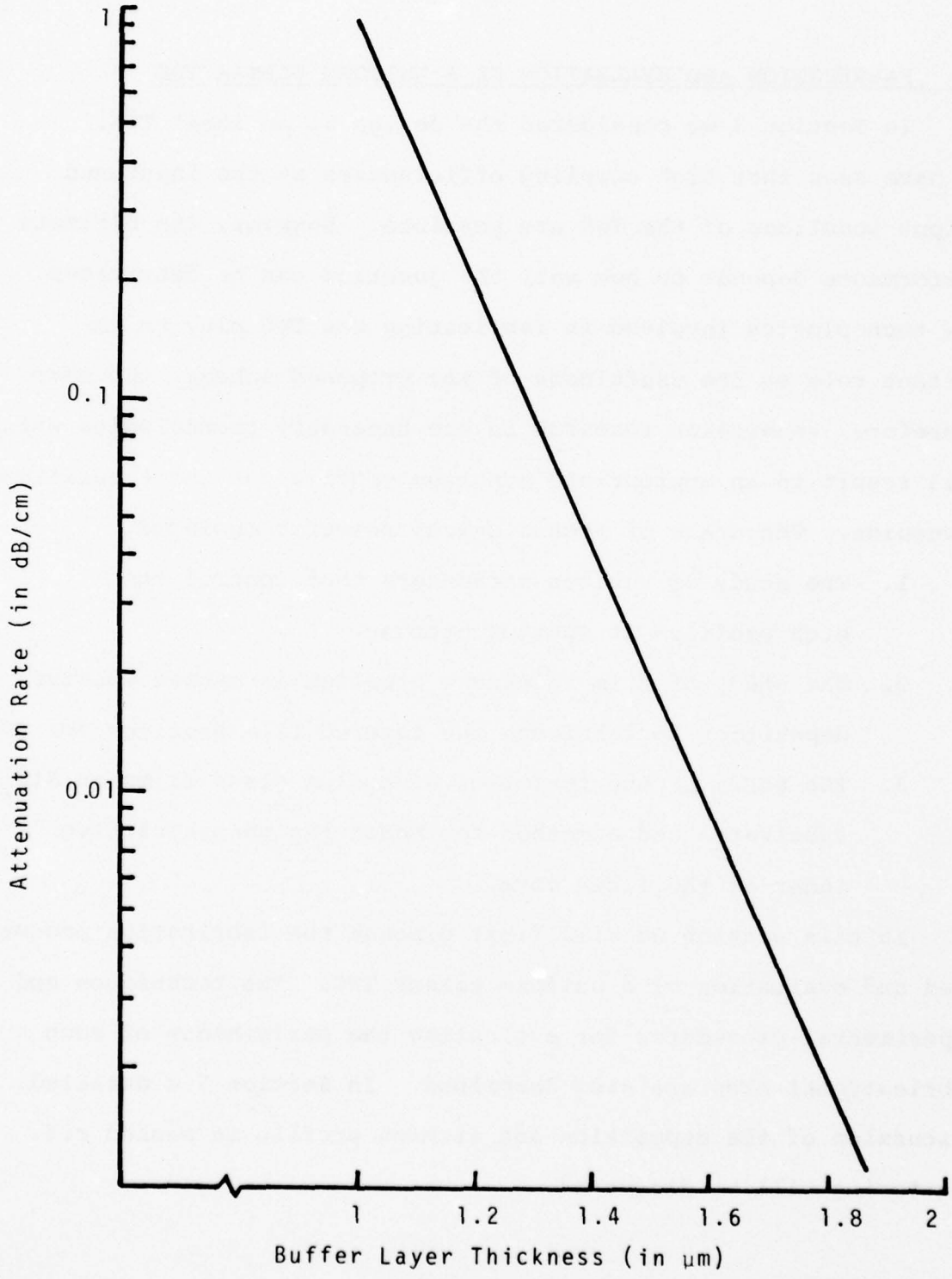

Figure 3.11 Calculated Attenuation Rate of the Glass/SiO_2 Transitional Waveguide on GaAs

4. FABRICATION AND EVALUATION OF A UNIFORM PLANAR TWG

In Section 3 we considered the design of an ideal TWG. We have seen that high coupling efficiencies at the input and output junctions of the TWG are possible. However, the ultimate performance depends on how well the junction can be fabricated. The technologies involved in fabricating the TWG play an important role on the usefulness of the proposed scheme. We have, therefore, undertaken research in the necessary technologies which will result in an appropriate junction profile for the transitional waveguide, The areas of technological research included:

1. The study of various parameters that control the etch profiles in sputter etching.
2. The study of film thickness profiles in masked sputter deposition to fabricate the tapered film profiles for TVC.
3. The study of the formation of sodium glass films on SiO_2 substrates and a method for modifying the refractive index of the fiber core.

In this section we will first discuss the fabrication process used and evaluation of a uniform planar TWG. The techniques and experimental procedures for evaluating the performance of each fabricational step are also described. In Section 7 a detailed discussion of the deposition and etching profile in masked r.f. sputtering will be discussed.

4.1 Preparation of the Primary Waveguides

The primary waveguides used in this work were mostly $GaAs_{1-x}P_x$/$GaAs_{1-y}P_y$ heterostructures (x<y). The GaAsP heterostructure waveguides were grown by vapor phase epitaxy. A typical cross-section of such a waveguide is shown schematically in Figure 4.1a. It consists of a layer (~40 μm) of graded composition (P=0 to P=y+0.02) of GaAsP grown on 2° -off (100) oriented n^+ GaAs. Such a grading helps to relieve the stress due to lattice mismatch. Next, a layer (~ 40 μm) of alloy composition $GaAs_{1-y}P_y$ is grown; followed by a layer (typically 1-2 μm) of $GaAs_{1-x}P_x$. Figure 4.1b shows the photograph of a cleaved end after it was stained in a ferrocynide etch (44). This kind of waveguide, supporting only one or two modes has shown low attenutaion (~ 1.5-2 dB/cm) but multimode waveguides have exhibited considerable mode conversion due to surface striations (45). Figure 4.2a shows a typical checkerboard pattern possessed by these waveguides. A Dektak trace of the waveguide surface, Figure 4.2b, shows maximum surface variations of about 800 Å. These waveguides were excited either by a GaAs prism or by grating coupler (Pitch Δ=0.35 μm) etched on the waveguide, using hollographically generated photoresist masks (45). Characteristics of some of these waveguides are summarized in Table 4.1.

4.2 Fabrication of a Uniform Planar TWG

Fabrication of the uniform planar TWG involves three steps: (i) step-etching the PWG, (ii) deposition of a low index buffer layer, and (iii) deposition of the low index waveguiding layer.

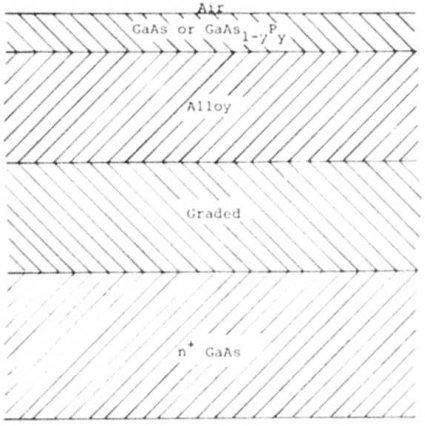

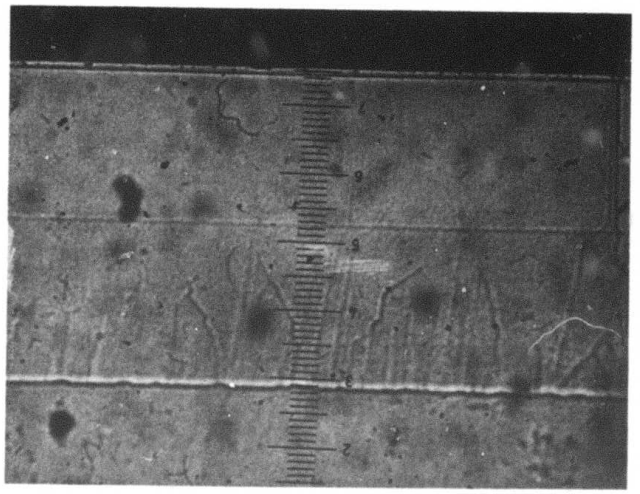

(a) (b)

Figure 4.1 (a) Schematic of GaASP heterostructure waveguide.
b) A photograph of a stained section of the waveguide. Each small division = 1.4μm.

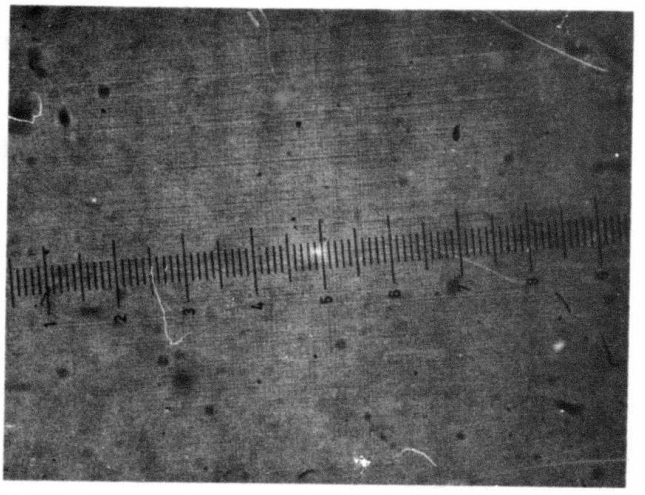

(a)

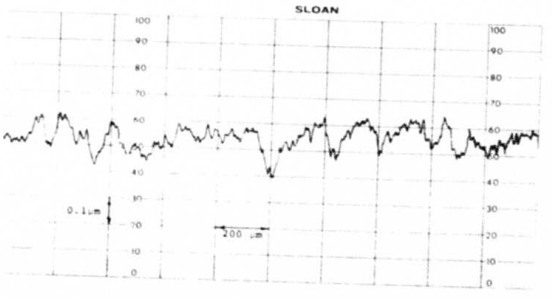

(b)

Figure 4.2 (a) A photograph of the checkerboard pattern on the GaASP waveguides caused by grading dislocations.

(b) A Dektak trace of the waveguide surface.

Table 4.1 Physical Properties of the Waveguides Evaluated

Wafer No.	Structure	Film Thick μm	Alloy Layer μm	Graded Layer μm	N_F $10^{14}cm^{-3}$	N_s cm^{-3}	R_{HS} cm^3/coul	ρ_s Ω-cm	u_s cm^2/v-sec
6-126	$GaAs/GaAs_{0.655}P_{0.345}$	1.5	43	43	3.4	1.1×10^{16}	558	0.17	3305
6-131*	GaAs/GaAsP	1	41	42	3.9	8.1×10^{15}	767	0.23	3288
6-187*	GaAs/GaAsP	1.6	39	43		5.1×10^{15}	1,227	0.31	3956
6-241	$GaAs/_{0.8}P_{0.2}/GaAs_{0.655}P_{0.345}$	1.2	44	41		2.9×10^{14}	21,090	5.56	3789
6-242	$GaAs_{0.77}P_{0.23}/GaAs_{0.66}P_{0.34}$	1.5	41	43		1.4×10^{14}	44,345	10.1	4393

*Alloy Composition P = 0.35

4.2.1 Step-Etching the PWG

From the discussion in Section 3, the desired depth of the step to be etched is 5-6 μm. To etch a vertical step with such a large depth and good edge quality is very difficult. There are basically two methods of etching a nearly vertical step. These are chemical and sputter etching (including ion milling).

Chemical etching for defining a vertical step makes use of a crystallographic (preferential) etchant which has high etching rates in certain crystallographic directions and very slow rates in others. The slow etching in some direction is due to the fact that these crystal planes are inert to the etchant. Such etchants are known for many materials, including Si and GaAs (46,47). An important consideration in chemical etching is the masking. Metal masks cannot be used for most acid etches, while alkaline etchants tend to attack SiO_2, which is commonly used as a masking material in device technology.

Several cyrstallographic etchants for GaAs, with different suitable masking materials, have been reported in literature (48). We have used an H_2SO_4: H_2O_2: H_2O etchant to etch a vertical step in the GaAsP waveguide through an SiO_2 mask. Such an etchant is very sensitive to the angular orientation of the wafer. Figure 4.3 shows the etch profiles when the mask edge is oriented along various direction on a (100) oriented GaAs wafer. Although a nearly vertical step can be etched if the mask edge is oriented along the (100) direction, we did not find chemical etching very useful for the fabrication of TWG because: (i) the uniformity of chemical etching over a large area is difficult to control, and (ii) the

(a) Mask edge along (0T1)

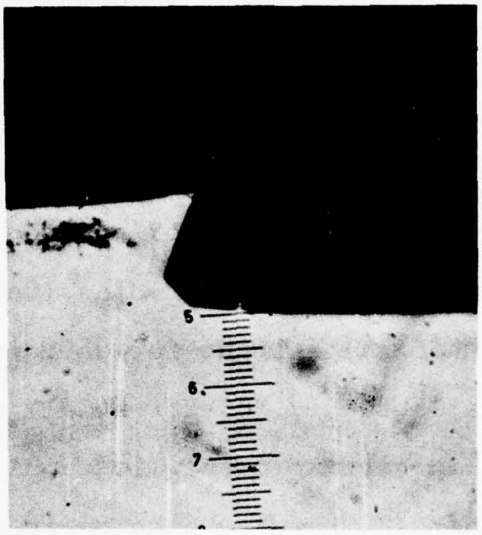

(b) Mask edge along (011)

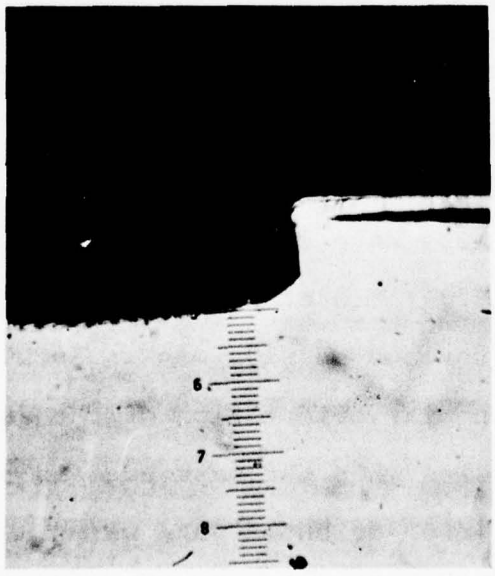

(c) Mask edge along (001)

Figure 4.3 Etch Profiles in Various Directions Using $H_2SO_4:H_2O_2:H_2O$ Etchant

inherent strain in the GaAsP heterostructure waveguides results in irregularities at the step edge which are not acceptable for this application. In view of the fact that chemical etching did not yield good results on GaAsP waveguides, we have developed techniques of sputter etching for this purpose. The advantage of sputter etching is that it can be used for all materials. Section 7 describes in detail the properties of the r.f. sputter etching about a vertical step. Here we will bring out specific results pertaining to the GaAsP waveguides used.

An important parameter (not discussed in Section 7), particularly significant for etching optical waveguides, is the energy of the bombarding ions. High energy bombardment is known to affect several properties on the surface layers of the etched wafer. These include surface topography and electrical and optical properties. The high energy bombardment causes formation of a highly disordered region (gross structural defects such as clusters of vacancies and interstitials in the vicinity of the incident ion). Jacobson and Wehner have experimentally determined this area to be about 50 surface atoms, i.e., ~15 Å radius (49). This kind of damage is unimportant for our device. The surface damages of our concern are the irregularities larger than several hundred angstroms.

We have experimentally observed the effect of power density in sputter etching on the surface topography. In low power density ($0.5w/cm^2$) a microscopic examination of the etched surface has shown that the topological damage is related to the pre-existing defect density of the sample. For example, on highly polished surfaces (SiO_2, Si, n^+ GaAs and $LiNbO_3$) the only noticeable difference before and after etching was that polishing damage became

visible after etching. However, GaAsP waveguides showed highly increased surface roughness. The surface roughness increased with the increase of power density and/or etching time. Figure 4.4 shows a photograph of etched and unetched surfaces of a GaAsP waveguide. The waveguide was etched for 6 hours at 15 m torr Argon pressure and 0.04w/cm^2 power density; a part of the waveguide was masked during etching to show the original surface. We have also observed that the waveguides etched at lower pressures (~3 m torr) resulted in better surface quality.

Initially, the GaAsP waveguides were etched at 15 m torr Argon pressure with the samples placed on top of a Ti target. A well cleaved piece of GaAs was used as the etch mask. Sputtering under these conditions resulted in a dark brown layer adhering to the etched area. This layer was not affected by inorganic acids and was very weakly dissolved in H_2O_2: H_2O: H_2SO_4. It was thought to be due to a preferential etching of one of the components of the GaAs-GaP compound from the surface layers of GaAsP substrates (under an oxygen deficient sputtering atmosphere). Consequently, the formation of such a layer was avoided by placing the sample on an Al electrode. Wafers so etched showed about an 8% "undershoot" (i.e. excess etch depth at the mask edge as compared to the depth away from the mask). Another problem faced in the earlier stages of step etching the GaAsP waveguides was that the edge of the step

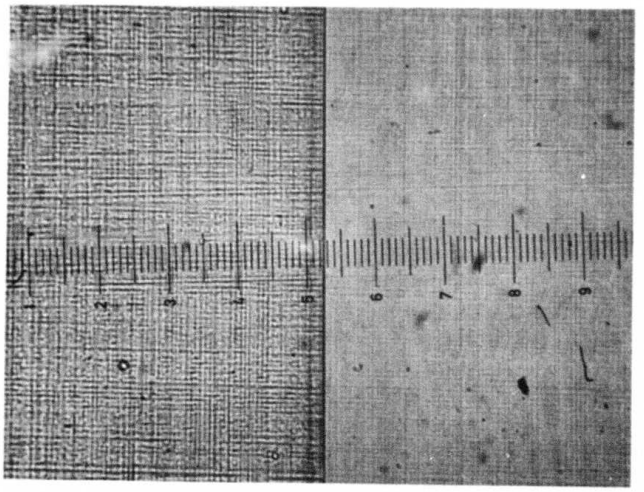

Etched Side

Figure 4.4 Effect of Sputter Etching on the Surface Topography Wafer 6-242B Was Etched for 6 Hours at 0.4 w/cm^2

often showed considerable roughness. When a guided wave propagating towards the step was excited on the unetched area of the waveguide, the radiation from the step showed a large spread in a direction parallel to the edge. Actual spread varied from wafer to wafer. A typical radiation pattern from such a step-etched GaAsP waveguide, excited at 1.06 μm wavelengths, is shown in Figure 4.5. The radiation pattern was photographed through an i.r. viewer from a semi-transparent screen placed close to the step. The edge roughness and the consequent scattering was thought to be due to "channeling" and "focussing" effects at the surface striations during sputter etching. Figure 4.6a shows, schematically, the incidence of bombarding ions along the surface of a groove. An enhanced etching rate occurs at non-normal incidence. Such an effect would be minimized if the surface roughness were smoothed by depositing a layer of SiO_2 prior to etching and by aligning the mask edge parallel to the lines of strain. This was found to yield excellent results.

An improvement in the step quality as a result of following this procedure can be seen by comparing the Figures 4.6b and 4.6c. Figure 4.6b shows the photograph of a step, etched without depositing an SiO_2 layer prior to etching. A corresponding photograph of a step in the same waveguide etched after depositing a 0.8 μm thick layer of SiO_2 and locating the mask edge parallel to

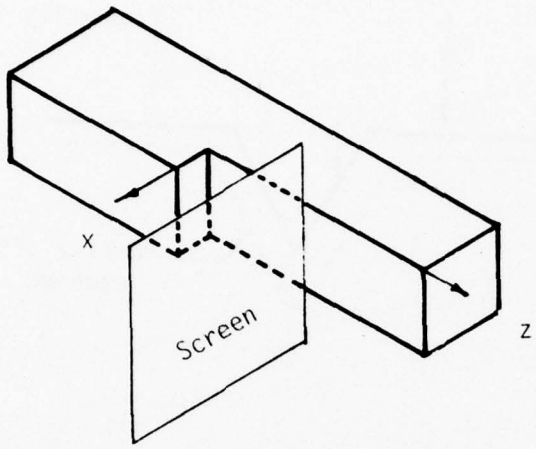

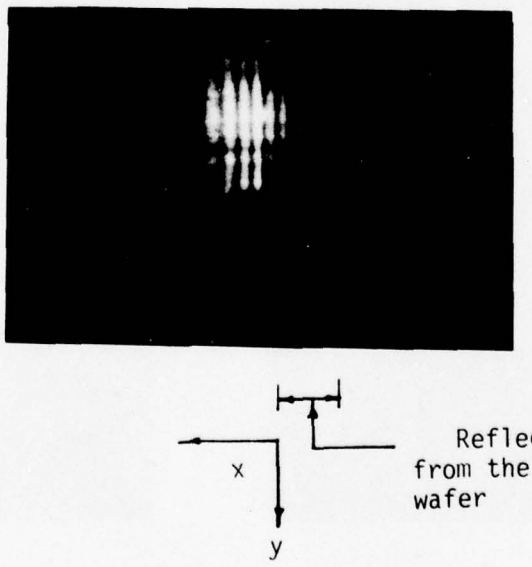

Figure 4.5 Photograph of a radiation pattern from a step in a GaAsP waveguide showing spread in the beam (along y direction) due to edge roughness.

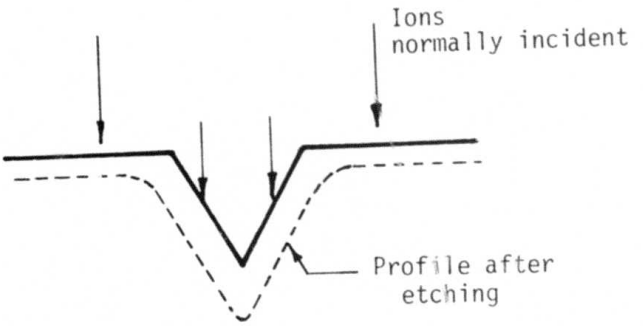

(a)

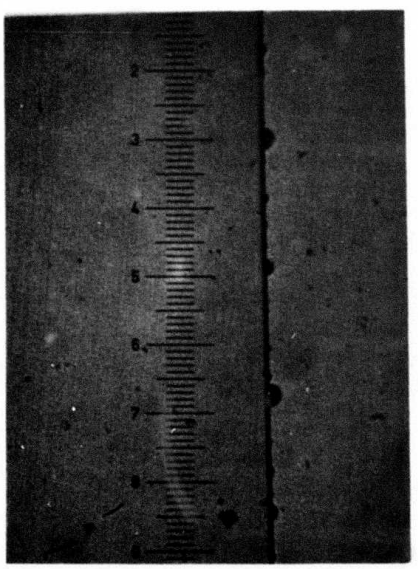

(b)

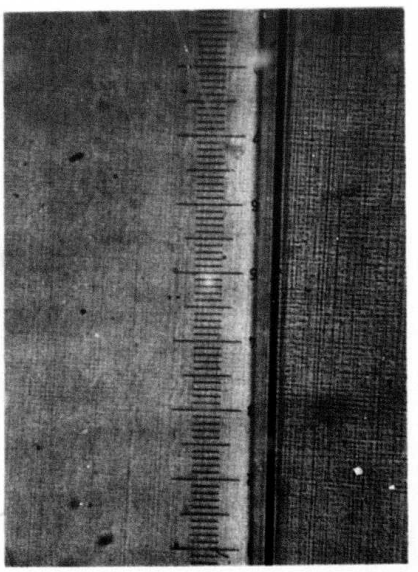

(c)

Figure 4.6 (a) A Schematic Diagram Showing the Effect of "Channelling".

Photographs of Step-Etch in GaAsP Waveguides Showing Edge Quality when Etched with Mask not Parallel to Strain Lines (b), and parallel to Strain Lines (c).

the strain lines is shown in Figure 4.6c. When a guided mode is excited on the waveguide that has been etched with the mask parallel to the lines of strain, the radiation pattern clearly shows discontinuities corresponding to the striation. Figure 4.7 shows radiation from the sample VR6-242 etched 7 μm deep; the lines parallel to the step wall are due to the filamentary excitation of the guided wave.

It should be pointed out that a pronounced "undershoot" in the etched section of the waveguide is highly undesirable. Such an undershoot is not filled up during the sputter deposition of buffer and low index guiding films*. This results in a large discontinuity (a valley) at the junction, which causes coupling loss. As described in Section 7, the undershoot can be reduced by etching at low pressure.

Figure 4.8 shows the Dektak trace of the surface profile of a $GaAs_{1-x}P_x/GaAs_{1-y}P_y$ (x=0.23, y=0.34) waveguide etched under 4 m torr of Argon pressure at 50 watts of r.f. power for 4 hours 50 minutes. The etched depth is 5.7 μm and the undershoot is 5.9%. Figure 4.9 shows the photograph of the etched and unetched surfaces from an optical microscope at 500X magnification. Notice the excellent surface quality of the etched section as compared to the unetched section. Figure 4.10a shows the radiation pattern emerged from the etched edge while Figure 4.10b shows the measured

*See Section 4.2.2 and 4.3.3 for more details.

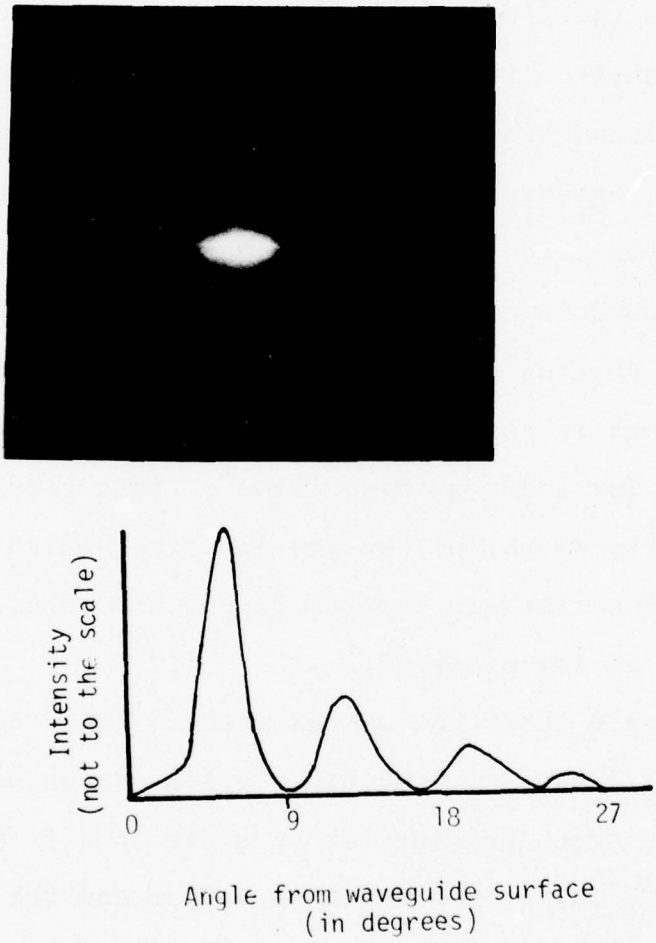

Figure 4.7 Radiation Pattern Corresponding to a TE_0 Mode of a GaAsP Waveguide Etched 7μm deep, Showing the Guided Wave Power in Two Filaments.

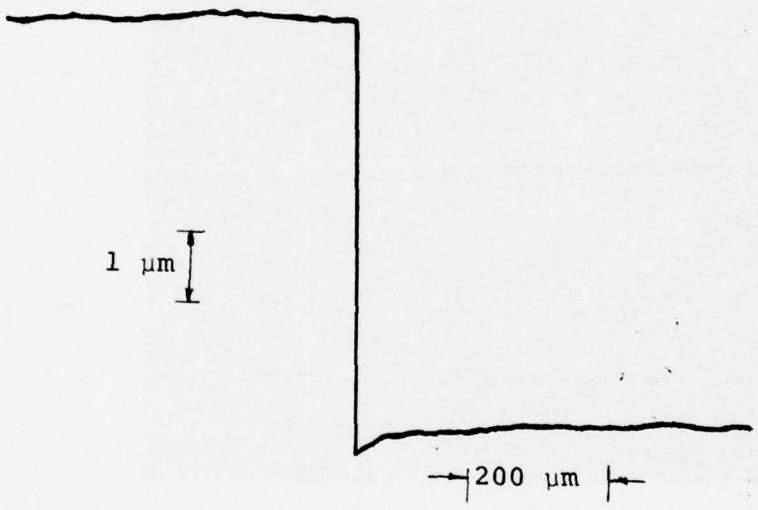

Figure 4.8 Surface Profile of the GaAsP Waveguide Etched under 4 m torr of Ar.

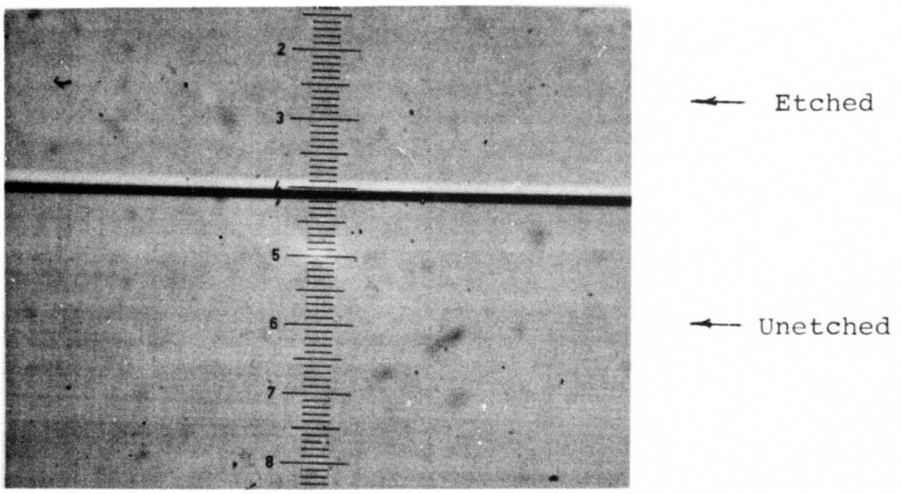

Figure 4.9 Photograph of the GaAsP Waveguide Surface after Step Etching at 500X

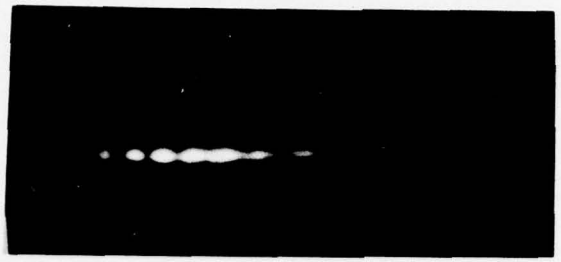

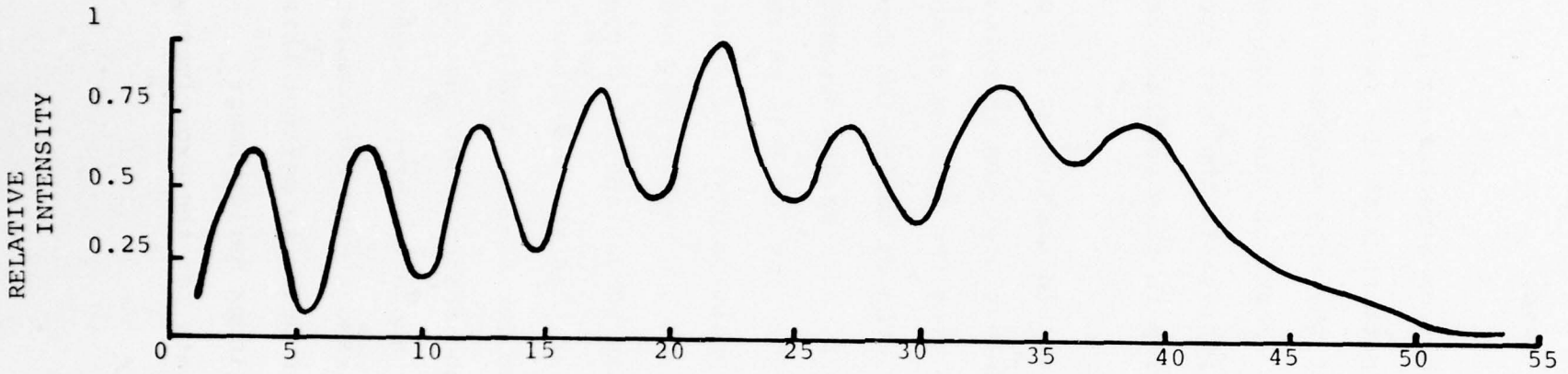

Figure 4.10 (a) A photograph of the radiation pattern from the step etched wall through an i.r. viewer

(b) Measured radiation pattern for the step etched wall.

radiation pattern obtained from a mechanically scanned detector. Comparing this radiation pattern with the radiation pattern shown in Figure 4.5, we see that the edge roughness is much reduced. There is an insignificant amount of radiation spread caused by scattering. This sample represents the best etching profile that we have been able to develop in this contract using the r.f. sputtering technique.

However, a disadvantage in etching at low pressure is that the etching rate is low unless high ion energies are used. An alternate approach for solving the problem of the undershoot is to bill up the undershoot area by making two depositions of the buffer layer; one consisting of a masked deposition localized on the etched area near the junction (to fill up the undershoot) and the other as a uniform deposition over the entire etched area. In view of the relation between the mask height and etch profile (Equation 7.4) and the mask height and the deposition profile (Equation 7.3), it is clear that the undershoot can be filled if a deposition of the buffer material is made through a mask located at a height h, equal to the thickness of the etch mask and with its edge located directly above the step. However, our initial attempts to fill the undershoot were not completely successful. More research is needed in order to perfect this technique.

4.2.2 Deposition of Low Index Buffer Layer

The low index substrate for the experimental TWG was chosen

to be SiO_2. The buffer layer can easily be sputter deposited. However, from the discussion in Section 7.1, we see that a sputter deposition of SiO_2 near a step of height h will have two effects. Firstly, the step wall will accumulate an SiO_2 thickness of about $0.6t_B$ where t_B is the buffer layer thickness away from the step. This implies that, in effect, the PWG and the TWG will be separated by a few micrometers. The effect of a few micrometer separation between PWG and TWG is not expected to cause any significant change in the coupling efficiency. Secondly, due to a shadowing effect of the step, there is a non-uniformity in SiO_2 film thickness extending approximately to a distance h from the step. An exact profile due to an infinite target is described by Equation 7.2. For a finite source, the parameter R that determines the profile is defined as the ratio of source-to-substrate distance to source diameter. Film profiles for two values of R are schematically shown in Figure 4.11 (50). From the figure we notice that for small values of R a crack is formed where the horizontal and vertical films join. The crack formation is reduced as R increases.*

The deposition of SiO_2 was carried out in a sputtering system with R=0.65. Ideally, SiO_2 should be deposited only over the etched region. However, since the deposition of a low index layer

---

*One can clearly see that by using a point source for the deposition, the SiO_2 profile at the step will approach the ideal profile shown in Figure 2.7. A point source approximation can easily be achieved in vacuum evaporation (e.g., by utilizing electron beam vaporization). Such a conclusion also follows directly from the cosine distribution of the material evaporated if the step is located directly above a point source and far away from it.

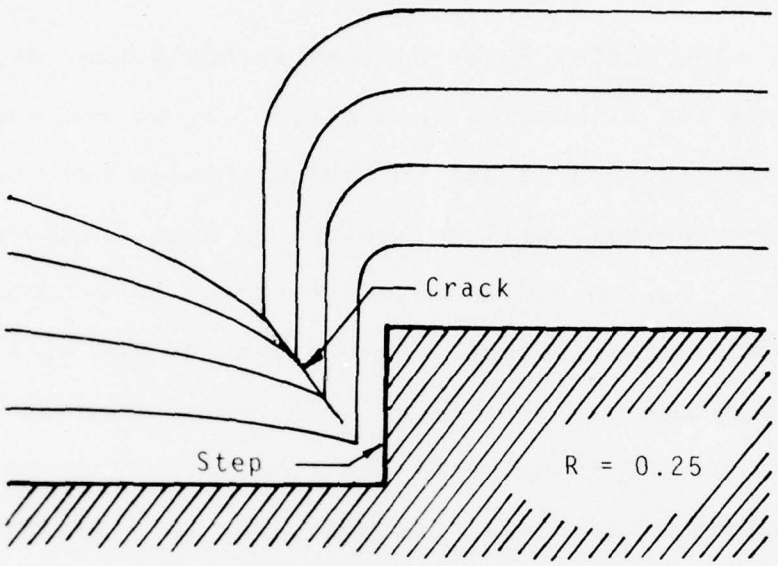

(a)

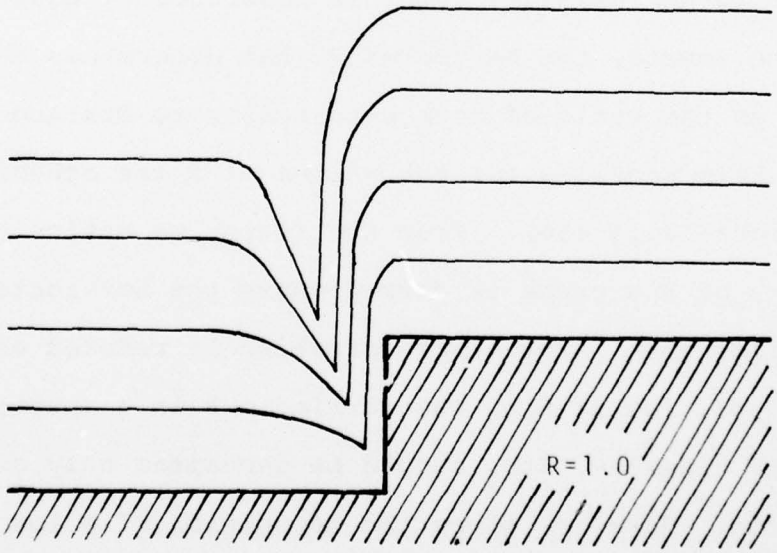

(b)

Figure 4.11 Step Coverage in Sputter Deposition (a) R < 1 and (b) R = 1

on the PWG will not affect its waveguiding properties significantly, it is easier to carry out the deposition by placing a mask a short distance from the step over the unetched area. But such a mask will cause a sharp nonuniformity in the thickness of the SiO_2 layer near the step. Such a discontinuity is likely to cause a loss of coupling efficiency due to scattering. A way to circumvent this problem is to smooth out the discontinuity by using a thick mask located at the step during the SiO_2 deposition. Such a mask could in practice be the same as the etching mask if SiO_2 deposition can be made in one pump down.*

We have fabricated TWG's on GaAsP PWG's using both methods of SiO_2 deposition, i.e., with and without the mask at the step. In one case, SiO_2 was deposited with the mask away from the step to fabricate a TWG of AZ1350/SiO_2 on a GaAsP PWG. In the second case, SiO_2 was deposited with the mask placed at the step (i.e., the deposition and the etching were carried out in one pump down without moving the mask). We found that the coupling loss is not affected significantly by the mask position.

4.2.3 Deposition of Low Index Guiding Layer

We have seen that even with an ideal step, the sputter deposition of SiO_2 results in a valley near the step. A similar valley will result if the low index guiding layer is sputter deposited. We have, therefore, investigated both solution-

*This would also necessitate placing the waveguide on a silica target during sputter etching.

deposited and sputter-deposited guiding films to study the TWG performance. A solution-deposited film may fill up the dip and result in a smooth transition.

The solution-deposited guiding layer for the TWG at 1.06 μm operation was AZ1350B. The waveguide after etching and deposition of SiO_2 was coated with a layer of the photoresist. A few drops of AZ1350 were put on the etched side and the photoresist was then allowed to dry with the wafer tipped about 10° with the etched side upwards . The wafer was then baked at $80^{\circ}C$ for 10 minutes and developed, followed by a post bake at $80^{\circ}C$ for 10 minutes.

We have also sputter deposited BaO-glass on SiO_2 to form the TWG. For the sample that has the surface profile of etched GaAsP with SiO_2 deposition as shown in Figure 4.12, a layer of BaO-glass is deposited on that sample with a mask placed about 1 mm away from the step. The BaO glass deposition was carried out at 15 m torr of Argon pressure and 400 Watts of r.f. power. The total thickness of the BaO-glass layer is 2.1 μm. Figure 4.13 shows the Dektak trace of the surface after BaO-glass deposition. Notice that the unetched surface of the primary PWG and the BaO-glass surface of the TWG are registered. There is a small dip (about 0.4 μm deep) caused by the undershoot in the etching and deposition processes.

4.3 Evalution of the Coupling Efficiency

To evaluate the TWG, the coupling efficiency, defined as the ratio of the power transmitted in the desired mode in the TWG to

Figure 4.12 Surface Profile of the GaAsP Step Etched Waveguide after SiO_2 Deposition

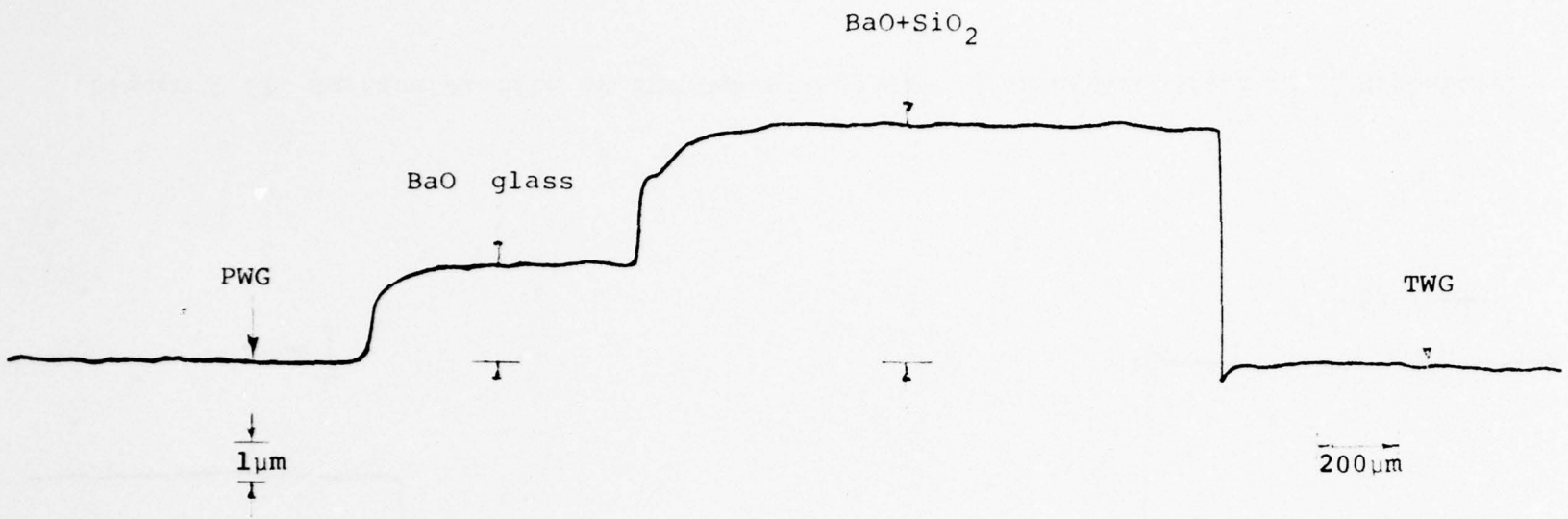

Figure 4.13 Dektak Trace of the Surface Profile of the PWG and the TWG after the BaO glass Deposition

the power incident at the step junction in the incident mode of the PWG is measured as follows:

A guided mode of the primary waveguide is excited. The guided mode power in the TWG is measured at various distances from the junction. By extrapolation, the power at the junction in the TWG is determined. Power at the junction in the PWG is determined from the input prism coupling efficiency and the attenuation rate of the waveguide. For GaAsP waveguides the input efficiency of a GaAs prism is very low (<0.1%). In this case the power at the junction in the PWG is determined directly from another piece of waveguide (test waveguide) cleaved from the same GaAsP wafer. The test wafer is excited similarly, and its propagation length is adjusted to be the same as that of the PWG. The power P_a at the end of the waveguide radiating into the air is measured. Hence, the power at the junction of the PWG is Pa/T where T is the transmission coefficient at the test waveguide end $T = 1-(n_f-1/n_f+1)^2$. The measured coupling efficiencies for various waveguide combination and their parameters are shown in Table 4.2.

Two features that are used commonly to identify high coupling efficiencies are:

1. The absence of radiation at the junction.
2. A single m-line output from the TWG.

These features have also been examined for the TWG's fabricated in this contract. Figure 4.14 shows a photograph, taken through an

Table 4.2

Coupling Efficiencies Between Various Primary

and Transitional Waveguides

High Index Waveguide			Low Index Waveguide				
	Film thick m	No. of modes	Material	Film thick away from m	No. of modes	λ in μm	η in percent
(a) $GaAs_{.77}P_{.23}/GaAs_{.660}P_{.34}$	1.5	1	$AZ1350/SiO_2$	1.7	2	1.06	.77
(b) $GaAs_{.800}P_{.20}/GaAs_{.665}P_{.345}$	1.2	1	$AZ1350/SiO_2$	2	3	1.06	.5
(c) $GaAs_{.77}P_{.23}/GaAs_{.66}P_{.34}$	1.5	1	$BaO\ glass/SiO_2$	2.1	---	1.06	.64

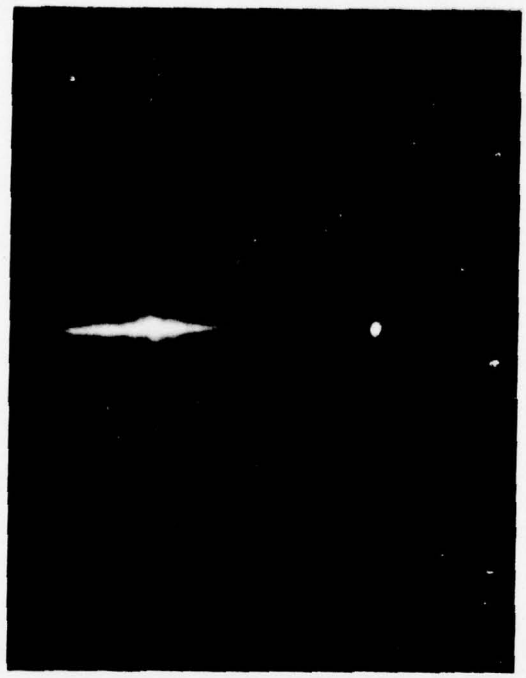

Fig. 4.14 Photograph of the Scattered Radiation from the GaAs Waveguide and the Transition Waveguide

i.r. viewer, of the coupling of a guided wave from a PWG (GaAsP) to a TWG(AZ1350/SiO_2). The guided wave excited on the PWG continued past the junction as the guided mode of AZ1350/SiO_2 without any noticeable scattering at the junction. On the other hand, output of a low efficiency TWG is shown in Figure 4.15. A TE_0 mode was excited on the primary waveguide and the output taken with a flint glass prism. Notice that there is considerable scattering of power into the substrate and higher order modes (in addition to radiation into the air - not in the picture). By reducing the input beam diameter at the PWG to a width of a few striations, the mode conversion between guided modes was reduced, as seen in Figure 4.15b. In contrast, the m line structure of the radiation coupled out from waveguide (c) of Table 4.2 shows only a single line.

Two interesting features in high efficiency coupling were observed in the reverse coupling; i.e., when a guided wave is excited in the TWG at the opposite end from the PWG. The reverse coupling efficiency is less than the forward case. This is believed to be caused by a large coupling coefficient of a low index waveguide mode to radiation modes due to the deviation of the etch profile from a perfect step. For waveguide (a) in Table 4.2, when m=1 was excited, there was no observable power transmitted to the primary GaAsP waveguide. Since the PWG is a single mode guide, this shows that the mode conversion at the junction is very small.

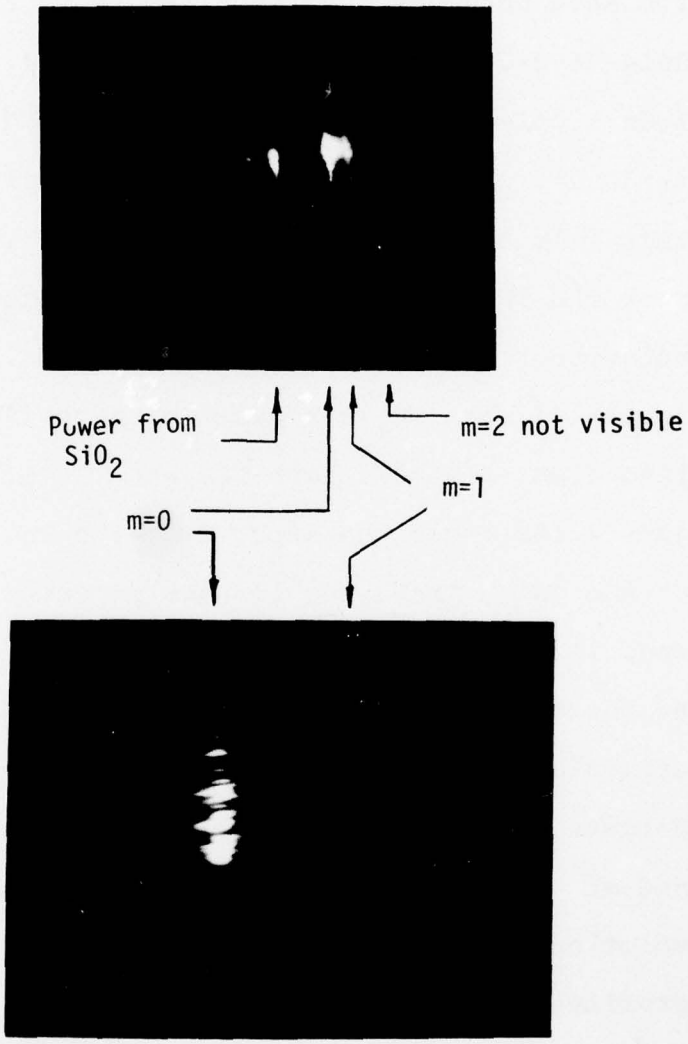

Figure 4.15 Photographs of m-Lines from an AZ1350/SiO_2. TE_0 Mode Way Excited on the PWG.

Although no systematic experiments were done to determine the coupling efficiency as a function of the film thickness t_2 of the TWG (for a given thickness of the primary waveguide, t_1), certain results have been observed in $LiNbO_3$ waveguide in Navy Contract (N00014-76-C-0796) when $t_2 >> t_1$. Figure 4.16a shows output coupled from a polyurethane/SiO_2 TWG on a $LiNbO_3$ primary waveguide, with $t_2 \sim 10$ μm, when TE_0 of the PWG was excited at 6328 Å*. The TWG for this film thickness has 13 modes. It is clear that all the modes of the TWG were almost equally excited with no observable radiation into the substrate or the air. Similar results were obtained when TE_1 was excited on the PWG. In the reverse coupling (TWG excited), both TE_0 and TE_1 of the PWG were excited. Figure 4.16b shows the ouput from the PWG when TE_{10} was excited on the TWG. These results are expected from the theory developed in Section 3, and they have very important implications to the use of hollow dielectric TWG discussed in Section 6.

The experimental results presented in this section (Table 4.2) have clearly demonstrated high efficiency (close to theoretical values) can be obtained at the PWG-TWG junction. However, due to the softness of solution-deposited films and difficulty in controlling their taper profiles (for TVC), the use of the TWG's fabricated with these films is limited only to laboratory experiment. The BaO-glass/SiO_2 TWG is rugged. But the measured coupling efficiency

*Results obtained in Navy Contract, N00014-76-C-0796, are used here to illustrate the point.

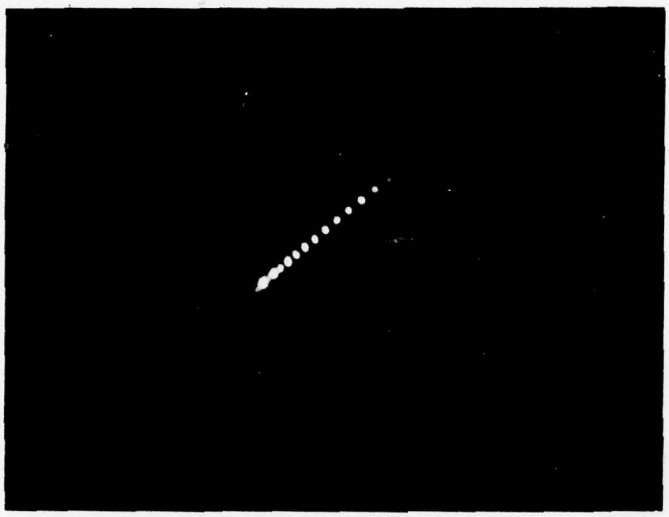

Figure 4.16a
Showing the Output of a 13 Mode Polyurethane TWG when TE_0 was Excited on the Primary WG.

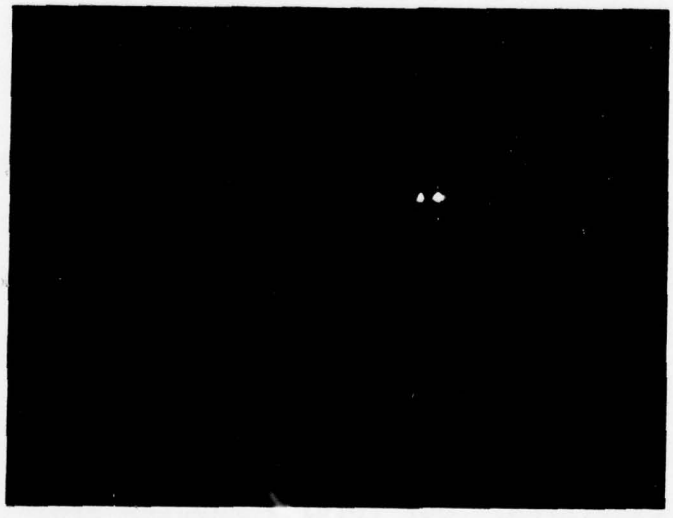

Figure 4.16b
Showing the Output of the PWG when TE_{10} was Excited on the TWG.

m=0 m=1

is not as high as the AZ1350/SiO_2 TWG because of the scattering loss of the surface dip at the step. Our measurement showed that 25% of the power is loss at the junction in the form of the scattered radiation from the surface dip. More experimentation with the deposition technique to fill this dip should increase the efficiency to more than 80%.

5. THE FABRICATION AND EVALUATION OF STRUCTURES FOR CYLINDRICAL TO PLANAR WAVEGUIDE TRANSITIONS.

In order to match the planar geometry of the waveguide to the cylindrical geometry of the fiber, we have first experimented with the fabrication of a fiber horn. Later we experimented with the fabrication and evaluation of tapered waveguides, i.e., a transition structure that converts the energy in a primary planar waveguide to a channeled waveguide and that is compatible with our TWG materials. Fabrication and evaluation of sodium-glass waveguides were undertaken so that ion exchange can be used for realizing the tapered structure. The detailed results of these studies are presented in the following subsections to show (a) that an efficient fiber horn is very difficult to realize and (b) that the realistic approach is to use a Na-glass tapered waveguide for such transition. However, within the present contract period, we were only able to obtain some initial results in the efficiency of the tapered transition. Our initial results are insufficient for assessing the ultimate efficiency that can be achieved in such a tapered waveguide.

5.1 The Fiber Horn

The initial idea was to heat an existing fiber to its plastic temperature range and then to apply mechanical pressure to the softened fiber to deform it into an elliptical shape. If such a horn can be fabricated without creating excessive scattering loss, the dominant mode of the fiber core will be transformed adiabatically into the dominant mode of the elliptical fiber. The mode of the elliptical fiber will have a long evanescent tail because the thickness of the core is small. Additionally, the cladding material will be thin. Consequently, there will be a significant amount of the energy in the evanescent tail outside of the cladding material in the air, convenient for the coupling to the waveguide by the tapered velocity coupling method. The broadened width of the elliptical waveguide means also that the beam, once coupled into the waveguide, will remain collimated in the horizontal direction. The key to success is naturally how to deform the fiber without creating a large number of scattering centers.

During this contract period, we have investigated experimentally the fabrication of such a fiber horn by two different methods. These experiments are discussed in the following subsections. From these experimental results, we concluded that the difference of the thermal properties of the cladding and core material will not allow us to fabricate a low-loss fiber horn in silica-boro-silicate fibers by this method.

5.1.1 The Fabrication of the Fiber Horn by CO_2 Laser Direct Heating

Initial experiments were conducted with multimode glass fibers in order to evaluate and to optimize the basic mechanical process involved in heating a cylindrical fiber and forming it into the desired taper. CO_2 laser radiation was used to heat the fiber because it is clean, its power can be controlled accurately, and it is absorbed effectively by the fiber. A variable pressure pneumatic press was used to force a replaceable form vertically down against another such form. The surfaces of the two forms were optically polished to a planar configuration, and the relative angle and position of the lower form was accurately adjustable by micrometers. By preheating the last few millimeters of the glass fiber using side illumination from the CO_2 laser, a tapering section of up to 2 mm in length was produced by the controlled, rapid pressing of the plasticized fiber between aluminum forms.

This initial success with the glass fibers encouraged us to fabricate next the horns with multimode silica fibers. Anticipating the high softening temperature of the silica fiber, optically polished molybdenum was used for the mechanical forms. Molybdenum was chosen because of its high reflectivity at 10.6 μm, its high melting temperature, and its suitability for maintaining optical flatness under pressure. In order to obtain sufficient

energy density, the 50-watt, 10.6 μm CW laser radiation was focused onto the end of the fiber. However, the absorption coefficient of silica at 10.6 μm wavelength is so high and the thermal conductivity of the silica sufficiently low that the end of the fiber evaporated before a useful length (less than 1 mm) was heated above the softening temperature. Pulsing the laser radiation would give us much more accurate control of the heating of the fiber. We have pulsed the CO_2 laser and varied both the width and the repetition rate of the pulse at different power levels so that the maximum volume of the fiber was heated up to a temperature below evaporation. Evaporation was prevented by this method; but the pliable length of the fiber remained very small.

In order to provide the necessary thermal environment high density polished graphite forms were substituted for the molybdenum forms and CO_2 laser radiation was used to heat the forms, achieving an oven-like effect. However, 50 watts of CO_2 laser radiation was insufficient to heat up both the fiber and the graphite forms to a sufficiently high temperature. Subsequently, electrical resistive heating of the graphite form was used to soften the silica fibers.

5.1.2 The Fabrication of the Fiber Horn by Electrical Resistive Heating.

In this second method, the lower polished graphite form served also as the resistance heater. The upper form was appro-

priately remounted to provide the necessary tapering adjustment. A nitrogen atmosphere at 10 psi pressure was maintained around the pneumatic jig to prevent the oxidation of graphite. The forming process was observed by means of a stereo microscope positioned between the two forms at the tapering end of the fiber. The temperature of the fiber was monitored by an optical pyrometer.

Experimental results indicate that a sufficient amount of uniform heating can be produced by this method without oxidation of the graphite. Tapers with angles as small as 4° can be produced over a length of 1.5 mm. However, the softening temperature of the borosilicate cladding of the fibers was measured to be approximately $1325^{\circ}C$. At the softening temperature of the SiO_2 core, approximately $1625^{\circ}C$, the borosilicate cladding appears to liquefy and tends to attach to the graphite form. A number of horns from both the multimode and the single-mode fibers have been produced in this manner with the fibers heated to not more than $1650^{\circ}C$. In an attempt to minimize unnecessary heating of the borosilicate material, the temperature of the graphite form was controlled by feedback from the optical pyrometer. Best results were obtained with the lowest pressure applied to the form. Measurements of the produced horns before removal from the lower form indicate horns of the length of 2 mm and thickness of 20 μm have been obtained, corresponding to a cross-sectional aspect ratio of 15 to 1 at the end of the horn. Figure 5.1 is a photograph of a typical single-mode fiber horn fabricated in this manner. Notice

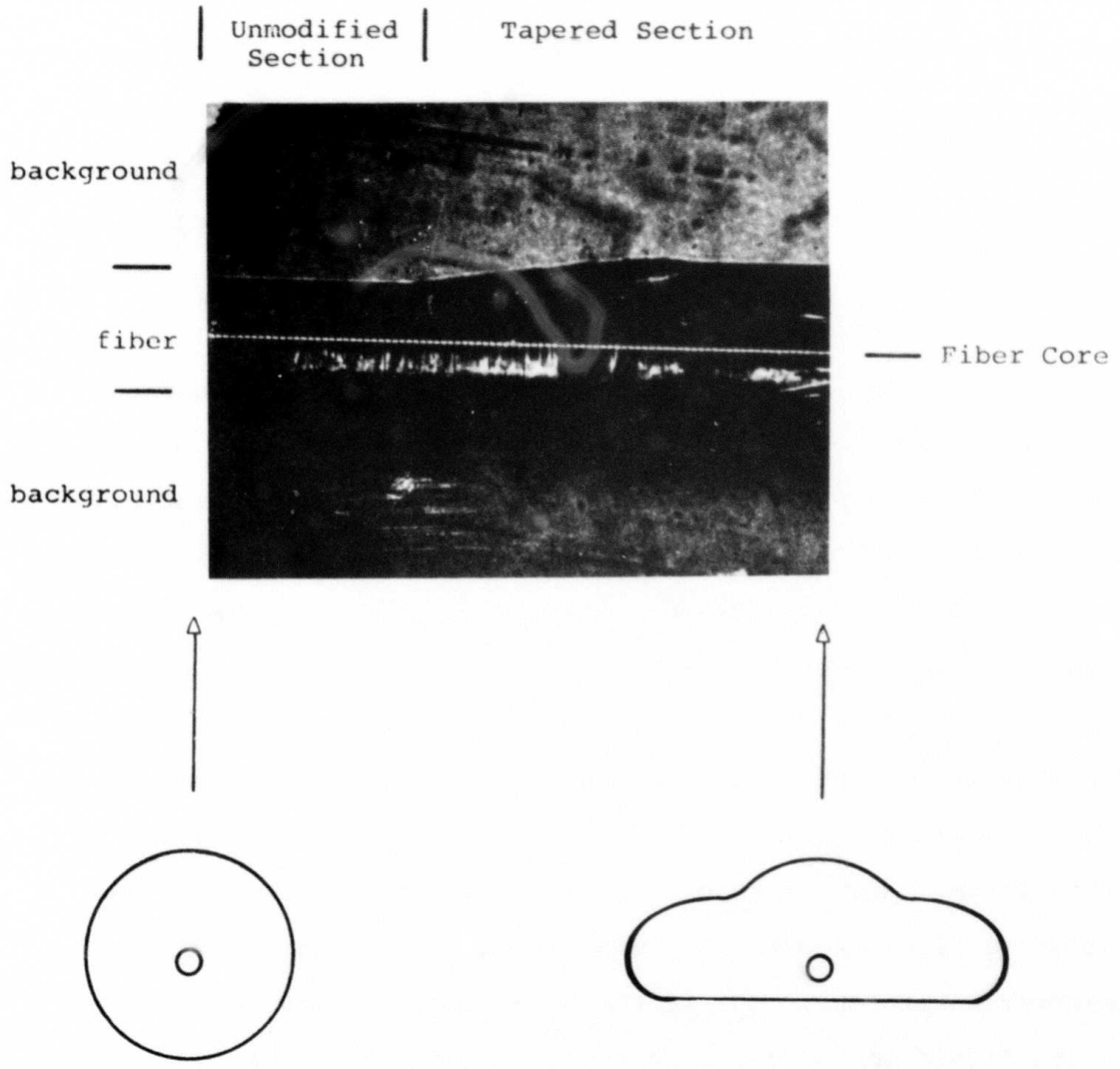

Figure 5.1 Photograph of Single-mode Fiber Horn

the very poor surface quality. The center white line is the core. In this particular case, the core seems to be intact while the cladding has already been badly corrugated. Fiber horns obtained by heating to a higher temperature showed a much greater degree of surface degradation. Removal of the tapers from the lower forms always resulted in the breakage of the horn at a thickness of approximately 35μm due to the adhesion of the borosilicate glass to the form.

From these results, we reached several conclusions: (1) Obviously the silica fiber is made with core and cladding materials that have very different thermal properties. Figure 5.2 shows the photograph of an illuminated end of a single-mode silica fiber donated to us by Bell Telephone Laboratories. This picture illustrates the three separate layers of the fiber, the core, the cladding; and an outer sleeve consists of silica. (2) When a silica fiber is heated to a temperature between 1325^{o}C and 1625^{o}C, the cladding is softened enough to be deformed. But the core and the sleeve remain cylindrically solid. When mechanical pressure is brute-forcely applied to change the shape of the cladding, the surface quality becomes very poor because of the inhomegenous deformation process. (3) If the borosilicate cladding is heated to its liquid state, the adhesion of the fiber to the form is much worse, and a much poorer taper is obtained. In short, the drastically different thermal properties of the cladding and the core have prevented the silica fiber from deforming uniformly in the

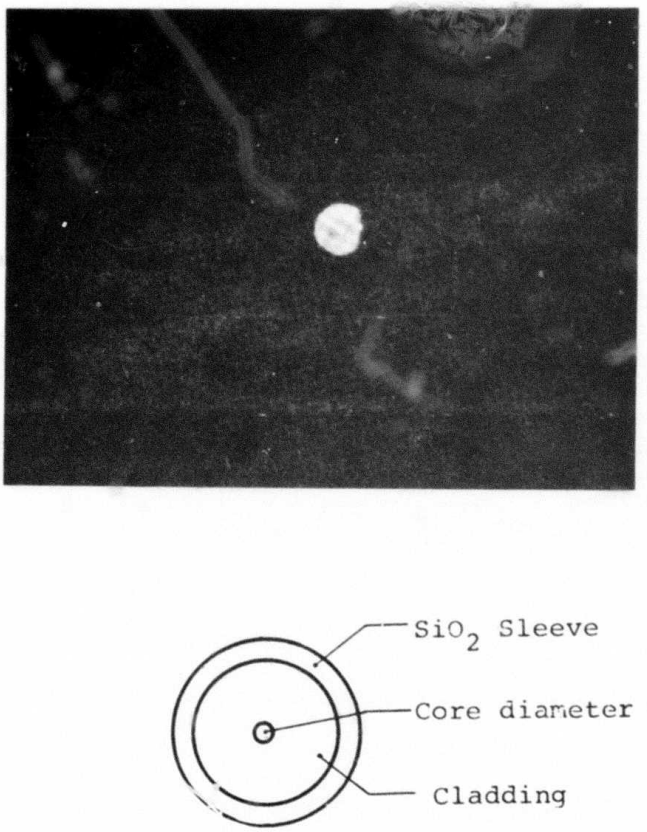

Figure 5.2 Photograph of the Single-mode Fiber Cross-section

plastic temperature range. This is a fundamental bottleneck to the fabrication of silica fiber horns by any form of heating process. Nevertheless, the ability to deform the cladding without deforming the core may be very useful. For example, it may be used to remove cladding materials from the core in the future.

5.2 Fabrication and Evaluation of Tapered Transitional Structures

We discussed in the previous section the reasons why the horn cannot be fabricated with silica fibers. Alternative methods must now be found. One alternate method for fabricating a fiber horn has already been reported by Dalgoutte, et al., in that an externally mounted glass fiber horn was fabricated by drawing it from a glass pre-form. On the other hand, there is no reason that a transition from a uniform thin-film waveguide to a channel waveguide configuration cannot be made either within the GaAs waveguide or the transitional waveguide. If there is such a transition, the fiber can then be coupled by evanescent field directly to a tapered channel waveguide when its cladding is sufficiently removed. The disadvantage of Dalgoutte's method is that the externally mounted fiber still needs to be interconnected with the single-mode fused silica fiber for transmission. The disadvantage of using a channel waveguide is that the horizontal position alignment is critical between the core and the channel. However, recent trends in integrated optics research (see, for example, the technical digest of the 1976 Topical Meeting in Integrated Oqtics) indicate that a monolithic integrated optical subsystem may

utilize channel waveguides in GaAs. In that case, since channel waveguides have already been used in GaAs, we may as well use a channel transitional waveguide for coupling into fibers.

5.2.1 Fabrication and Evaluation of Tapered Waveguide

In order to match the geometry of the planar waveguide to the geometry of the channel waveguide, we have experimented with the fabrication and evaluation of two types of tapered waveguide structures. In one case we have used conventional photolithography to create metallic patterns on top of a planar glass waveguide as shown in Figure 5.3a. In this case the complex dielectric constant of the metal film lowers the propagation wave constant β of the waveguide under the metal film, thereby producing a channeled waveguide and a tapered transitional section. As an alternative, we have also made Al mask patterns on microscope glass and then immersed the sample into the solution of $AgNO_3$ to obtain ion exchanged, high index tapered transition as shown in Figure 5.3. The aluminum mask is removed later after the ion exchange. Glass is chosen as the material for this investigation because it is planned to be the material for the TWG and because its index can be altered by the ion exchange technique. Results obtained from this investigation should be directly applicable to the fabrication of a tapered section in a transitional waveguide.

Our ion exchanged glass waveguides are prepared by immersion of sodium glass slides in the $AgNO_3$ solution at $230^{\circ}C$. Typically, we obtain a single-mode planar waveguide after 8 minutes of immersion. The attenuation rate of such a waveguide is typically 10 dB to 15 dB per cm. A three-mode planar waveguide is obtained

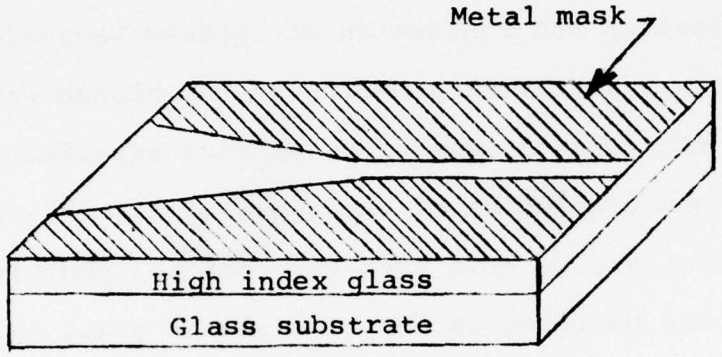

(a)

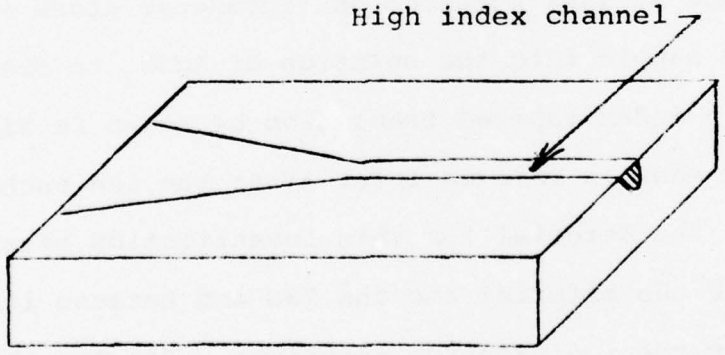

(b)

Figure 5.3 Illustration of Tapered Transitional Structures

after 15 minutes of immersion. The attenuation rate of the three-mode planar waveguide is typically 5 dB per cm. Since the single-mode waveguides are quite lossy, an immersion time of 15 minutes is used for the fabrication of all tapered transitional structures. The channeled waveguides fabricated in this manner have attenuation rates of 8 dB to 20 dB per cm for 20 μm wide channels and 12 dB to 30 dB per cm for 10 μm wide channeled waveguides. These preliminary attenuation rates can probably be lowered significantly in the future. However, no attempt was made to do this during the present reporting period. Instead, we are primarily interested here in assessing the additional attenuation that may be caused by the tapering transition.

When chromium or aluminum is deposited on top of the planar waveguide as described in the preceding paragraph to form a tapered pattern, as shown in Fig.5.3(a), good confinement of the optical beam was obtained as evident from Fig.5.4. But the channeled waveguide produced in this manner has so high an attenuation rate that the guided wave mode cannot propagate more than a few millimeters of distance.

In order to fabricate tapered transitions by ion exchange, aluminum was used as a mask on top of a sodium glass substrate. The masked sample was then immersed in a solution of $AgNO_3$. After that, the Al mask was removed. Such a tapered transition produced by ion exchange gave acceptable attenuation in the channeled waveguide, but the confinement of a planar guided wave mode to a channeled guided wave mode is not effective until the

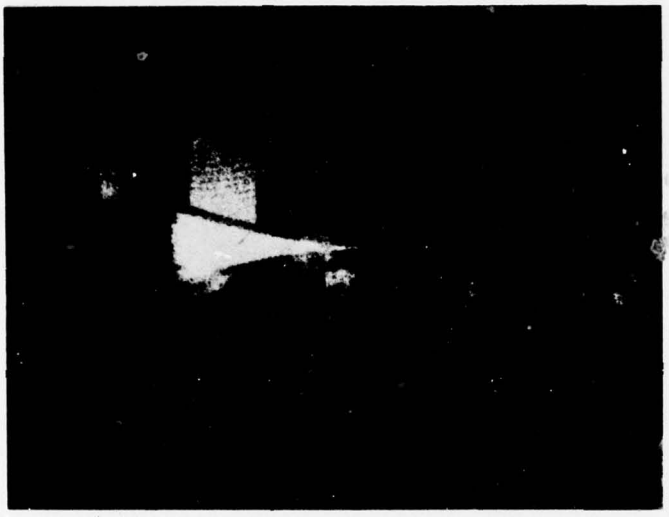

Figure 5.4 Picture of the Confinement of the Planar Guided Wave by the Metal Mask.

tapering angle is very small. We have experimented with two taper designs. Figure 5.5(a) shows the design where the channeled section is joined with a circular taper mask pattern. Figure 5.5(b) shows the design where the channeled section is joined with a linear taper. Both designs were chosen because of the convenience in cutting the mask. But the linear taper seems to be superior in performance.

To compare the confinement of the planar guided wave mode by metallization and by ion exchange and to measure the effect of the tapering angle on the coupling efficiency of the planar waveguide to the channeled waveguide, we have evaluated the net coupling loss (i.e., the net additional attenuation of the power transmitted through the entire waveguide, including the taper, above the normal attenuation of the channeled waveguide) as a function of the linear tapering slope which is defined as d/D in Fig.5.5(b). These measured results are listed as following:

Method of Confinement	Tapering Slope (d/D)	Coupling Loss in dB
Metallic (Al)	1/20	6
ion exchange	1/20	10
ion exchange	1/30	3.5

Based upon these results and the attenuation rate of the channeled waveguide, we have chosen ion exchange as the most promising method to obtain a planar to channeled transitional waveguide. However, to obtain ion exchange the guiding film must be sodium glass. We have tried, but failed, to obtain any significant ion exchange in either SiO_2 or BaO_2 glass films. Therefore, an

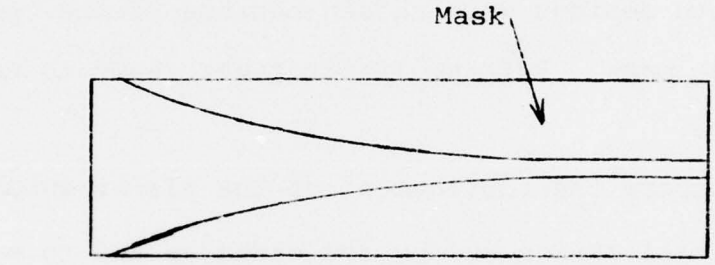

(a)

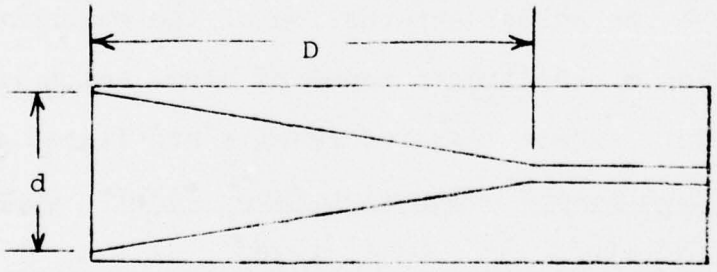

(b)

Figure 5.5 Illustration of Two Mask Patterns

experimental investigation was launched during this period to deposit sodium glass as the waveguiding layer and to evaluate its property in ion exchange, as discussed in Section 6.

In summary, we have demonstrated the ion exchange as an effective method to create a tapered transition (a) between a planar waveguide and a channel waveguide, and (b) between two channel waveguides of different horizontal cross sections. This method is compatible with the TWG described in Section 4. The demonstrated coupling loss is only 3.5 dB. However, more than 90% efficiency has been demonstrated in the tapered structures in in-diffused $LiNbO_3$ waveguides (50). There is no reason that the efficiency of the ion exchanged waveguide cannot approach that value when the design of the taper is optimized. The most cruical factor yet to be examined is the fabrication and the evaluation of sodium glass waveguide that can be used with ion exchange to form either the tapered or the channeled TWG.

5.3 Fabrication and Evaluation of Low-Loss Sodium-Glass Films Suitable for Ion Exchange*

Despite the fact that ion exchange has been used extensively in bulk sodium-glass to obtain optical waveguides, thin films of these glasses have not be reported to date. We have, therefore, developed techniques for fabricating sodium glass films by sputter deposition and re-glassification as follows.

*Work supported jointly by Navy Contract No. N00014-76-C-0796

Fabrication of sodium glass thin films on silica substrates involves two steps: first, sputter deposition of a sodium glass film from a Na_2O/SiO_2 (17% Na_2O) target. Films thus formed exhibit a strong amber color indicating excess of sodium present in the film. These films have extremely high loss and are not suitable for waveguide applications. The second step is the glassification of these films. This involves heating the wafer to a temperature which corresponds to the glass formation. This temperature is about 800°C, as can be seen from the phase diagram in Figure 5.6 (51). Baking time between 5 to 15 minutes is adequate to form very clear films. It is necessary to avoid any prolonged heating of the film at lower temperatures which results in formation of defects as shown in Figure 5.7. This is believed to be caused by devitrification or phase separation which can take place at temperatures around 700°C.

Films formed with thin layers of sodium glass (glassified at 800°C for 5 minutes and rapidly cooled) have shown excellent waveguiding properties, in particular, the measured attenuation rate is less than 1 dB/cm. These films form single-mode waveguides at the 6328 Å wavelength. When thicker films of sputtered sodium glass are glassified the waveguides thus formed show multiple tracks of the guided wave beam. A close surface examination has shown that cracks developed on the surface. A typical branching cracked pattern with the origin of the fracture is shown in

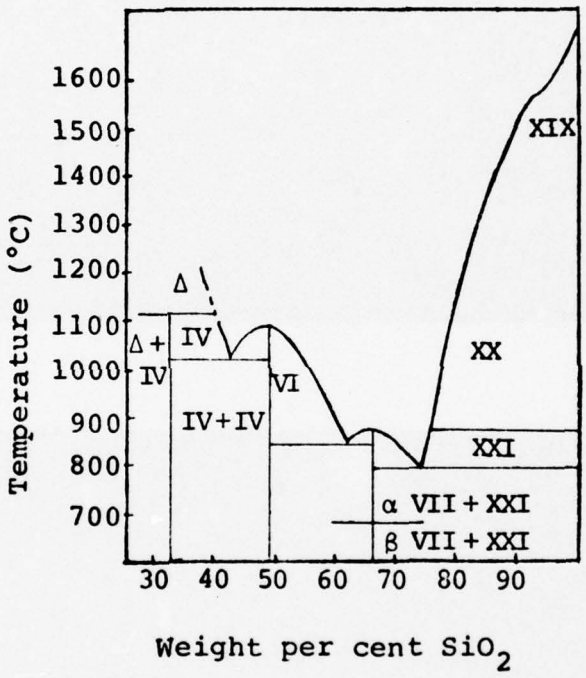

Figure 5.6 Melting point curves for the binary system sodium oxide silicon dioxide. Δ, sodium oxide field; IV, sodium orthosilicate field; VI, sodium metasilicate field; VII, sodium disilicate field; XIX, cristobalite (SiO_2) field; XX, tridymite (SiO_2) field; XXI, quartz (SiO_2) field; XXI, quartz (SiO_2) field

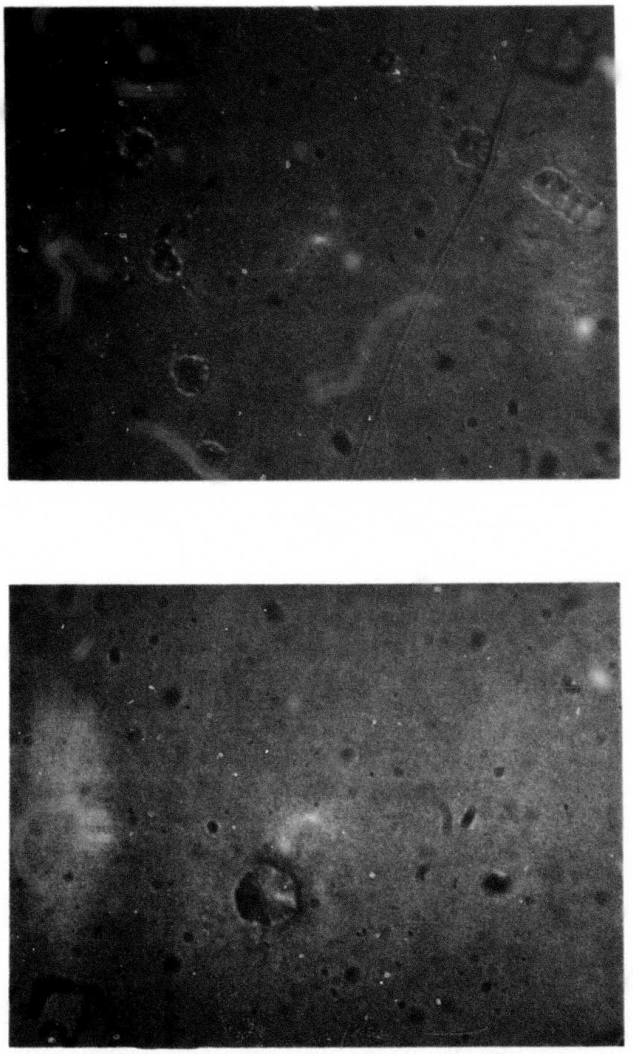

Figure 5.7 Micrographs of Defects Caused by Devitrification

(magnification: 780)

Figure 5.8. We believe the fractures are caused by stress developed in the surface film on cooling. These cracks may be precipitated by pre-existing surface fractures, and hence their origin may be similar to that of Griffith cracks. Since the density of these fractures varied from sample to sample, we believe that by using better surface quality silica wafers such fractures may be reduced considerably.

From our experiments with different glassificiation times with the same initial thickness of sputtered glass films, we have concluded that the sodium-glass formation involves both the melting of the sodium-glass and diffusion at the silica-sodium-glass interface. This is exhibited by reduction in effective refractive index, β/k, of the waveguide as the glassification time in increased. When the baking process is repeated for the already glassified wafers, a reduction in β/k is again observed. Table 5.1 summarizes the variations of β/k and the number of modes observed in films made under different conditions.

Finally, these sodium-glass films were ion exchanged for Ag in molten $AgNO_3$ at $260^{\circ}C$ for 15 minutes. Large index changes $\Delta n \simeq 0.1$ have been observed. This is manifested by an increase in β/k and by the number of modes the waveguide can support.

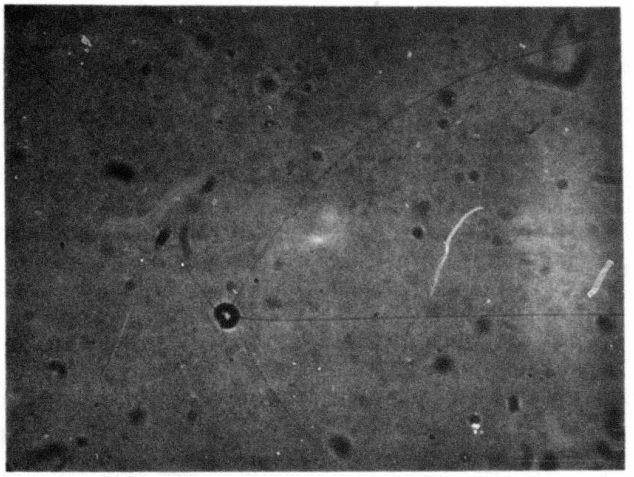

Figure 5.8 Micrograph of Surface Fractures

Table 5.1. Characteristics of Na-Glass Waveguides

Initial Film Thickness (μ)	Glassification Time (minutes)	Number of Modes	β/k	β/k after Ion Exchange
0.25	5	1	1.47	1.55
0.6	5	1	1.485	1.588 for m = 0
0.6	15	1	1.489	1.52 for m = 1
0.6	36	1	1.493	
1.5	5	2	1.493 1.466	(high attenuation)
1.5	20	2	1.486 1.464	

6. HOLLOW DIELECTRIC TRANSITIONAL WAVEGUIDE

In Section 4 we used sputtered SiO_2 for the buffer layer of the TWG because its sputtering properties have been throughly characterized. This will, however, give a β-value of the modes of the TWG higher than that of the fiber. In order to meet the requirements of the β values for phase matching we have already discussed, in Section 2, the possibility of MgF_2 as the buffer layer and also the possibility of modifying the index of the fiber core by formation of a layer of sodium glass on it. Another way to achieve a β lower than that of the fiber is to utilize the hollow dielectric modes of SiO_2/GaAs or $SiO_2/LiNbO_3$.

A hollow dielectric waveguide, as opposed to a conventional waveguide, is one in which one or both the media surrounding the guiding film have a refractive index higher than that of the guiding film. The energy is guided as a result of large reflection coefficient, i.e., the reflection coefficient close to 1, at these interfaces. Hollow dielectric waveguides of circular cylindrical geometry have been investigated earlier by Kapany et al., (52) and used in waveguide gas lasers (53). In this section we will describe the investigations carried out to determine the usefulness of a hollow dielectric transitional waveguide (HDTWG) as a transition waveguide.

The two major foci of our investigations are: (i) The variation of β as a function of the thickness of the guiding film. This variation will determine whether the tapering of the film thickness will bring about a significant change in β so as to result in a reasonable coupling length for tapered velocity coupling between the HDTWG and the optical fiber. (ii) The attenuation loss in the waveguide.

Consider a hollow dielectric waveguide consisting of a thin film of low refractive index n_b on top of a substrate of high refindex, n_s, as shown in Figure 6.1. A true modal solution of such a waveguide does not exist. However, from geometrical optics point of view a hollow dielectric mode may be represented as a plane wave bouncing between the air-film and film-substrate boundaries such that the total phase shift in one round trip of the plane wave is a multiple of 2π. The wave suffers a total internal reflection at the film-air boundary, thus there is no energy loss to the air region. However, at the film-substrate interface there are both the specular reflection and the transmission. The transmitted beam constitutes the leakage of power from the waveguide. If the reflection coefficient at film-substrate interface is close to 1, the guided wave will propagate without appreciable loss in energy.

The propagation wave number β_h of such a waveguide can be obtained in a fashion similar to that of the conventional

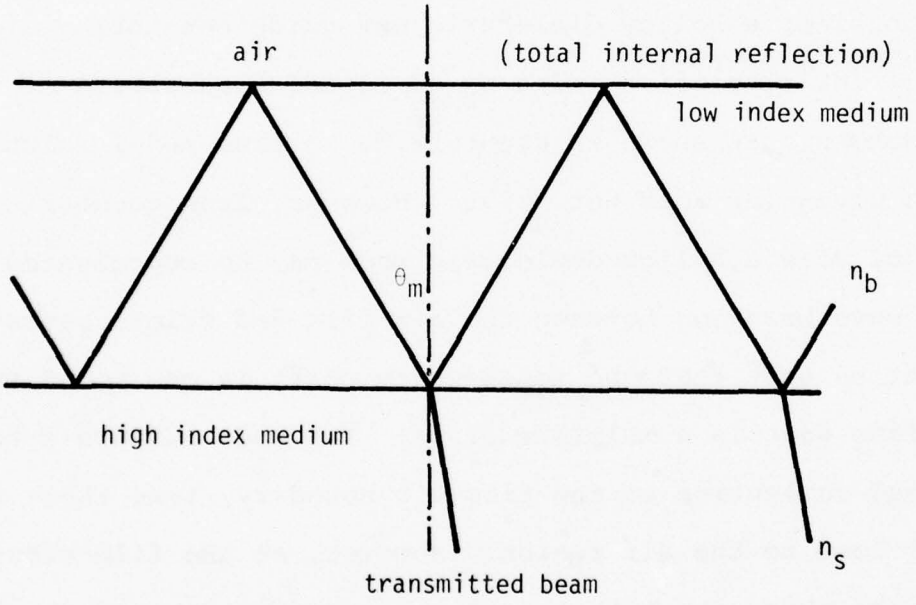

Figure **6.1** Plane Wave Representation of the Hollow Dielectric Waveguide

waveguide by requiring the round trip phase shift of the modal ray to be multiples of 2π. The equation obtained in this manner for β_h is

$$n_b kt \cos\theta_m - \tan^{-1} \frac{\sin^2\theta_m - 1/n_b}{\cos\theta_m} = (2m + 1)\ /2 \qquad (6.1)$$

where θ_m is the angle of incidence of the plane wave representation of the mth propagating hollow dielectric waveguide mode shown in Figure 6.1 (i.e., $\beta_{hm} = n_b k \sin\theta_m$); t is the thickness of the film; $k = 2\pi/\lambda$. It is clear from this equation that β_{hm} will change as the film thickness is varied. Figure 6.2 illustrates such changes in β_{ho}/k for a hollow dielectric waveguide mode in SiO_2 on top of GaAs. These changes demonstrate that phase matching can be achieved easily between the fiber and the waveguide by a tapered section. We have also experimentally fabricated hollow dielectric waveguides with SiO_2 layer (about 6 μm) and AZ 1350 layer (about 3 μm) on flat GaAs samples. We were able to excite these modes by prism coupler just like the usual waveguides modes. The measured values of β_{hm} also correspond well with the calculated results.

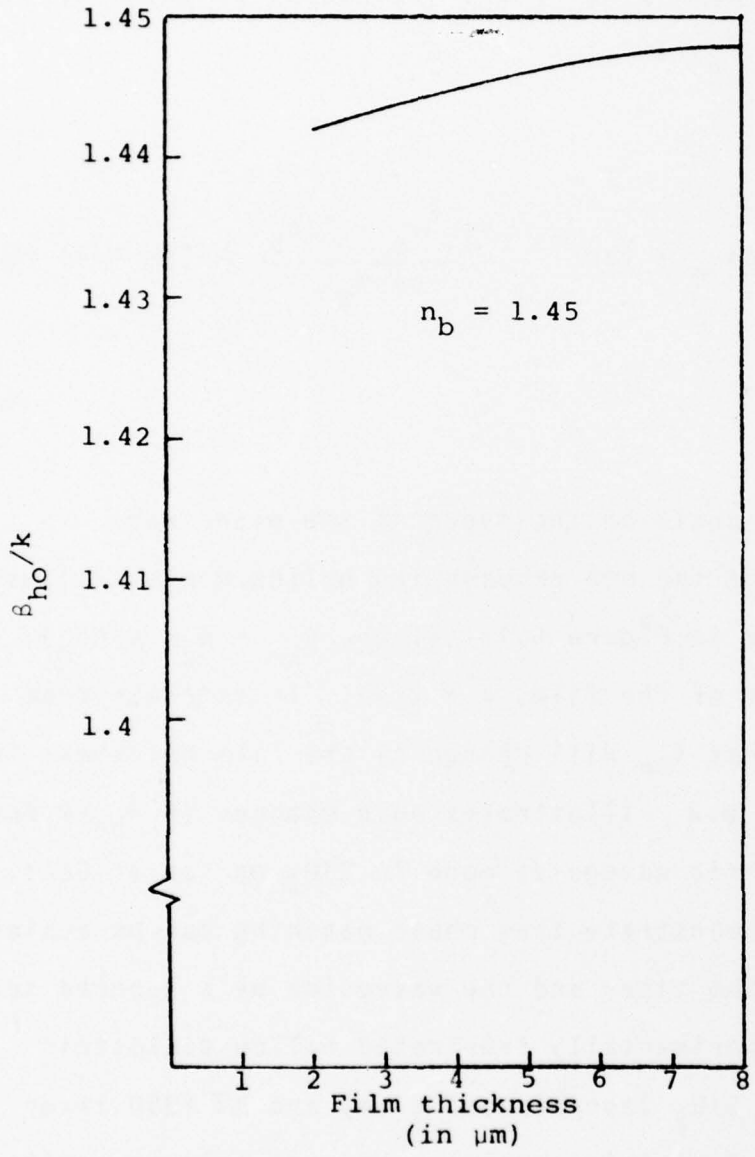

Fig. 6.2 Variations of the Propagation Wave Number of the Hollow Dielectric Waveguide Mode as a Function of Waveguide Thickness

The loss in the hollow dielectric waveguide can be calculated in a manner similar to the mode sinking loss determined in Section 3. Substituting $t_B = 0$ in Equation 3.16 yields the loss

$$\alpha = \frac{1 - \rho_{FS}^2}{2\tan \theta_m} \tag{6.2}$$

where

$$\rho_{FS} = \frac{n_b \cos \theta_m - n_s \cos \theta_s}{n_b \cos \theta_m + n_s \cos \theta_s} \tag{6.3}$$

and

$$\theta_s = \sin^{-1}[n_b/n_s \sin \theta_b] \tag{6.4}$$

Figure 6.3a shows the loss (in nepars/m) for various modes of SiO_2/GaAs at 1.06 μm wavelengths. Similar plots for AZ1350/GaAs are shown in Figure 6.3b. From this we see that the attenuation rate of the HDTWG is high (>3dB/cm) unless the film thickness is about 10 μm. At large film thickness very low losses (<1dB/cm) are possible. These high losses are

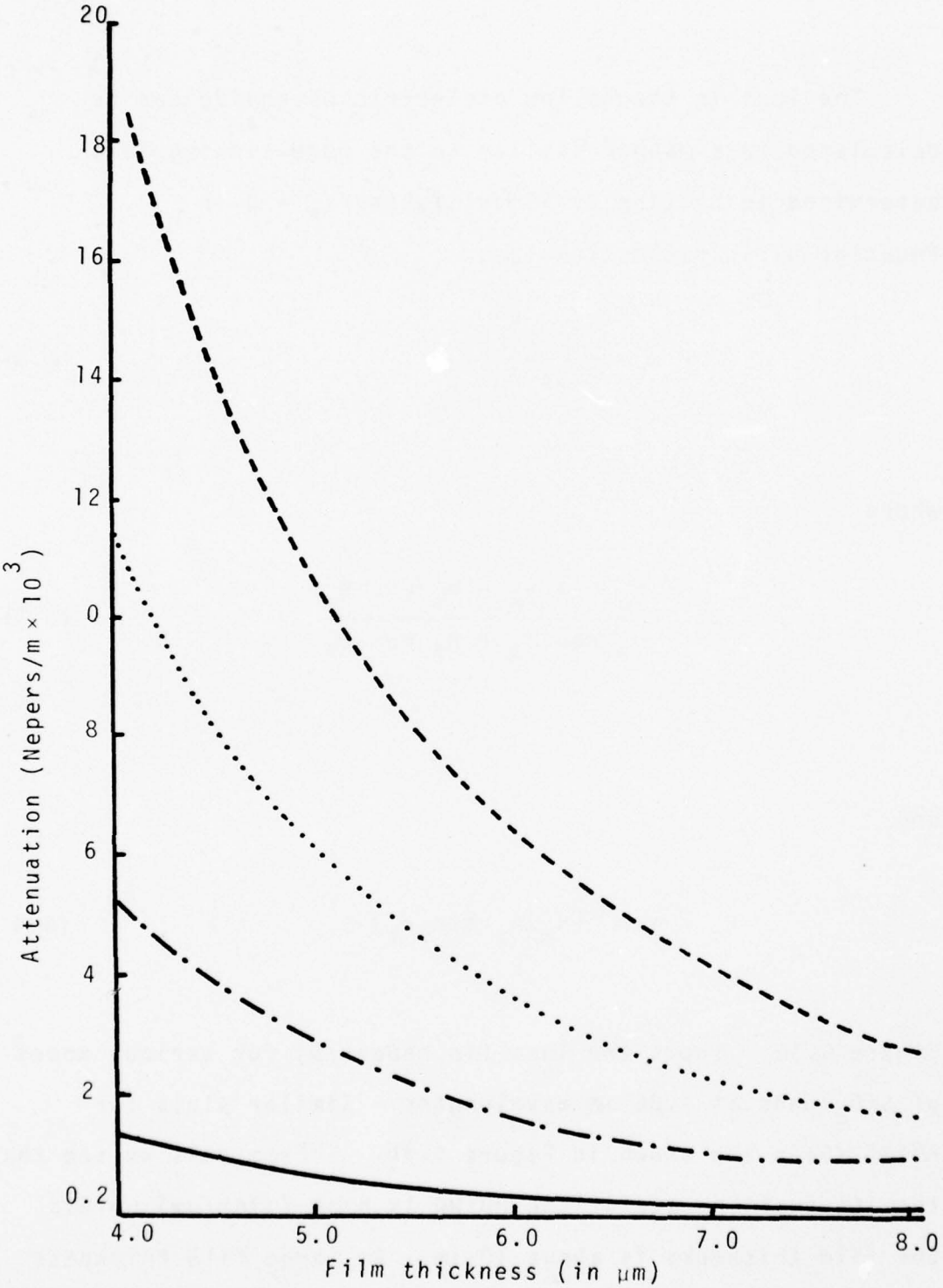

Figure 6.3a Attenuation Loss in an SiO_2/GaAs Hollow Dielectric Waveguide as a function of film thickness, λ=1.06.

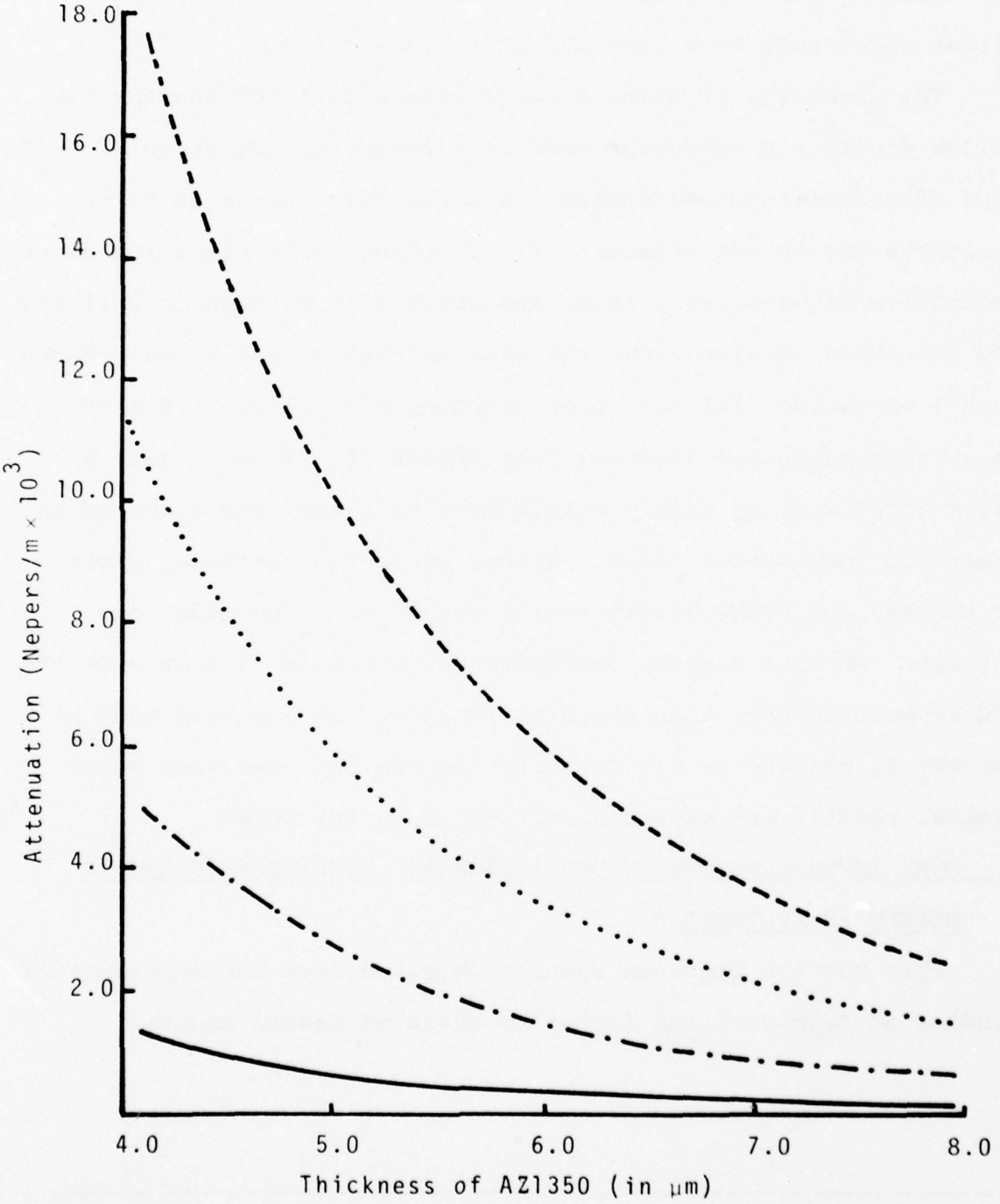

Figure 6.3b Attenuation Lo in an AZ1350/GaAs Hollow Dielectric Waveguide as a function of film thickness; λ=1.06.

confirmed by our experiments by noticing that the guided wave streak fades away in a very short distance (<1 cm).

The necessity of using a large waveguide thickness for the hollow dielectric waveguide mode is a severe disadvantage of this type of transitional waveguide. A large film thickness is undesirable due to two reasons: (i) Coupling coefficient for direct excitation between the primary and HDTWG will be high only if the PWG thickness is also about the same as that of the HDTWG. Hence, such a waveguide will have poor coupling efficiency if the PWG is a GaAsP waveguide (typical film thickness ~ 2 μm). (ii) A thick HDTWG will be highly multimode with a very small spread in β between the various modes. Hence, small fabricational error at the PWG and HDTWG junction will result in large mode conversion. We have already demonstrated in Section 4 that when the TWG is much thicker than the PWG, the power in a single mode of the PWG is coupled to all the modes of the TWG, and vice versa. Similar results are expected to take place for HDTWG.

7 SOME INVESTIGATIONS ON DEPOSITION AND ETCHING PROFILES IN MASKED RF SPUTTERING*

This section presents results obtained from the experimental studies of film profiles formed by means of masked sputter

*Work supported jointly by Navy Contract N00014-76-C-0796

deposition. The actual profiles are compared with the theoretical profiles expected from the cosine distribution of the sputtered material. In addition, a discussion of masked sputter etching is given. In particular, the effects of the mask characteristics and the back scattering on the etch profiles are discussed.

7.1 Deposition Profile Using a Mask

In a simple plane parallel diode sputtering system using an amorphous or poly-crystalline target, the random nature of the collision processes at the target leads to an ejection pattern which is basically cosine, i.e., the fractional mass $dm_e(\phi)$ ejected in a solid angle $d\omega$ at an angle ϕ from an elemental area is given by $dm_e(\phi) = m_e \cdot \cos\phi \cdot d\omega/4\pi$ where m_e is the mass of the ejected material. This basic distribution is modified by the energy and the direction of the bombarding ions. At low energies the profile tends to be an under-cosine and at high energies an over-cosine. Under oblique ion incidence, the target atoms are sputtered along a direction parallel to that of the specular reflection of the incoming ion beam.

Assuming that the ions are normally incident at a circular disc type target and using the cosine distribution of the ejected material, we obtained the deposition rate at any point P on the substrate (see Figure 7.1) to be (54)

$$d = 1 - \frac{1 + (\ell/D) - (s/D)}{\left\{\left[1 - (\ell/D)^2 + (s/D)^2\right]^2 + 4(\ell/D)^2\right\}^{\frac{1}{2}}} \qquad (7.1)$$

where ℓ is the distance of the point P from the center, D is the interelectrode spacing and s is the diameter of the target. The validity of the cosine distribution can be seen by comparing the actual distribution of the deposited material at the substrate with that given by Equation 7.1. Figure 7.1 shows a plot of Equation 7.1 (solid lines) and the measured profiles (broken lines) of the deposition at the substrate of an rf dicde sputtering system with 8 cm interelectrode spacing. The depositions were made from a five inch diameter SiO_2-target, at 15 m torr Argon pressure and 500 watts rf power with the substrate electrically floating. The two broken lines correspond to the thickness profiles at the substrate in two perpendicular directions. A good agreement between the theorectical and the experimental profiles is clearly seen. The difference in thickness profiles in

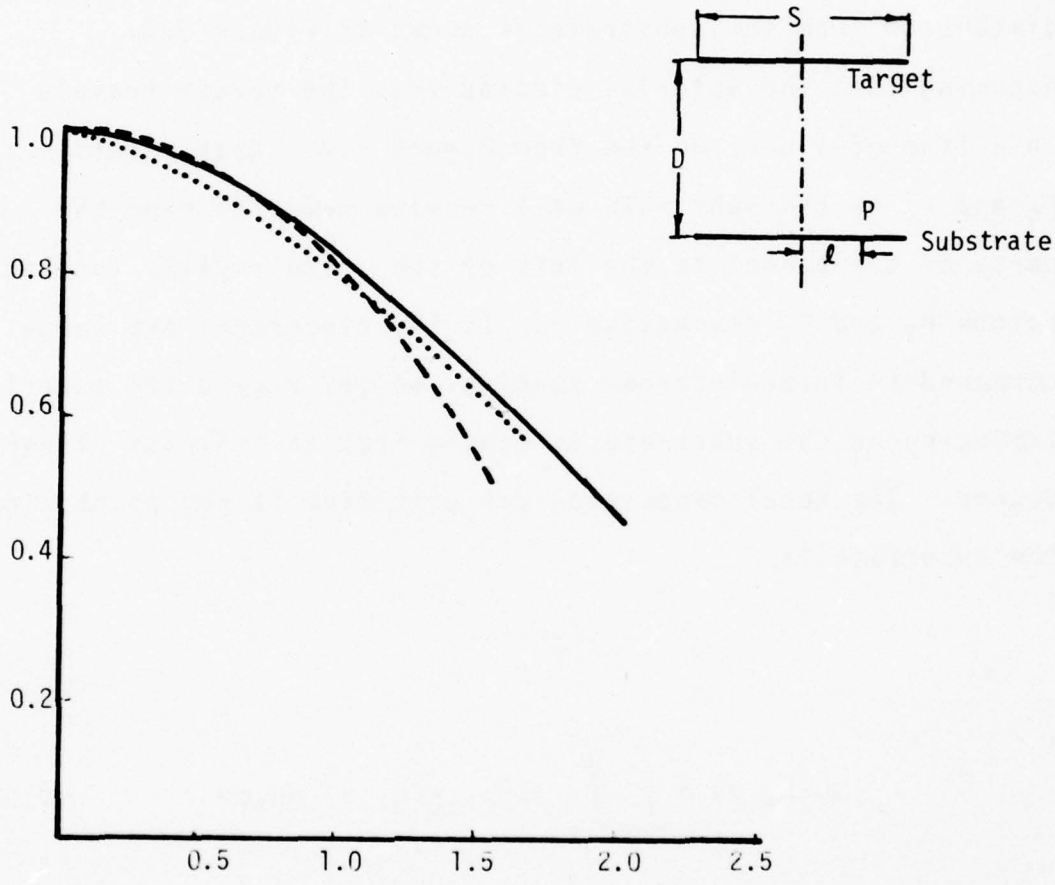

Figure 7.1 Deposition Profiles at the Substrate of a Plane Parallel rf Diode Sputtering System with Five Inch Diameter Target.

———— = Theoretical

---------- = Experimental

the two directions is caused by the asymmetry in the plasma due to the proximity of fixtures and the bell jar wall.

In order to calculate the deposition profile in presence of a mask, consider a sharp edge located at a distance h from the substrate as shown in Figure 7.2. Assuming that the material ejected from the target travels in a line-of-sight, we see from Figure 7.2. that points P_S and P_S' on the substrate will receive material from the parts of the target to the left of the geometrically located points P_T and P_T' respectively. If the electrodes are large compared to interelectrode spacing, we may regard the material impinging on the substrate as coming from an infinite planar source. The total deposition per unit time at any point x on the substrate is

$$\mu = -x\left(\frac{D-h}{h}\right)$$

$$\phi(x, y) = \int_{-\infty}^{\mu}\int_{-\infty}^{\infty} f(x, y/u, v)\, du\, dv \qquad (7.2)$$

where f(x, y/u, v) is the distribution of the material at the x, y position on the substrate from an element du dv at u, v without the mask and μ is the point which has a line-of-sight to the point x.

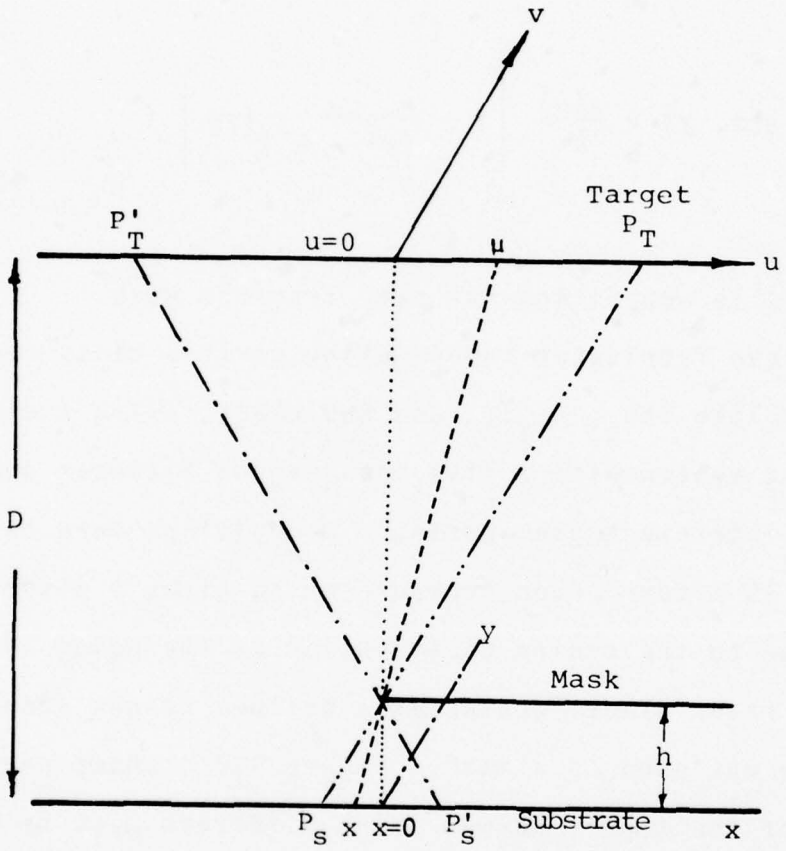

Figure 7.2 Schematic Diagram of Masked Deposition in Diode Sputtering System

If we assume a cosine distribution for f(x, y/u, v) and a unity-sticking coefficient for the sputtered material, the above equation easily reduces to

$$\phi(x, y) = \frac{\phi(\infty)}{2} \left[1 - \frac{x}{(x^2 + h^2)^{1/2}} \right] \qquad (7.3)$$

where $\phi(\infty)$ is deposition far away from the mask.

We have fabricated tapers using various glass target materials like SiO_2, As_2S_3, and BaO glass, using a diode rf sputtering system with a five inch target diameter and an eight cm interelectrode spacing. Depositions were carried out at a 15 m torr Argon pressure which gives a distribution very close to the cosine distribution at the power levels used. A razor blade located at a desired height above the substrate was used as a mask. Figure 7.3 shows profiles of some of the tapers formed using different mask heights. These profiles were measured by Dektak using a 25 μm stylus. Figure 7.4 shows theoretical and experimental profiles for a mask height of 160 μm. From these figures we notice a close agreement of simple theoretical and experimental profiles for regions that are not directly located under the mask, i.e., $x > 0$, in Figure 7.2. Directly under the mask

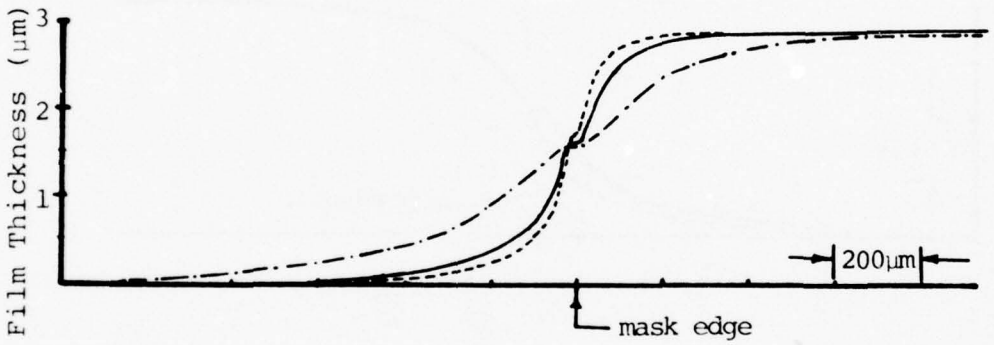

Figure 7.3 Deposition Profiles for Different Mask Heights

Mask height: ------ 75 μm
——— 100 μm
—·—· 220 μm

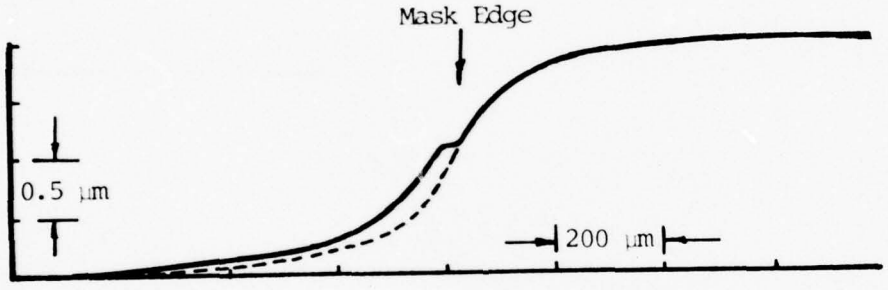

Figure 7.4 Experimental and theoretical profiles formed by a mask height of 160 µm

-------- Theoretical
———— Experimental

edge there is a discontinuity in slope. This discontinuity causes a shift between experimental and theoretical curves for the substrate region directly under the mask, i.e., $x > 0$ in Figure 7.2. When the mask thickness is increased, the region over which the discontinuity extends also increases, implying that the discontinuity is caused by a finite thickness of the mask. This can be seen from Figure 7.5 where a mask of thickness t is located at height h above the substrate. For region $x > 0$, the effective mask height is $(h + t)$ whereas for region $x < 0$ the effective mask height is h. Tapers thus formed have shown excellent optical quality. This is clearly seen by the smoothness of interference fringes seen under an optical microscope as shown in Figure 7.6. The discontinuity in slope near $x = 0$ is indicated by a spread out fringe as identified by the arrow. Standley et al. (55) have shown that some of the mask material is embedded in the film close to the mask edge. However, since our mask is very thin the amount embedded would not significantly change the optical characters of the tapers. No deleterious effects have been observed when such tapers were used in thin film waveguide applications.

When a cleaved piece of GaAs, 330 μm thick, placed directly on the substrate was used as a mask the deposited film thickness profile thus formed is shown in Figure 7.7. A common feature of Figure 7.3 and Figure 7.7. is that at

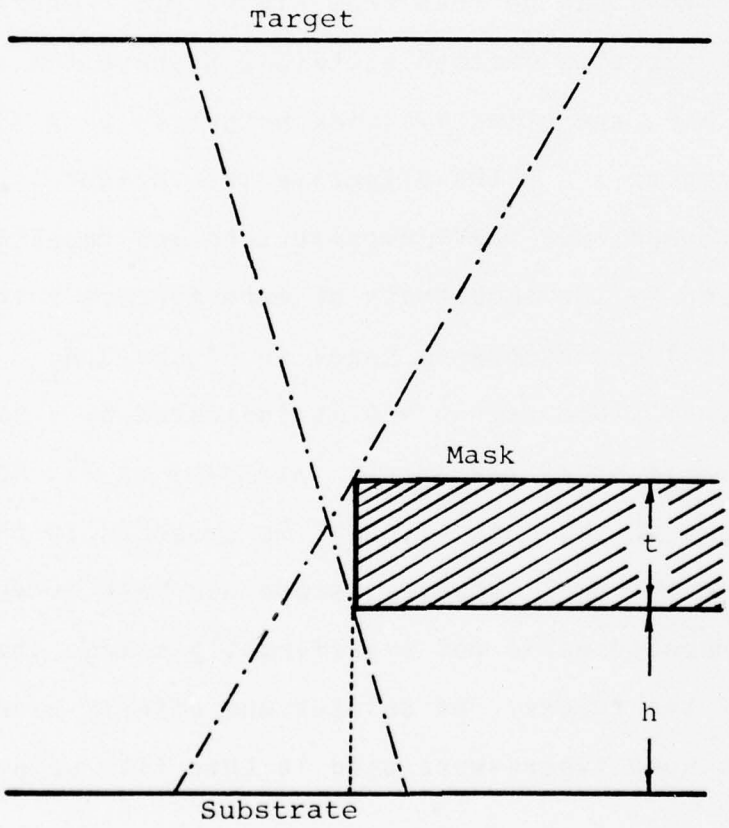

Figure 7.5 Illustration of different effective mask heights for regions directly under the mask and regions away from it

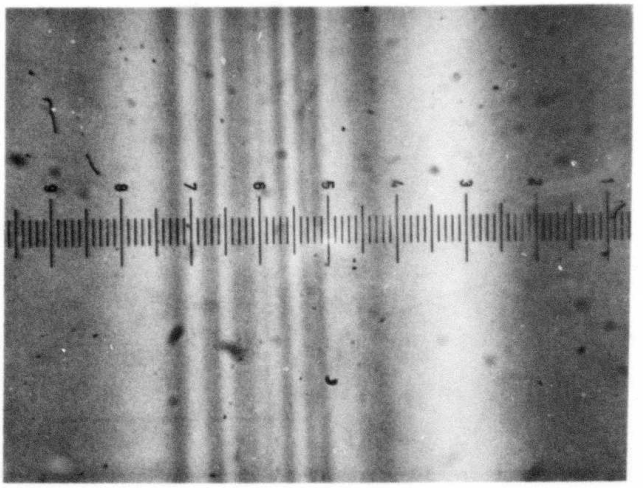

Discontinuity in Slope

Thickness increasing

Figure 7.6. Interference fringes due to a taper formed by a mask located 380 μm above the substrate. Each small division equals 174 μm.

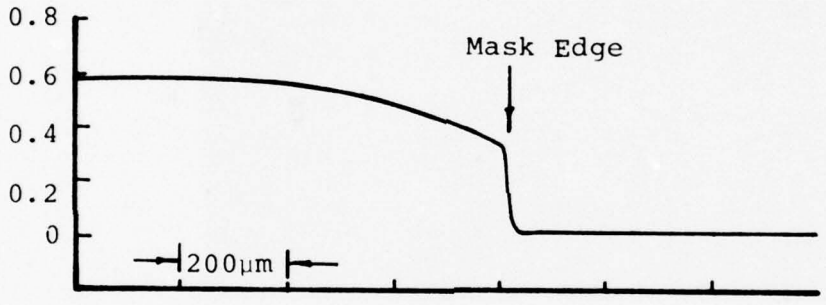

Figure 7.7 Profile of film thickness deposited with a 330 μm thick mask placed directly on the substrate

the mask edge the film thickness is larger than the theoretical value of $\phi(\infty)/2$. Moreover, deviation from the theoretical value was found to be larger with thicker masks. There are three possible explanations for this phenomenon:

1. The re-emission of the deposited material, expected to take place predominantly in the region $x<0$, will effectively reduce the deposition rate in this region. We have measured the thickness of the film deposited on the underside of the mask i.e. facing the substrate during the deposition. From this we estimated the re-emission coefficient to be less than 0.1. This is in agreement with the data reported earlier (56). In view of the re-emission, the film thickness at the mask edge should be $0.55\ \phi(\infty)$.
2. The non-uniformity in the ejection of the material from the various portions of the target may contribute to the larger film thickness at $x = 0$. In particular, the rim of the target is known to behave as a more intense source of the sputtered material than the rest of the target (55).
3. The thick mask wall acts as an additional source for depositing material onto the surface near the mask.

When a thick mask is used during the deposition, the vertical wall of the mask also receives the material ejected from the target. The deposition on the mask wall was found to

be very uniform. The uniformity of the deposition on the vertical wall is clearly seen from the interferrograms shown in Figure 7.8a and Figure 7.8b. In order to show the reference fringe pattern, the deposited SiO_2 was etched away from a part of the wall. The thickness of the deposition was measured and found to be equal to the thickness of the film on the substrate at the mask edge.

7.2 Sputter Etch Profiles Using a Mask

In sputtering the etch profiles are highly influenced by the characteristics of the mask and the sputtering parameters. In the following paragraphs we will describe how the various factors, such as the relative etch rates of the mask and the substrate, the slope of the mask wall, the mask thickness and the back scattering, affect the profile etched in the substrate.

Consider that a substrate to be sputter etched has a mask of thickness t_m over a part of its surface, see Figure 7.9. Since all the masks formed by photo or electron lithography have a finite edge slope, we will assume that the mask wall makes an angle θ_m with the substrate surface. Further, let α_m and α_s be the etching rates of the mask and the substrate respectively. If we assume that during sputtering the wall and the flat top of the mask have same etching rate, then from Figure 7.9 we see that before the entire thickness of the mask has been etched off, the angle θ_s subtended by the step in the substrate is given by

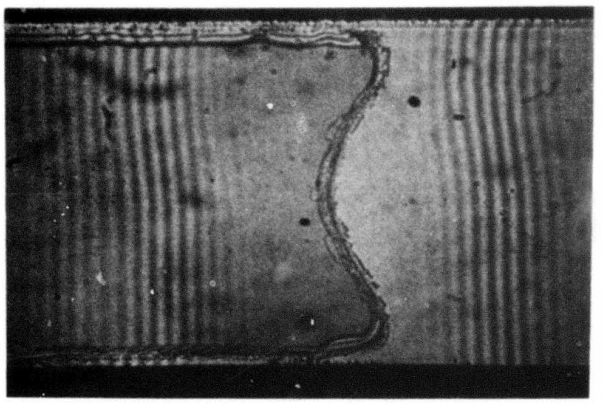

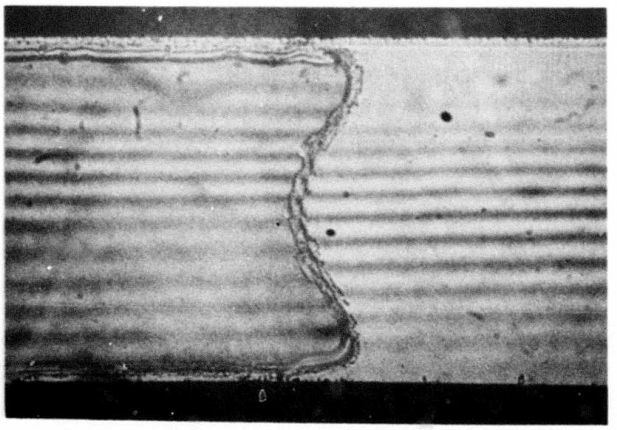

Figure 7.8 Pictures Showing Uniformity of SiO_2 Deposition on the Vertical Wall of the Mask

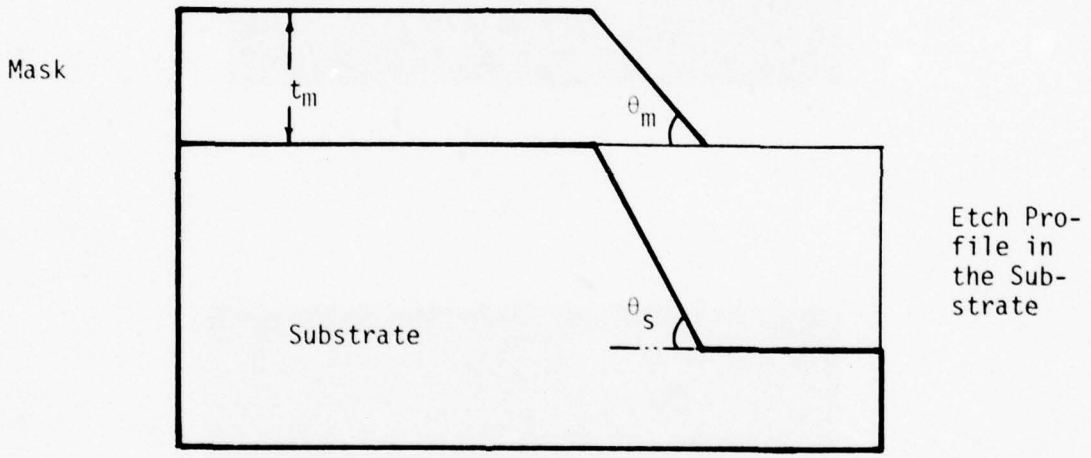

$$\frac{\tan\theta_m}{\tan\theta_s} = \frac{\alpha_m}{\alpha_s}$$

Figure 7.9 Etch Profile Formed in the Substrate due to an inclined mask wall (assuming uniform etch rate)

$$\tan \theta_m / \tan \theta_s = \alpha_m / \alpha_s \qquad (7.4)$$

This equation implies that in order to improve the angle of the etch in the substrate the etching rate of the mask should be less than etching rate of the substrate.

For most materials the etching rate of the flat top and the inclined wall of the mask are not the same. This is due to the fact that the sputtering yield (defined as the number of atoms ejected per incident bombarding ion) is a strong function of the angle of incidence of the bombarding ions. Figure 7.10 shows the dependence of the sputtering yield of some common masking materials on the angle of the incident ions (57). From the Figure 7.10 it is seen that the sputtering yield is higher for the oblique incidence of the ions and is maximum at some angle θ_{max}. Consequently, the inclined mask wall will experience a higher etching rate than the flat top. A similar effect will take place at the substrate. As the etching proceeds the wall of the groove etched into the substrate will experience a higher etching rate than the flat region. As a result a concave region is formed in the substrate near the mask edge. Formation of such a concave region is shown schematically in Figure 7.11 Figures 7.12a and 7.12b show the cross section of GaAs wafers sputter etched using SiO_2 and AZ1350 masks respectively. A concave region near the step is clearly visible.

Even when the mask edge is perfectly vertical, the sharp edges form the high field points and consequently

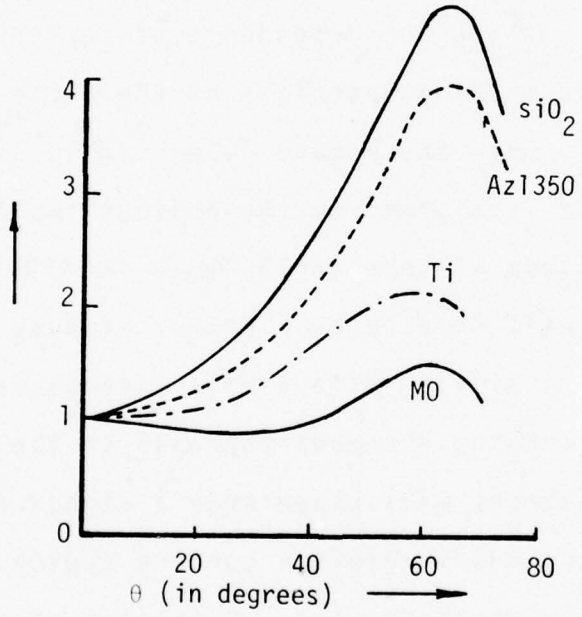

Figure 7.10 $s(\theta)/s(0)$ Versus θ for Various Mask Materials.

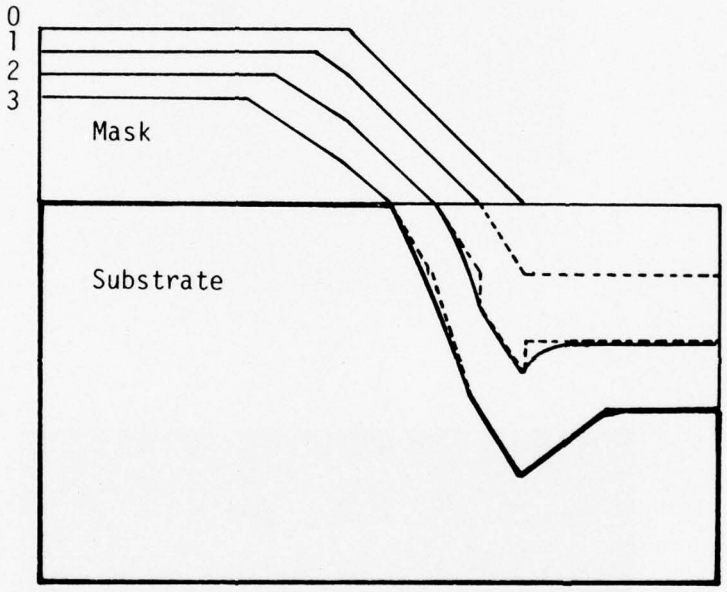

Figure 7.11 Profiles Etched into the Substrate (as the Etching Proceeds) as a result of Higher Sputtering Yield at Oblique Incidence of Ion.

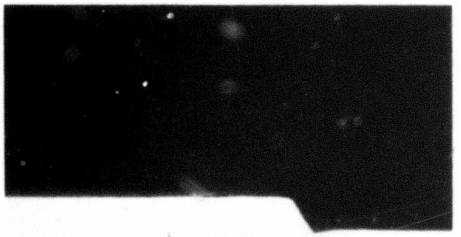

(a)

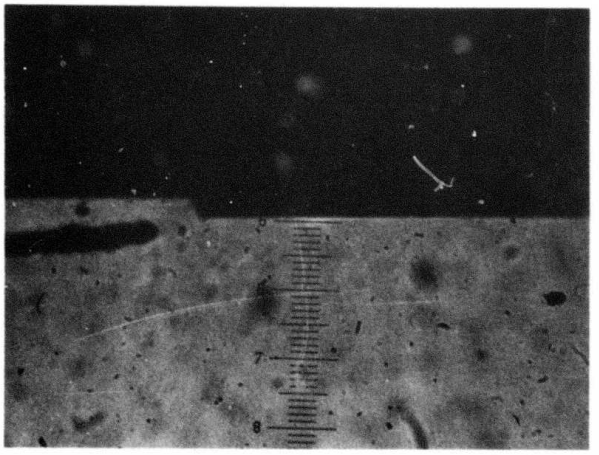

(b)

Figure 7.12 (a) Cross section of a GaAs wafer sputter etched with 6 μm thick SiO_2 mask; etched depth = 8.7 μm.

(b) Cross section of a GaAs wafer sputter etched with 1.9 μm thick AZ1350 mask; etched depth = 5.1 μm.

receive stronger ion bombardment than the rest of the mask (and the substrate). As a result, the mask begins to get distorted at the edges and flatten out till the edge slope becomes equal to the angle of maximum yield. If the etching is terminated before the inclined section of the mask wall meets the substrate, a nearly vertical step etch in the substrate can be formed. If, on the other hand, the etching is continued past this point, a concave region in the substrate will be formed as described earlier.

Another process which limits the resolution in sputter etching is back scattering. Back scattering is the reflection of ejected material consisting of neutrals, secondary ions and electrons, back to the target due to collisions with the sputtering gas atoms and the electrostatic attraction. In a normal etching process, the wafer to be etched covers only a small area of the electrode; hence the material back scattered onto the wafer is predominantly from the electrode which is simultaneously being etched away. During the sputtering run, the back scattered material is being continually deposited and etched away from the wafer. In absence of the mask, the back scattered material is almost uniformly deposited over the whole target. With the presence of mask, the back scattered material will be deposited on the wafer with a profile similar to that described in the earlier section, i.e., Equation 7.3. Thus, less material is

deposited near the step mask than away from it. Hence, the net etching rate α_n of the substrate may then be written as

$$\alpha_n = \alpha - K \left[1 - \frac{x}{(x^2 + h^2)^{1/2}} \right] \qquad (7.5)$$

where K is a constant depending on the scattering processes involved and the etching rate of the redeposited material (which may not be the same as that of the electrode material); α is the etching rate of the substrate with no back scattering, and x is the distance measured from the mask edge. From Equation 7.5 we see that back scattering will cause a reduction in the etching rate of the substrate and also result in an apparently enhanced etching rate near the edge of the mask (i.e., an "undershoot).

In order to observe the effects of back scattering independent of the other effects due to the mask (as described earlier) we used well cleaved thin pieces of optically polished GaAs (5-13 mil thick) as the masks. These masks were placed in intimate contact with the optically polished wafers to be etched. In addition to having vertical edges such a mask also offers the advantage of being able to separate easily from the substrate after etching. The etch profiles thus obtained in GaAs and $LiNbO_3$ substrate are shown in Figure 7.13a and Figure 7.13b respectively. These wafers were

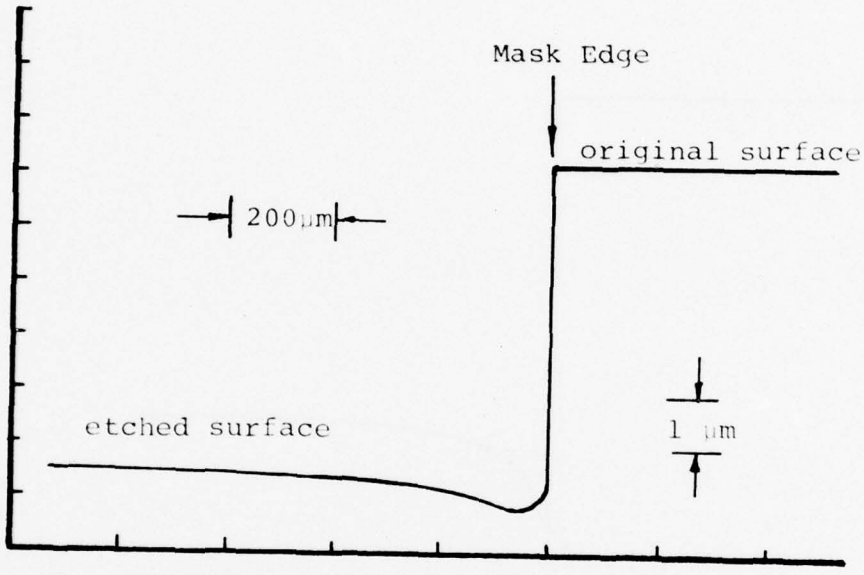

Figure 7.13a Profile produced in $GaAsP_{1-x}P_x$ waveguide by sputter etching using a cleaved piece of GaAs as a mask

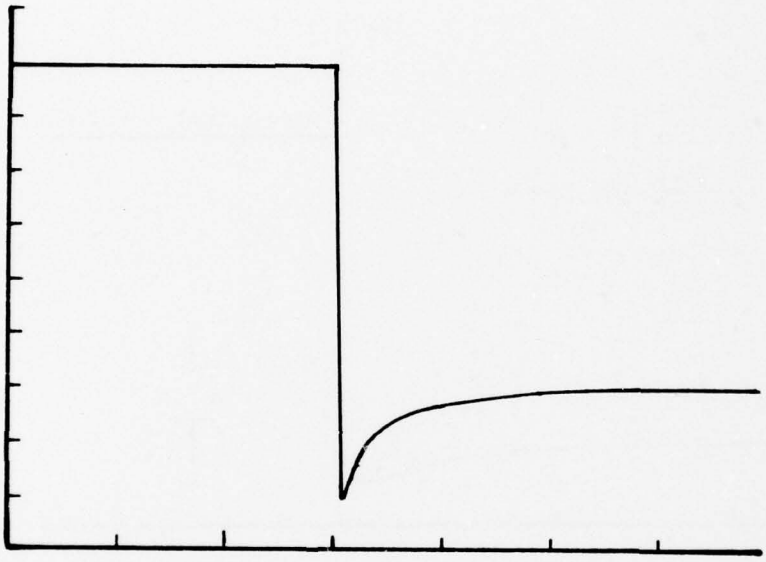

Figure 7.13b Profiles produced in $LiNbO_3$ by sputter etching using a cleaved piece of GaAs as a mask

Horizontal Div. = 200 μm
Vertical Div. = 0.5 μm

etched using 330 μm masks at 15 m torr of Argon pressure and profiles were monitored by Dektak using a 25μm stylus. The etch profiles clearly show an undershoot at the mask edge. A similarity between the deposition profile (Figure 7.7 and the etch profile can also be seen. When Equation 7.5 is used to calculate the etch profile, we found good agreement between the calculated and the measured profiles provided that the coefficient 1 is replaced by 1.3. This correction is reasonable in view of the results shown in Figures 7.3 and 7.7 which indicated a deposited thickness larger than $\phi(\infty)/2$ at the mask edge.

From Figure 7.13 and the data in Tables 7.1 and 7.2 (to be discussed later) we find that when $LiNbO_3$, fused silica, GaAs and Si substrates are etched under the same sputtering conditions, $LiNbO_3$ exhibits a much larger undershoot than indicated by Equation 7.5. This is not predicted from the theory that regards the etching rate of the redeposited material from different substrates to be the same. From this, we conclude that the redeposited material must etch differently from $LiNbO_3$ than from GaAs, fused silica and silicon.

From the discussion in earlier sections on masked deposition, it can be inferred that part of the back-scattering material will be deposited on the vertical wall of the mask. This material, however, will not be etched (assuming

normal incidence of ions). Hence a layer of reflected material will build up on the vertical wall of the mask. Figure 7.14 shows an interference micrograph of the reflected material on the wall of the mask while etching a piece of $LiNbO_3$ at 15 m torr of Argon pressure. The deposited material was removed from a part of the edge to show the reference fringes. The effect of this buildup on the mask wall is to taper the etch profile in the substrate (instead of vertical edges).

It must be pointed out that if a significant gap exists between the mask and the wafer, some of the back scattered material will also get into this region near the mask edge. Figure 7.15 is a Dektak trace of a $LiNbO_3$ wafer after etching. This trace shows a deposition at the edge extending into the masked side of the wafer. The deposition can vary from about 0.1 μm thickness extending to about 5 μm for well placed masks to about 1 μm extending to about 25 μm if the mask and the wafer do not make an intimate contact. Photographs of such a step etched GaAs wafer taken under high magnification and with oblique incidence of light, are shown in Figure 7.16a and 7.16b. When the light is incident such that the step wall does not receive any light, a shadow extends from the step edge into the etched region. However, when the light is incident from the opposite angle a bright reflection from the step wall extends from the step into the etched region. The fringes at the step are due to the

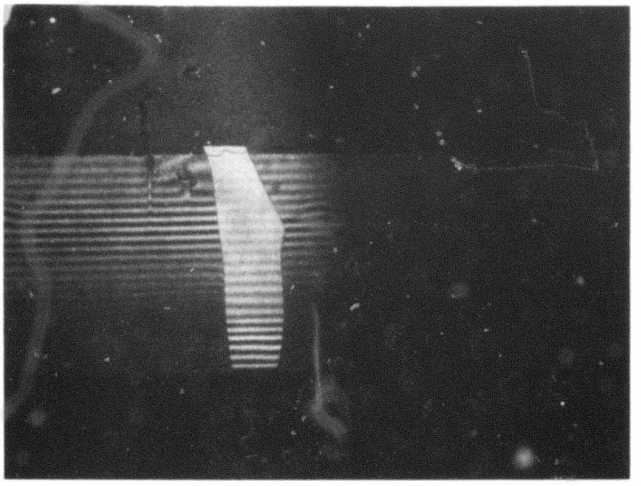

Figure 7.14 Interference micrograph of the film of back-scattered material on the vertical wall of the mask. Part of the film is removed to show the reference fringes.

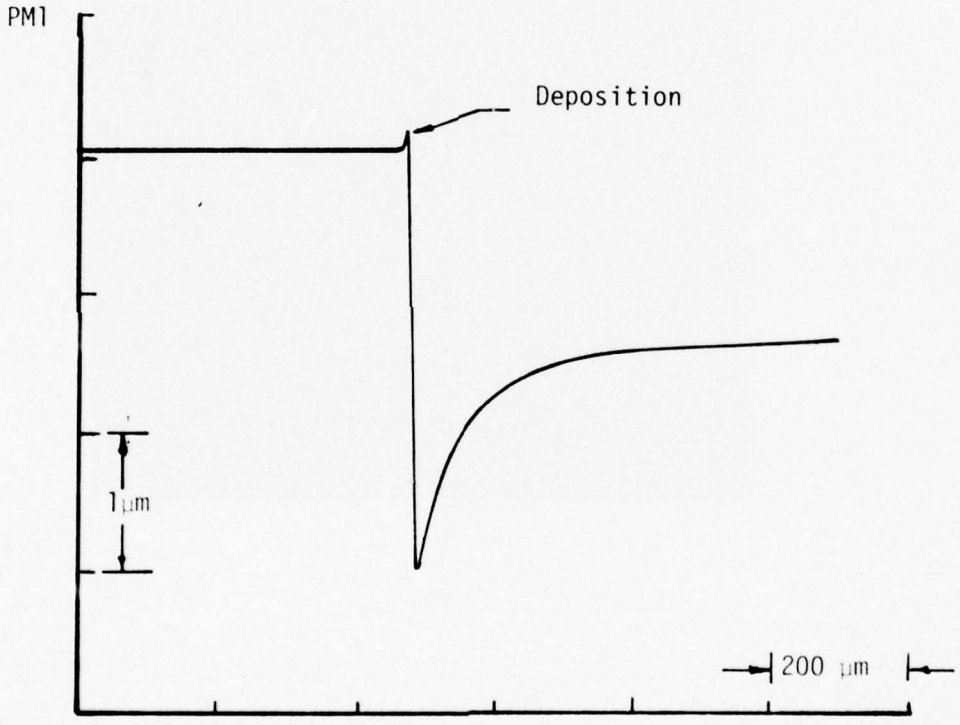

Figure 7.15 Dektak Trace of a Sputter Etched $LiNbO_3$ Wafer Showing Deposition of Resputtered Material Under the Mask.

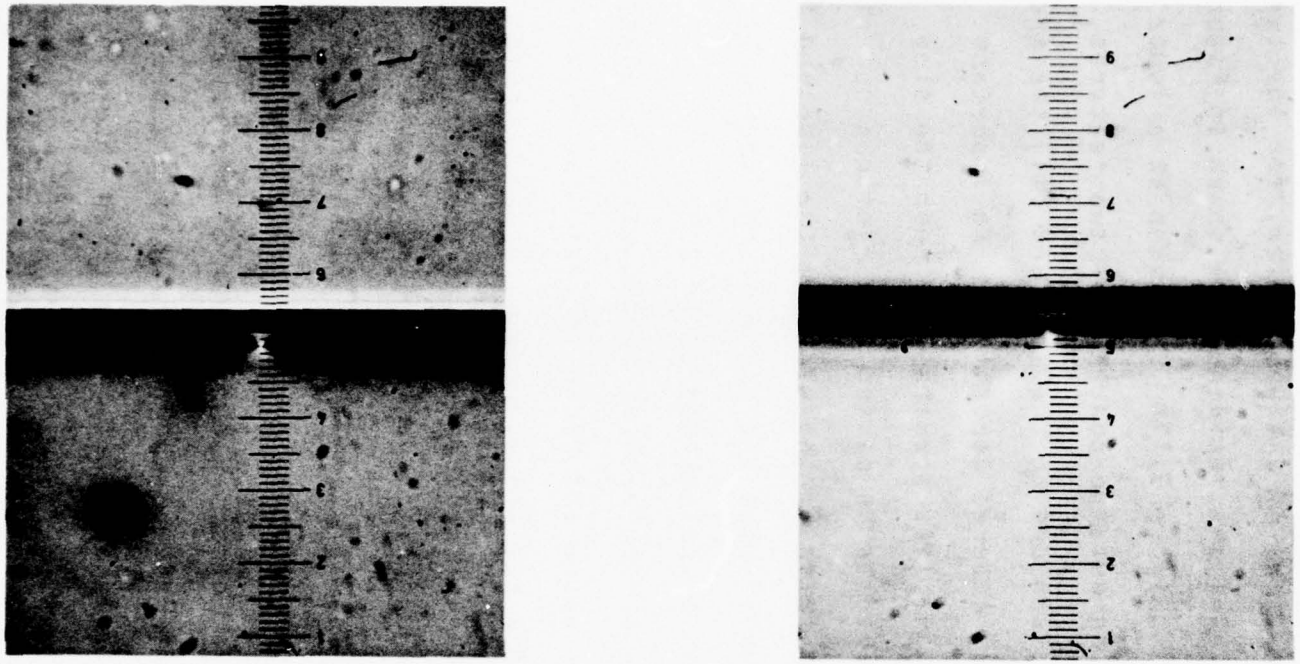

Figure 7.16 Photographs of a GaAs sample after sputter etching under oblique incidence of light. See the text for explanations.

1 small division = 1.45 μ

interference effects of the tapered deposition. When the deposition is chemically etched away, using 5% dil HF, the resulting microscope views of a $LiNbO_3$ wafer, for the two opposite directions of light incidence are shown in Figures 7.17a and 7.17b. Figure 7.17b is taken at a lower magnification to bring out the contrast of two features, (i) interference pattern due to the step and (ii) the area covered by the back scattered deposition.* An important feature of Figure 7.17a is a white line near the step edge. This is believed to be caused by a finite slope of the step wall. From the ratio of the width of the line and the total width of the wall image the angle of the step wall with the vertical can be calculated to be 2.8°.

Back scattering can be reduced in two ways. One way is to reduce the gas pressure and hence increase the mean-free-path of the sputtering gas and ejected material. Table 7.1 summarizes the effects of reducing the gas pressure to 4 m torr in terms of increased etching rates and reduction in undershoot. It is seen that considerably smaller undershoots and high etch rates are possible. This, however, needs increased rf power density and d.c. bias, which may not be desirable in many applications. Moreover, the reduction in gas pressure is limited by the plasma stability for a given interelectrode

*The area of $LiNbO_3$ wafers under the back scattered material is slightly etched in 5% HF probably due to some catalytic effect of the deposition. The depth etched is only a few hundred angstroms and can be easily avoided by shorter etching times.

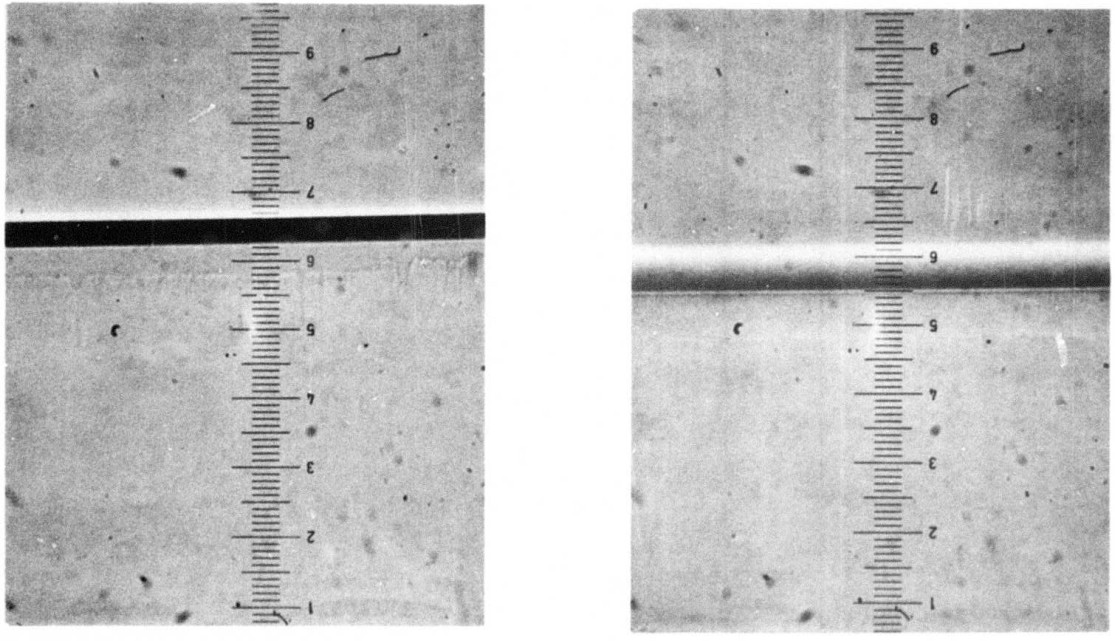

= ~ 0.5μm

(a) (b)

Figure 7.17 Photographs Taken After Chemical Etching in Dil HF

Table 7.1 Effect of Gas Pressure on Etching Parameters

Etching Parameters: Ar Pressure 4 μ
rf power density = 1.184 w/cm^2
D.C. bias = 2.4 kv
(Al electrode)

	GaAs	$LiNbO_3$	Si	Fused Silica
Avg. Etch rate (μ/hr)	4.96	1.6	1.44	1.12
Avg. % under-shoot	<1	<10	10	5

spacing (Paschen's Law). A second way to reduce back scattering is to use slower etching electrode materials. This would include using polished aluminum, SiO_2 or Ti electrodes. We have seen that a coarse electrode surface results in a larger back scattering; this is believed to be caused by a higher sputtering yield of the electrode due to oblique incidence of the ions at the electrode surface. Table 7.2 summarizes the effects of various electrode materials on back scattering. Using a Ti electrode and low rf power, we found the undershoot is almost undetectable.* Figure 7.18 shows the cross section of a GaAs wafer etched 10.8 μm deep using a Ti electrode and 15 m torr of Argon pressure. The angle with the vertical was determined to be less than 2°.

In conclusion, we have shown that the profile of masked deposition is closely predicted by Equation 7.3. The discontinuity in slope can be reduced by using thin masks. Reduction on back scattering will help improve etching in the following ways:

(a) Etching rate of the substrate will increase as predicted by Equation 7.5.

(b) Etching will be more uniform.

(c) Walls of the grooves etched in the substrate will tend to be more vertical.

*Ti targets are very effective for gettering oxygen. This helps to reduce the etch rate of photoresists; it, however, also enhances oxygen depletion of $LiNbO_3$ which results in a slight discoloration of the wafers.

Table 7.2 Effect of Electrode Material on Etching Parameters

Etching Parameters: Ar Pressure: 15 μ
rf power density = 0.4 w/cm^2
D.C. bias = 900 v

		AL	Polished Al	SiO_2	Ti
GaAs	Avg. Etch rate (μ/hr)	1.2	1.55-1.6	1.74	2-2.17
	Avg. % undershoot	20	8	<5	N.D.
$LiNbO_3$	Etch rate	0.243	0.3	0.3 0.5	
	Undershoot	140	100	100 33	

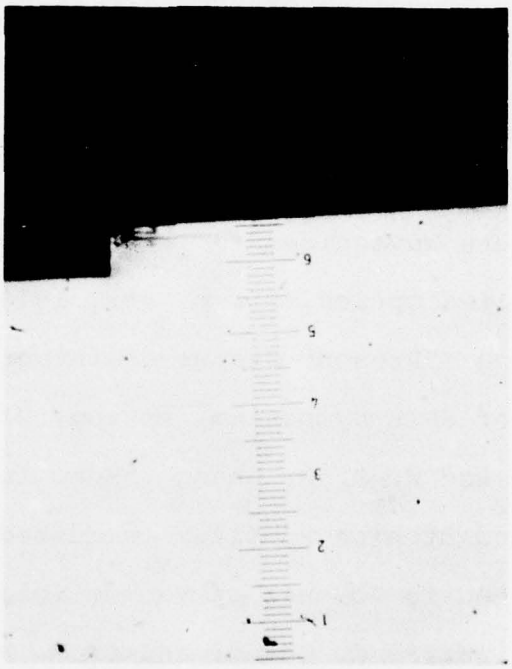

Figure 7.18 Cleaved Section of a GaAs Wafer Etched at 15 μ Argon Pressure with a Ti Electrode

Scale: 1 small division = 1.45 μm

8 PAPERS PUBLISHED

The following is a list of papers published concerning research work supported in part by this contract.

1. W. S. Chang, H. P. Hsu, A. F. Milton, B. L. Sopori, and R. A. Becker "Coupling of Single-Mode Fibers to Thin Film Waveguides", Proceedings of the Electrooptical System Design Conference, Anaheim, Ca., p. 228, 1975.
2. B. L. Sopori and W. S. C. Chang "Evaluation of GaAsP Heterostructure Waveguides for 1.06 μm and 0.905 μm Wavelength", Applied Optics, 15, p. 789, 1976.
3. W. S. C. Chang "Present Status of Integrated Optical Devices", Proceedings of SPIE Symposium, Reston, Virginia 1976.
4. B. L. Sopori and W. S. C. Chang "Some Investigations on Deposition and Etching Profiles in Masked r.f. Sputtering", To be published in Journal of Vacuum Science and Technology.
5. B. L. Sopori, W. S. C. Chang, and C. M. Phillips "A New Method for the Efficient Interconnection of High Index Planar Waveguide to Low Index Transitional Waveguides", Appl. Phys Lett., Vol. 29, p. 800, 1976.
6. B. L. Sopori "A Transitional Waveguide For Coupling a High Index Thin-Film Waveguide to a Single Mode Fiber", D.Sc. Dissertation, Washington University, 1977.

9 CONCLUSION

A careful examination of the various coupling methods that may be used to interconnect a single mode fiber with a GaAsP waveguide has been made. The most attractive method is to sputter etch a section of the primary waveguide and then to fabricate a glass/SiO_2 transition waveguide to replace the etched section of the primary waveguide. The fabricated transition waveguide will be coupled to the primary waveguide by direct end excitation. The other end of the transition waveguide will be coupled to the fiber via the tapered velocity coupling method. Transition from the planar geometry of the primary waveguide to the cylindrical geometry of the fiber will be accomplished by fabricating a transition waveguide that has a tapered width, transforming a planar waveguide into a channel waveguide.

Experimental and theoretical investigation on the fabrication and evaluation of the transition waveguide was undertaken to obtain the following results: (a) Techniques for deep and high surface quality step-etch have been developed using the r.f. sputtering process with a cleaved GaAs as a mask. Etching depth of several micrometers and an etched profile only a few degrees off from the desired vertical direction can be realized at 4 μm of Argon pressure, 50 watts of r.f. power, and several hours of etching time. Except

for a slight undershoot (about 8%) near the step edge, the sputter etching process has satisfied all the requirements. (b) Deposition of a SiO_2 layer followed by the deposition of BaO_2 glass or AZ1350 as the waveguiding layer has given us a high efficiency coupling between the GaAsP primary waveguide and the transition waveguide. Coupling efficiency up to 80% has been observed. Further improvement of this efficiency may be possible provided additional research will be conducted to develop techniques for filling up the small gap created by the undershoot. (c) We demonstrated that transition from the planar geometry of the uniform thin film waveguide to the cylindrical geometry of the fiber cannot be accomplished by fabricating a fiber horn. Instead we have demonstrated that a tapered transition from the planar waveguide to the channel waveguide can be realized, compatible with the materials used in our transition waveguide. We have developed successfully the technology for fabricating sodium glass waveguides on SiO_2. Such sodium glass waveguides have showed extremely low losses (less than 1 dB/cm for planar waveguide and less than 2 dB/cm for channel waveguide). Ion exchange, laser heating, and masked sputter deposition has been shown to be useful to obtain low loss transition waveguide tapers.*

Due to the limitation in time and in funding, the total coupling from the single mode fiber to the GaAs waveguide has not yet been demonstrated. The major unfinished task is the coupling

*Work supported in Navy Contract N-00014-76-C-0796.

of a single mode fiber to a transition waveguide. However tapered velocity coupling between two low index waveguides has been demonstrated to have 85% coupling efficiency at Washington University. The development of the sodium glass thin film waveguide technology indicates that it can be used to raise the β value of the fiber and to provide the necessary evanescent field for the tapered velocity coupling. In short, based upon the research results that have been obtained today, we are confident that an efficiency of 50% or larger can be realized in this method for the coupling of a single mode fiber to a GaAs waveguide. However, additional research is needed in order to demonstrate the total coupling system.

10. BIBLIOGRAPHY

1. Miller, Steward E., Marcatili, Enrique A.J., and Li Tingye, Part I; Miller, Steward E., Li Tingye and Marcatili, Enrique A.J., Part II, "Research Toward Optical-Fiber Transmission Systems", Proceedings of IEEE, Vol. 61 (1703), Dec. 1973.

2. Andrews, R.A., Milton, Fenner A., and Giallorenzi, Thomas G., "Military Applications of Fiber Optics and Integrated Optics," IEEE Trans., Microwave Theory Tech., Vol. MTT-21 (763), Dec. 1973.

3. Polky, J.N. and Harris, J.H., "Integrated Electro-Optic Thin Film Modulator," Appl. Phys. Lett., Vol. 61, (154), 1971.

4. Tsai, C.S. and Saunier, P., "Ultrafast Guided-Light Beam Deflection/Switching and Modulation Using Simulated Electro-Optics Prism Structures in $LiNbO_3$ Waveguide," Appl. Phys. Lett., Vol. 27, (248), 1975.

5. Flanders, D.C., Kogelnik, H., Schmidt, R.V. and Shank, C.V., "Grating Filters for Integrated Optical Waveguides," Appl. Phys. Lett., Vol. 25, (116), 1974.

6. Nakamura, M., and A. Yariv, "Distributed Feedback Semiconductor Lasers," Paper MAI, Topical Meeting on Integrated Optics, Salt Lake City, Jan. 1976.

7. Payne, D.N., and Gambling, W.A., "New Silica-Based Low-Loss Optical Fibre', Electron. Lett., Vol. 10, (289), July 1974.

8. Tasker, William G., and French, William G., "Low-Loss Optical Waveguides with Pure Fused SiO_2 Cores", Proc. IEEE, Vol. 62, (1281), Sept. 1974.

9. Gloge, D., Smith, P.W., Bisbee, D.L. and Chinnock, E.L., Optical Fiber End Preparation for Low-Loss Splices", Bell System Tech. J., Vol. 52, (1579), Nov. 1973.

10. Soneda, C.G., "Simple, Low-Loss Joints Between Single-Mode Optical Fibers", Bell Sys. Tech. J., Vol. 52, (583), April, 1973.

11. Cohen, L.G., "Power Coupling from GaAs Injection Lasers into Optical Fibers", Bell Sys. Tech. J., Vol. 51. (573), March 1972.

12. Dietrich, Marcuse, "Excitation of the Dominant Mode of a Round Fiber by a Gaussian Beam", Bell Sys. Tech. J., Vol. 52, (1695), October 1970.

13. Cook, J.S., Mammel, W.L. and Grow, R.J.,"Effect of Misalignments on coupling Efficiency of Single-Mode Optical Fiber Butt Joints", Bell Sys. Tech. J., Vol. 52, (1439), October 1973.

14. Biovin, L.P., "Thin-Film Laser-to-Fiber Coupler", Appl. Optics, Vol. 13, (391), February 1974.

15. Giutmann, J., Krumpholz, O., and Pfeiffer, E., "Optical Fiber-to-Stripline-Coupler", Applied Opticsl, Vol. 14, (1225), May 1975.

16. Hsu, H.P. and Milton, A.F., "Single Mode Coupling Between Fibers and Channel Waveguides", to be published.

17. Cohen, L.G., and Schneider, "Microlenses for Coupling Junction Lasers to Optical Fibers", Applied Optics, Vol. 13 (89), January 1974.

18. Auracher, F., "A Photoresist Coupler for Optical Waveguides," Optics Comm., Vol. 11, (191), June 1974.

19. Kato Daisuke, "Light Coupling from a Stripe-Geometry GaAs diode Laser into an Optical Fiber with Spherical End," J. Appl. Phys., Vol. 44, (2756), June 1973.

20. Pierce, J.R., "Coupling of Modes of Propagation", J. Appl. Phys., Vol. 25, (179), February 1954.

21. Yariv, Amnon, "Coupled-Mode Theory for Guided-Wave Optics," IEEE QU, Vol. 9, (191), September 1973.

22. Somekh, S., Garmire, E., Yariv, A., Garvin, H.L., and Hunsperger, R.G., "Channel Optical Waveguides and Directional Couplers in GaAs - Imbedded and Ridged", Appl. Optics, Vol. 13, (327), February 1974.

23. Papnchon, M., Combemale, Y., Mathieu, X., Ostrowsky, D.B., Reiber, L., Roy, A.M., Sejourne, B., and Werner, M., "Electrically Switched Optical Directional Coupler: Cobra," Appl. Phys. Lett., Vol. 27, (289), 1975.

24. Hsu, H.P. and Chang, W.S.C, "A Progress Report on Coupling Methods in Prospective Single Mode Fiber-Integrated Optics Systems", to be published.

25. Bulmer, C.H. and Wilson, M.G.F., "Distributed Coupling Between a Singlemode Fibre and a Planar Waveguide", Paper WB3 presented at Topical Meeting on Integrated Optics, Salt Lake City, January 1976.

26. Hammer, J.M., Bartolini, R.A., Miller, A., and Neil, C.C., "Grating Coupling Between Low Index Fiber and High Index Film Waveguide", Paper WD3, Topical Meeting on Integrated Optics, alt Lake City, January, 1976.

27. Wilson, M.G.F., and Teh, G.A., "Tapered Optical Directional Coupler", IEEE Trans. on Microwave Theory and Technique, Vol. MTT-23, (85), January 1975.

28. Louisell, W.H., "Analysis of the Single Tapered Mode Coupler," Bell Sys. Tech. J., (853), July 1955.

29. Fox, A.G., "Wave Coupling by Warped Normal Modes", Bell Sys. Tech. J., (823), July 1955.

30. Burns, W.K. and Milton, A.F., "Mode Conversion in Planar Dielectric Separating Waveguides", IEEE J. Quantum Electron., Vol. QE-11, (32), 1975.

31. Milton, A.F. and Burns, W.K., "The Design of Tapered Velocity Couplers for Integrated Optics", Appl. Optics, Vol. 14, (1207), April 1975.

32. Yajima, Hiroyoshi, "Dielectric Thin-Film Optical Branching Waveguide", Appl. Phys. Lett. Vol. 22, (647), June 1973.

33. Becker, R., "The Tapered Velocity Coupler-Optical Connector", M.S. Thesis, Washington University, St. Louis, Missouri, 1977.

34. Smith, R.B., "Analytical Solutions for Linearly Tapered Directional Couplers", J. Opt. Soc. Am., Vol. 66, (882), September 1976.

35. Dalgoutte, D.G., Smith, R.B., Achutaramayya, G., and Harris, J.H., "Externally Mounted Fibers for Integrated Optics Interconnections", Appl. Optics, Vol. 14, (1860), August 1975.

36. Yamamoto, Y., Naruse, Y., Kamiya, T., and Yanai, H., "A Large-Tolerant Single-Mode Optical Fiber Coupler with a Tapered Structure," Proc. IEEE, (1014), June 1976.

37. Tien, P.K., "Light Wave in Thin Films and Integrated Optics", Appl. Optics, Vol. 10, (2395), 1971.

38. Dietrich, M., "Radiation Losses of Tapered Dielectric Slab Waveguides", Bell Sys. Tech. J., Vol. , (273), February 1970.

39. Chang, W.S.C., Muller, M.W., and Rosenbaum, F.J., "Integrated Optics" in Laser Applications, Vol. 2, edited by Monte Ross, Academic Press, 1974.

40. Henderson, D.M., "Waveguide Lasers with Intercavity Electroptic Modulators: Misalignment Loss", Appl. Optics, Vol. 15, (1066), April 1976.

41. Chang, W.S.C., "Leakage of Guided Wave Modes to Adjacent High Index Medium", unpublished results.

42. Born, Max, and Wolf, Emil, "Principles of Optics", Chapter I, Pergamon Press, 1970.

43. Reisinger, A., "Characteristics of Optical Guided Modes in Lossy Waveguides", Appl. Optics, Vol. 12, (1015), May 1973.

44. Ferrocynide etch: 8gms $K_3Fe(CN)_6$, 12 gms KOH in 100 ml of DI water.

45. Sopori, B.L. and Chang, W.S.C, "Propagation Characteristics of GaAsP Heterostructure Waveguides at 1.06μm Wavelengths," Appl. Optics, Vol. 15, (789), 1975.

46. Stoller, A.I., "The Etching of Deep Vertical-Walled Patterns in Silicon", RCA Review, (271), June 1970.

47. Rowland, M.C., "GaAs Lasers", edited by Gooch, C.H.

48. Gannon, J.J. and Nuese, C.J., "A Chemical Etchant for the Selective Removal of GaAs Through SiO_2 Masks", J. Electrochem. Soc., Vol. 121, (1215), September 1974.

49. Jacobson, R.L. and Wahner, G.K., "Study of Ion-Bombardment Damage on a Ge (111) Surface by Low-Energy Electron Diffraction", J. Appl. Phys., Vol. 36, (2674), September 1965.

50. Chen, B., Tangonan G. L., and Lee, A., "Horn Structures for Integrated Optics" Optics Communications, Vol. 20, (250), 1977

51. Swarts, E. L., "Introduction to Glass Science", edited by Pye, L.D., Stevens, H.J. and LaCourse, W. C., Plenum Press, 1972.

52. Marcatili, E. A. J. and Schmeltzer, "Hollow Dielectric Waveguide Modes", Bell Sys. Tech. J., Vol. 43, (1783), 1964.

53. Smith, P. W., "A Waveguide Gas Laser", Appl. Phys., Lett., Vol. 19, (132), 1971.

54. Maissel, L. I. And Reinhard, G., "Handbook of Thin Film Technology", McGraw-Hill Book Company, 1970.

55. Standley, C. L., Jones, R. E. and Maissel, L. I., "Sputtered SiO_2 Deposited Over a Step", Thin Solid Films, Vol. 5, (355), 1970.

56. Jones, R. E., Standley, C. L. and Maissel, L. I., "Re-emission Coefficient of Si and SiO_2 Films Deposited Through rf and dc Sputtering", J. Appl. Phys., Vol. 38, (4656), 1967.

57. Dimigen, H., Luthje, H., Hubsch, H., and Convertini, U., "Influence of Mask Materials on Ion-Etched Structures", J. Vac. Sci. Technol., Vol. 13 (976), July/August 1976.

METRIC SYSTEM

BASE UNITS:

Quantity	Unit	SI Symbol	Formula
length	metre	m	...
mass	kilogram	kg	...
time	second	s	...
electric current	ampere	A	...
thermodynamic temperature	kelvin	K	...
amount of substance	mole	mol	...
luminous intensity	candela	cd	...

SUPPLEMENTARY UNITS:

plane angle	radian	rad	...
solid angle	steradian	sr	...

DERIVED UNITS:

Acceleration	metre per second squared	...	m/s
activity (of a radioactive source)	disintegration per second	...	(disintegration)/s
angular acceleration	radian per second squared	...	rad/s
angular velocity	radian per second	...	rad/s
area	square metre	...	m
density	kilogram per cubic metre	...	kg/m
electric capacitance	farad	F	A·s/V
electrical conductance	siemens	S	A/V
electric field strength	volt per metre	...	V/m
electric inductance	henry	H	V·s/A
electric potential difference	volt	V	W/A
electric resistance	ohm		V/A
electromotive force	volt	V	W/A
energy	joule	J	N·m
entropy	joule per kelvin	...	J/K
force	newton	N	kg·m/s
frequency	hertz	Hz	(cycle)/s
illuminance	*lux*	lx	lm/m
luminance	candela per square metre	...	cd/m
luminous flux	lumen	lm	cd·sr
magnetic field strength	ampere per metre	...	A/m
magnetic flux	weber	Wb	V·s
magnetic flux density	tesla	T	Wb/m
magnetomotive force	ampere	A	...
power	watt	W	J/s
pressure	pascal	Pa	N/m
quantity of electricity	coulomb	C	A·s
quantity of heat	joule	J	N·m
radiant intensity	watt per steradian	...	W/sr
specific heat	joule per kilogram-kelvin	...	J/kg·K
stress	pascal	Pa	N/m
thermal conductivity	watt per metre-kelvin	...	W/m·K
velocity	metre per second	...	m/s
viscosity, dynamic	pascal-second	...	Pa·s
viscosity, kinematic	square metre per second	...	m/s
voltage	volt	V	W/A
volume	cubic metre	...	m
wavenumber	reciprocal metre	...	(wave)/m
work	joule	J	N·m

SI PREFIXES:

Multiplication Factors	Prefix	SI Symbol
1 000 000 000 000 = 10^{12}	tera	T
1 000 000 000 = 10^{9}	giga	G
1 000 000 = 10^{6}	mega	M
1 000 = 10^{3}	kilo	k
100 = 10^{2}	hecto*	h
10 = 10^{1}	deka*	da
0.1 = 10^{-1}	deci*	d
0.01 = 10^{-2}	centi*	c
0.001 = 10^{-3}	milli	m
0.000 001 = 10^{-6}	micro	μ
0.000 000 001 = 10^{-9}	nano	n
0.000 000 000 001 = 10^{-12}	pico	p
0.000 000 000 000 001 = 10^{-15}	femto	f
0.000 000 000 000 000 001 = 10^{-18}	atto	a

* *To be avoided where possible.*